Fluid–Structure Interaction Models of Bioprosthetic Heart Valve Dynamics in an Experimental Pulse Duplicator

Jae H. Lee[1], Alex D. Rygg[2], Ebrahim M. Kolahdouz[1,2], Simone Rossi[1], Stephen M. Retta[2], Nandini Duraiswamy[2], Larry N. Scotten[3], Brent A. Craven[2], and Boyce E. Griffith[4,5,6,7]

[1]Department of Mathematics, University of North Carolina, Chapel Hill, NC, USA
[2]Division of Applied Mechanics, Office of Science and Engineering Laboratories, Center for Devices and Radiological Health, United States Food and Drug Administration, Silver Spring, MD, USA
[3]LNS Consulting, Victoria, BC, Canada
[4]Departments of Mathematics, Applied Physical Sciences, and Biomedical Engineering, University of North Carolina, Chapel Hill, NC, USA
[5]Carolina Center for Interdisciplinary Applied Mathematics, University of North Carolina, Chapel Hill, NC, USA
[6]Computational Medicine Program, University of North Carolina, Chapel Hill, NC, USA
[7]McAllister Heart Institute, University of North Carolina, Chapel Hill, NC, USA
boyceg@email.unc.edu

Abstract

Computer modeling and simulation (CM&S) is a powerful tool for assessing the performance of medical devices such as bioprosthetic heart valves (BHVs) that promises to accelerate device design and regulation. This study describes work to develop dynamic computer models of BHVs in the aortic test section of an experimental pulse-duplicator platform that is used in academia, industry, and regulatory agencies to assess BHV performance. These computational models are based on a hyperelastic finite element extension of the immersed boundary method for fluid–structure interaction (FSI). We focus on porcine tissue and bovine pericardial BHVs, which are commonly used in surgical valve replacement. We compare our numerical simulations to experimental data from two similar pulse duplicators, including a commercial ViVitro system and a custom platform related to the ViVitro pulse duplicator. Excellent agreement is demonstrated between the computational and experimental results for bulk flow rates, pressures, valve open areas, and the timing of valve opening and closure in conditions commonly used to assess BHV performance. In addition, reasonable agreement is demonstrated for quantitative measures of leaflet kinematics under these same conditions. This work represents a step towards the experimental validation of this FSI modeling platform for evaluating BHVs.

Keywords: immersed boundary method, finite element method, porcine aortic valve, bovine pericardial valve

1 Introduction

Worldwide, nearly 300,000 aortic valve replacements are performed annually, and the rate of heart valve replacement is projected to exceed 850,000/year by 2050 [1]. Bioprosthetic heart valves (BHVs) are commonly constructed from fixed porcine heart valves or bovine or porcine pericardial tissues. BHVs generate flow patterns that mimic those of the normal human aortic valve and typically allow patients to be managed without chronic anticoagulation [2]. Unfortunately, BHVs have a limited durability, and they typically fail 10–15 years post implantation, primarily from tissue degeneration or calcification [3].

Computer modeling and simulation (CM&S) can be used throughout the life cycle of prosthetic valve design and regulatory approval. CM&S is a cost- and time-efficient complement to traditional bench testing that can assess device performance under a broader range of conditions than those listed in the instructions for use, including patient-specific conditions [4]. Simulations may be used in the design phase to optimize device design. Credible simulation data may also be leveraged in regulatory applications to support claims of device safety and effectiveness. Indeed, using modeling and simulation to support regulatory decision-making is a strategic priority area for the U.S. FDA Center for Devices and Radiological Health [5]. CM&S is well-suited for performing root cause analyses to understand impaired device function. For example, CM&S provides information about valve performance that is difficult to acquire on the bench, including assessing the impact of non-circular configurations on transcatheter BHVs [6]. To realize its full impact in device regulation, however, CM&S results must be shown to be credible through verification and validation (V&V) [7].

A fluid–structure interaction (FSI) approach is necessary to model heart valves across the full cardiac cycle [8]. Accounting for coupling between the flexible valve leaflets and the fluid flow is crucial in studying the effect of vortices in the aortic sinuses, predicting fluid-induced shear stress on the leaflets, and assessing valve performance by quantifying the valve orifice area and regurgitation [9]. A widely used approach to simulating cardiovascular FSI is the arbitrary Lagrangian–Eulerian (ALE) method [10,11], which uses body-conforming meshes for the fluid and solid. ALE methods have realized limited success in simulating the dynamics of heart valves to date, however, because of the substantial challenges posed by dynamically generating geometrically conforming discretizations of thin structures that undergo substantial motion [10,11].

Non-body conforming discretizations, which avoid the difficulties of body-fitted grids, are now widely used to model heart valve dynamics. One of the earliest of these types of approaches is the immersed boundary (IB) method [12], which was introduced by Peskin to simulate heart valves [13,14]. The IB formulation allows the structural discretization to be independent of the fluid grid and thereby facilitates models with very large structural deformations [15]. Extensions to the IB method have also been used to simulate heart valves [16,17], but in most cases, these prior simulations were not fully resolved, and the valve leaflets were described using only simple structural models based on linear elasticity. Other studies [18,19] used anisotropic models of native and bioprosthetic valves but do not address the diastolic phase of the cardiac cycle. Flamini et al. [20] used an IB approach to simulate aortic valve FSI across multiple cardiac cycles, but they used a simplified description of the aortic valve mechanics. Hasan et al. [21] also used an IB approach to simulate FSI in a subject-specific aortic root model, and they used realistic hyperelastic constitutive models to describe the valve leaflets, but their model has not been validated. In addition, neither study used subject-specific driving or loading conditions.

Methods also have been developed that combine features of ALE and IB-like approaches, including the hybrid fictitious domain/ALE method [22] and the immersogeometric (IMGA) method [9,23–26]. These methods also seek to relax the need to use body-conforming discretizations. Prior models of aortic valves using a fictitious domain/ALE method [22] showed instabilities when simulated under physiological Reynolds numbers and transvalvular pressures. The IMGA method has been used in several studies on pericardial BHVs that include experimentally derived constitutive models of the valve leaflets. Hsu et al. [23] validated the leaflet kinematics of their model by comparing the cross-sectional profiles of the leaflets to those from dynamic in vitro experimental measurements [27]. Xu et al. [25] used in vivo imaging data to drive their simulations and compared the fluid flow patterns with those from magnetic resonance imaging. These models both employed isotropic descriptions of the pericardial BHV leaflets. Wu et al. [26] used an anisotropic model that incorporated the fiber structure of a bovine pericardial valve that was developed and validated with experimental data from Sun and Sacks [28]. These prior studies did not use boundary condition models that established flow conditions directly comparable to available experimental or clinical data.

Other methods that avoid body-conforming discretizations include smoothed particle hydrodynamics (SPH) [29]. The SPH approach [29], however, cannot fully impose incompressibility, and prescribing boundary conditions is difficult. In addition, several studies have used cut-cell-like methods [30–32] to simulate valve FSI, but these studies also used linearly elastic leaflet models and have not yet been validated.

To date, there have been relatively few experimental validation studies of FSI models of native or bioprosthetic aortic valves [33, 34]. The two studies by Tang et al. [33] and Sigüenza et al. [34] use idealized isotropic leaflet models that do not account for leaflet anisotropy and, as a result, their simulations show discrepancies in the dynamics of the valve compared with experimental data. These studies also do not use flow domains that are long enough to allow the complex flow patterns downstream of the valve to develop fully. The model of Sigüenza et al. exhibits incomplete closure and experiences substantial regurgitation during diastole, leading to an underestimation of the transvalvular pressure gradient. The study of Sigüenza et al. also uses flow rate boundary conditions throughout the cycle, which introduces bias in the valve dynamics.

This study develops a computational FSI model based on the IB method of an experimental pulse-duplicator platform for simulating BHV dynamics. The model is calibrated using relatively limited experimental data, and this study describes initial work towards the V&V of this model for porcine tissue and bovine pericardial BHVs. Our models of the leaflet mechanics are based on experimental tensile test data [35–37] of fixed tissues that are similar to the biomaterials used to construct porcine aortic and bovine pericardial BHVs. To provide realistic driving and loading conditions across the full cardiac cycle, we use reduced-order models that are calibrated using pressure and flow data acquired from the pulse-duplicator systems. Simulation results are compared to experimental data obtained from a commercial ViVitro pulse duplicator and a customized experimental apparatus based on the ViVitro pulse duplicator.

2 Materials and Methods

2.1 Experimental Pulse Duplicator

In vitro experiments are performed using two different experimental platforms, including a ViVitro Pulse Duplicator (ViVitro Labs, Inc., Victoria, BC, Canada) available through the FDA Cardiac Device Flow Lab and a customized pulse duplicator developed by Scotten that is similar to the commercial ViVitro system. Figure 1a details Scotten's customized system. It includes a prototype *Leonardo* electro-optical subsystem [38] to assess projected dynamic valve area (PDVA). The commercial ViVitro system is similar but uses high-speed videography to assess valve kinematics, from which we reconstruct PDVA data via automatic image analysis in DataTank (Visual Data Tools, Inc., Chapel Hill, NC, USA). We also measure flow rates and pressures, as indicated in Figure 1b. Experiments in the customized pulse duplicator use a 25 mm Labcor TLBP A Supra (Labcor Laboratórios Ltd., Belo Horizonte, Brazil) porcine aortic valve. Flow and pressure signals are filtered at 100 Hz, and PDVA signals are not filtered. Experiments at the FDA use a Model 2800 25 mm Carpentier–Edwards PERIMOUNT RSR (Edwards Lifesciences, Irvine, CA, USA) bovine pericardial aortic valve. Flow signals are filtered at 100 Hz, and pressure signals are not filtered. Both experiments use saline as the test fluid for this initial study because the viscosities of common blood analogues are more sensitive to temperature than saline. In addition, saline is widely used for hydrodynamic assessments of heart valves [39]. For instance, the ISO 5840-3 standard allows saline to be used as a test fluid [40], and the most recent inter-laboratory study by Wu et al. [41] also used saline as the test fluid. Results presented in Supplemental Materials Section G examine the effect of using a Newtonian blood analogue instead of saline in the computational model.

(a)

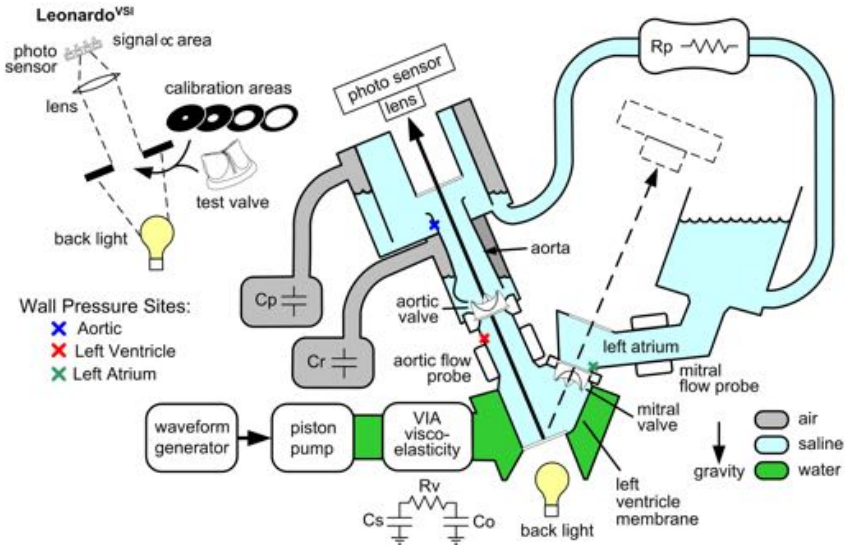

(b)

Figure 1: (a) A customized pulse duplicator based on the commercial ViVitro pulse-duplicator system adapted with prototype electro-optical subsystem for measuring aortic valve projected dynamic valve area (PDVA), or alternate configuration for measuring mitral valve PDVA. (b) A schematic diagram of the custom pulse duplicator based on the commercial ViVitro pulse-duplicator system adapted with prototype electro-optical subsystem for measuring aortic valve PDVA, or alternate configuration for measuring mitral valve PDVA. The commercial ViVitro system is similar but lacks the back light and the photo sensor for acquiring PDVA.

2.2 Solid Mechanics Models

2.2.1 Leaflet Mechanics

We describe the biomechanics of the valve leaflets using the framework of nonlinear solid mechanics [42]. Briefly, leaflet deformations are described by the mapping $\boldsymbol{\chi} = \boldsymbol{\chi}(\boldsymbol{X}, t)$ between reference coordinates $\boldsymbol{X}$ and

current coordinates $\boldsymbol{x}$ at time t. The valve leaflets are treated as anisotropic, incompressible, hyperelastic materials. For a hyperelastic material, the first Piola–Kirchhoff stress $\mathbb{P}$ is related to a strain-energy functional $\Psi(\mathbb{F})$ via [21]

$$\mathbb{P} = \frac{\partial \Psi}{\partial \mathbb{F}}, \tag{1}$$

in which $\mathbb{F} = \partial \boldsymbol{\chi}/\partial \boldsymbol{X}$ is the deformation gradient tensor. We split the strain energy functional into isochoric and volumetric parts,

$$\Psi(\mathbb{F}) = W(\overline{\mathbb{F}}) + U(J), \tag{2}$$

in which $\overline{\mathbb{F}} = J^{-1/3}\mathbb{F}$ and $J = \det \mathbb{F}$. We use a modified version of the Holzapfel–Gasser–Ogden model from Murdock et al. [43] with the addition of angle dispersion [44]. The isochoric part of the model, $W(\overline{\mathbb{F}})$, includes an isotropic contribution from the extracellular matrix and an anisotropic contribution from the collagen fibers embedded in the leaflets,

$$W(\overline{\mathbb{F}}) = W_{\text{iso}}(\overline{\mathbb{F}}) + W_{\text{aniso}}(\overline{\mathbb{F}}). \tag{3}$$

This model describes the extracellular matrix as an exponential neo-Hookean material along with a collagen fiber reinforcement model accounting for angle dispersion,

$$W_{\text{iso}}(\overline{\mathbb{F}}) = C_{10}\{\exp\left[C_{01}(\bar{I}_1 - 3)\right] - 1\}, \tag{4}$$

$$W_{\text{aniso}}(\overline{\mathbb{F}}) = \frac{k_1}{2k_2}\{\exp\left[k_2(\kappa \bar{I}_1 + (1-3\kappa)\bar{I}_4^{\star} - 1)^2\right] - 1\}, \tag{5}$$

in which $\bar{I}_1 = \text{tr}(\overline{\mathbb{C}})$ is the first invariant of the modified right Cauchy–Green strain tensor $\overline{\mathbb{C}} = \overline{\mathbb{F}}^T\overline{\mathbb{F}}$, $\bar{I}_4^{\star} = \max(\bar{I}_4, 1) = \max(\boldsymbol{e}_0^T\overline{\mathbb{C}}\boldsymbol{e}_0, 1)$, and $\boldsymbol{e}_0$ is a unit vector aligned with the mean fiber direction in the reference configuration. By construction, $\bar{I}_4^{\star}$ is nonzero in extension but not in compression. The parameter $\kappa \in [0, \frac{1}{3}]$ describes collagen fiber angle dispersion. If $\kappa = 0$, the fibers are perfectly aligned and the constitutive model becomes the same as that of Murdock et al. [43] By contrast, if $\kappa = \frac{1}{3}$, then the model describes an isotropic distribution of fibers, and we obtain an isotropic model with no preferred direction of fiber reinforcement. The parameters for the porcine aortic valve are fit to experimental tensile test data from Billiar and Sacks [35,36] for glutaraldehyde-fixed porcine aortic valves (Fig. 2a). We obtain $C_{10} = 0.302$ kPa, $C_{01} = 3.25$, $k_1 = 0.197$ MPa, $k_2 = 0.001$, and $\kappa = 0.0$. The parameters for the bovine pericardial valve are fit to biaxial data from Kim et al. [37], and we obtain $C_{10} = 0.119$ kPa, $C_{01} = 22.59$, $k_1 = 2.38$ MPa, $k_2 = 149.8$, and $\kappa = 0.292$. For further details, see Supplemental Materials Section B. The mathematical framework used in this study treats the leaflets as exactly incompressible. Thus, within our numerical framework, the volumetric part of the strain energy,

$$U(J) = \beta(J \ln J - J + 1), \tag{6}$$

can be viewed as a stabilization term. For further details, see the summary of the study of Vadala-Roth et al. [45] in Supplemental Materials Section E. We use $\beta = 14.1$ MPa in our simulations.

The geometry of the Labcor TLBP A Supra porcine aortic valve is constructed based on literature values [46]. A model collagen fiber architecture is created using Poisson interpolation [47] (Fig. 2a). The pericardial valve geometry is reconstructed from micro-CT images of a Carpentier–Edwards PERIMOUNT RSR Model 2800 surgical aortic heart valve (Fig. 2b). The mean fiber orientation is chosen to be 45° (Fig. 2b), following the small angle light scattering data of Sun et al. [28]

2.2.2 Aortic Test Section

The wall of the aortic test section is glass. To avoid the expensive linear solvers required by exactly imposing the rigidity constraint within the present computational framework [48], we instead use a penalty method that models the test section as a stiff neo-Hookean material with [21]

$$W_{\text{wall}} = \frac{c_{\text{wall}}}{2}(\bar{I}_1 - 3). \tag{7}$$

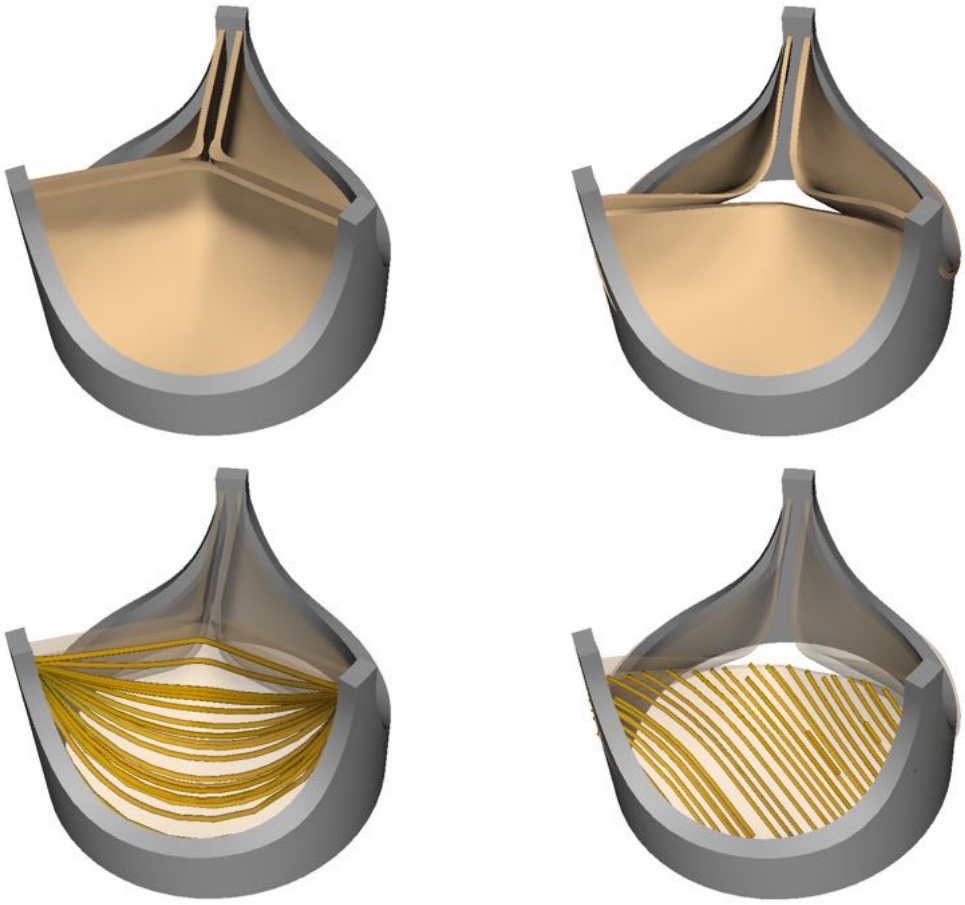

(a) **(b)**

Figure 2: (a) Model porcine bioprosthetic valve geometry and fiber architecture. The idealized geometry of the Labcor TLBP A Supra porcine aortic valve is reconstructed based on literature values [46]. The model fiber structure is generated using Poisson interpolation [47]. (b) Model bovine pericardial bioprosthetic valve geometry and fiber architecture. This valve geometry is obtained from micro-CT imaging of a Carpentier-Edwards PERIMOUNT RSR Model 2800 surgical aortic heart valve. The model fiber structure is generated based on the small angle light scattering (SALS) data of Sun et al. [28]. The SALS data show that the mean fiber orientation of a bovine pericardial valve leaflet is 45°.

Additional structural forces are included in the rigid test section model,

$$\boldsymbol{F}(\boldsymbol{X},t) = \kappa_{\text{wall}}(\boldsymbol{X} - \boldsymbol{\chi}(\boldsymbol{X},t)). \tag{8}$$

In the limit as c_{wall} and κ_{wall} become large, the test section becomes effectively rigid and stationary. We use $c_{\text{wall}} = 33.1$ kPa and $\kappa_{\text{wall}} = 8.52 \times 10^5$ kPa cm^{-2}.

2.3 Fluid Model and Boundary Conditions

We use the incompressible Navier–Stokes equations to model the test fluid in the aortic test section of the pulse duplicator as a viscous incompressible fluid. We model the saline solution with a uniform density $\rho = 1.0$ g cm^{-3} and a uniform dynamic viscosity $\mu = 1.0$ cP (saline at 25 °C) for both cases. Results from additional simulations using a blood analogue fluid with density 1.0 g cm^{-3} and viscosity 3.5 cP are provided in Supplemental Materials Section G. These simulations indicate that the large-scale flow structures and leaflet kinematics are similar between saline and the blood analogue.

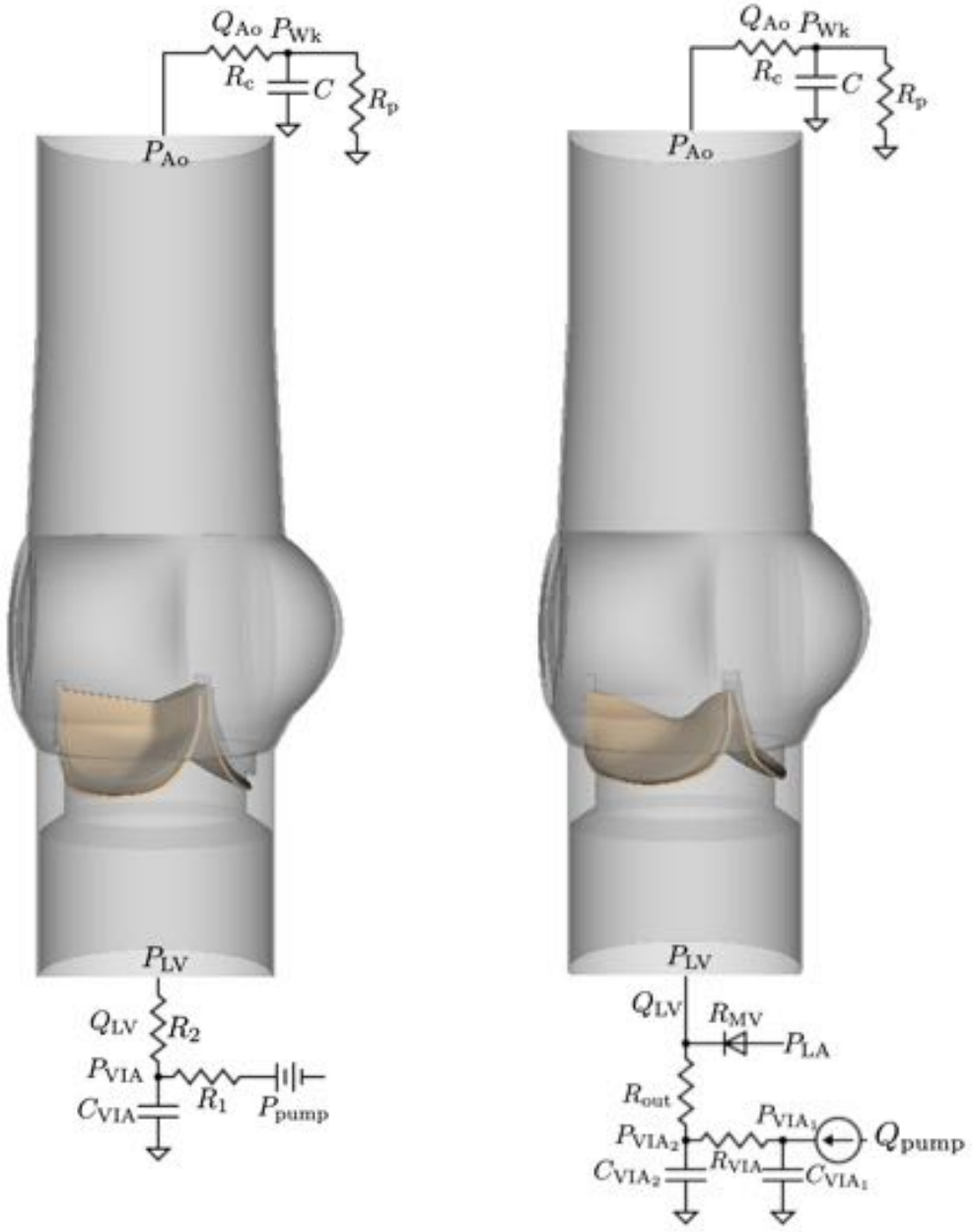

(a) **(b)**

Figure 3: Three-dimensional aortic test section models for the porcine (a) and bovine pericardial (b) BHV simulations along with the reduced-order models that provide driving and loading conditions. Three-element Windkessel models are used at the downstream (outlet) for both cases. (a) A three-element Windkessel model is used at the upstream (inlet) for the porcine aortic valve simulations. The pump pressure is derived from pressure and flow data from the ventricular outflow tract of the pulse duplicator. (b) Because the pump flow waveform and atrial pressure data are available for the bovine pericardial valve experiments, a more detailed pump model is used upstream for the bovine pericardial valve simulations.

Three-element Windkessel (R–C–R) models establish downstream loading conditions for the aortic test section for both cases (Fig. 3). A three-element Windkessel model is also used for the porcine BHV simulations to capture the upstream driving conditions for the aortic test section (Fig. 3a). Additional data are

available for the bovine pericardial case, including the experimental pump flow and atrial pressure waveforms, which allow for a more complete description of the upstream components of the system (Fig. 3b). In both cases, we impose a combination of normal traction and zero tangential velocity boundary conditions at the inlet and outlet of the FSI model to couple the reduced-order models to the detailed description of the flow within the aortic test section. The values of the resistances and compliance for the upstream model are $C_{\mathrm{VIA}} = 0.1$ mmHg mL^{-1}, $R_1 = 0.15$ mmHg mL^{-1} s, and $R_2 = 0.15$ mmHg mL^{-1} s for the porcine aortic valve case, which characterize compliance and resistance of the VIA system. The values for the bovine pericardial valve case are $C_{\mathrm{VIA}_1} = 0.0275$ mmHg mL^{-1}, $C_{\mathrm{VIA}_2} = 0.0347$ mmHg mL^{-1}, $R_{\mathrm{VIA}} = 0.15$ mmHg mL^{-1} s, and $R_{\mathrm{out}} = 0.0898$ mmHg mL^{-1} s. The mitral valve is modeled as a diode, with a resistance of $R_{\mathrm{MV}} = 0.0280$ mmHg mL^{-1} s when the valve is open. The values for the downstream model are $R_{\mathrm{c}} = 0.0218$ mmHg mL^{-1} s, $R_{\mathrm{p}} = 1.31$ mmHg mL^{-1} s, and $C = 0.915$ mmHg mL^{-1} for the porcine BHV, and $R_{\mathrm{c}} = 0.0282$ mmHg mL^{-1} s, $R_{\mathrm{p}} = 1.22$ mmHg mL^{-1} s, and $C = 1.27$ mmHg mL^{-1} for the bovine pericardial BHV. Supplemental Materials Section C provides additional details. We use solid wall (zero velocity) boundary conditions on the remainder of the boundaries in the computational domain of the FSI model.

2.4 Fluid–Structure Interaction

We use a finite element (FE) extension of the IB method [49] to simulate FSI. Supplemental Materials Section D provides details on the continuum formulation and numerical approximations. Reduced-order boundary condition models are coupled to the FSI model following the approach detailed by Griffith et al. [16]

2.5 Numerical Discretizations

Simulations are performed using a geometrically realistic model of the aortic test section of the pulse duplicator with length 10.1 cm and diameter 28 mm (see Fig. 3). The aortic test section is embedded in a square computational domain with side lengths of 10.1 cm. In our IB formulation, Eulerian variables are approximated using a block-structured adaptively refined Cartesian grid, and Lagrangian variables are approximated using an unstructured FE mesh that conforms to the geometry of the structure [49]. The effective fine-grid resolution of the Cartesian grid is approximately 0.39 mm. The structural meshes use second-order hexahedral (27-point) elements for the BHV leaflets and first-order tetrahedral (4-point) elements for the aortic test section. The aortic test section and porcine BHV meshes were generated using Trelis (Computational Simulation Software, LLC, American Fork, UT, USA), and the bovine pericardial BHV mesh was generated using Pointwise (Pointwise, Inc., Ft. Worth, TX, USA). The average grid-spacings of the meshes are 0.4 mm for the aortic test section, 0.59 mm for the porcine aortic valve, and 0.75 mm for the bovine pericardial valve. We use a piecewise-linear kernel for the aortic test section and a three-point B-spline kernel for the valve leaflets as regularized delta functions (see Supplemental Materials Section D). The time step size starts at $\Delta t = 7.5 \times 10^{-6}$ s, and it is systematically reduced if needed to avoid instabilities related to our time stepping scheme. The penalty parameters c_{wall} and κ_{wall} in Eqs. (7) and (8) detailed in the "Aortic Test Section" section are empirically determined as approximately the largest values allowed by our explicit time stepping algorithm at the time step sizes used in the simulations. Supplemental Materials Section F shows results from a grid convergence study to quantify the level of consistency in our numerical results and to justify the chosen level of grid resolution for the final results reported here.

2.6 Software Infrastructure

FSI simulations use the IBAMR software infrastructure, which is a distributed-memory parallel implementation of the IB method with adaptive mesh refinement (AMR) [50, 51]. IBAMR uses SAMRAI [52] for Cartesian grid discretization management, libMesh [53] for finite element discretization management, and PETSc [54] for linear solver infrastructure.

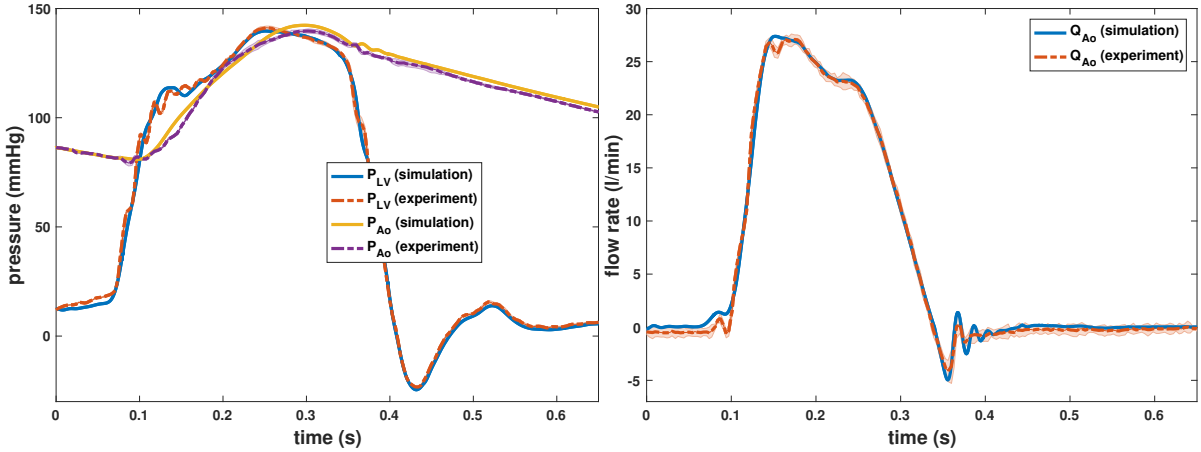

(a) Porcine aortic valve

(b) Porcine aortic valve

(c) Bovine pericardial valve

(d) Bovine pericardial valve

Figure 4: Comparisons between simulated and experimental pressure and flow rate waveforms for the porcine aortic valve (a)-(b) and bovine pericardial valve (c)-(d). The experimental waveforms shown are the average waveforms over 10 consecutive cycles of data, with shaded regions showing where 95% of the data fall. The experimental and computational stroke volumes for the porcine aortic valve are 69.4 ± 0.4 mL and 72.7 mL, respectively, and 71.6 ± 0.7 mL and 72.1 mL for the bovine pericardial valve. The maximum experimental pressure differences during forward flow for the porcine aortic and bovine pericardial valve are 22.8 ± 0.2 mmHg and 19.7 ± 0.5 mmHg, respectively. The maximum computational pressure differences during forward flow are 22.4 mmHg and 16.4 mmHg, respectively.

3 Results

We perform corresponding experiments and simulations using a pulse rate of 70 beats per minute in all cases. We use 10 consecutive cycles of experimental pressure and flow rate waveforms for both valves to characterize the reduced-order models that provide driving and loading conditions for the three-dimensional FSI models. The stroke volumes of the average flow waveforms are 69.4 ± 0.4 mL and 71.6 ± 0.7 mL for the porcine and bovine pericardial BHVs, respectively. We assess the computational results by comparisons to available experimental data, including flow rates, upstream and downstream pressures, and leaflet kinematics. The computational models also provide detailed flow patterns and leaflet stress distributions, which are not readily available in the present experimental models.

Figure 4 shows comparisons between simulated and experimental pressures and flow rates for both valves, which are in good agreement. To quantify this, we calculate the discrepancy between the simulation data

Table 1: Comparisons of normalized L^2- and L^∞-norms of discrepancies in the bulk measurements between simulation and experiment*

	porcine (L^2)	pericardial (L^2)	porcine (L^∞)	pericardial (L^∞)
P_{LV}	3.4%	4.6%	8.6%	14.4%
P_{Ao}	1.9%	1.4%	4.5%	3.6%
Q_{Ao}	4.7%	8.6%	9.5%	20.2%

* Comparisons of L^2- and L^∞-norms of the discrepancies in the bulk measurements from simulation and experiment shown in Figure 4, normalized by the L^2- and L^∞-norms of the measurements from the experiment.

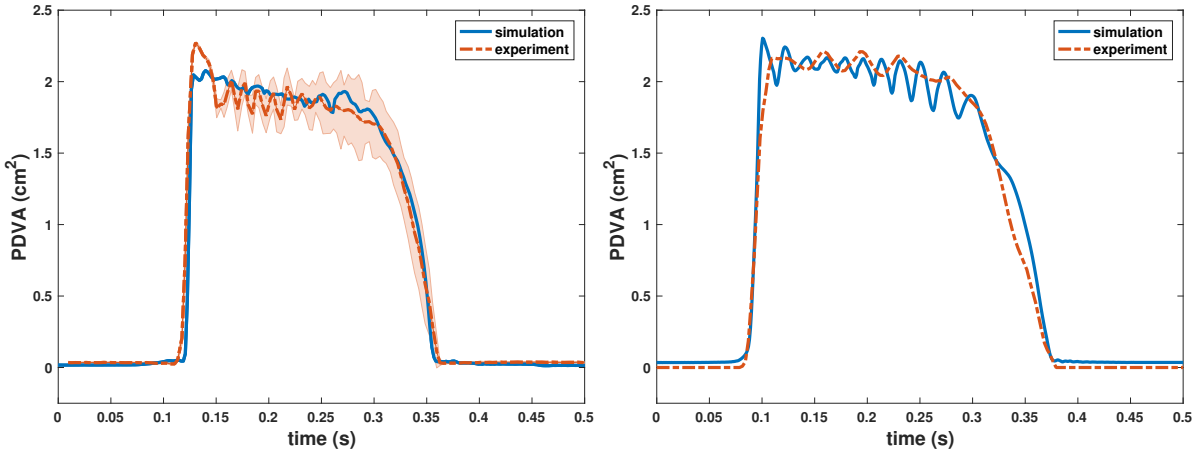

(a) Porcine aortic valve **(b)** Bovine pericardial valve

Figure 5: Comparisons between simulated and experimental projected dynamic valve area (PDVA) for the porcine aortic (a) and bovine pericardial (b) valves. (a) The experimental data (acquired using custom apparatus depicted in Fig. 1b) are manually aligned with the beginning of the valve opening with the simulation data. The experimental PDVA measurement shown is the average PDVA over 10 consecutive cycles of data with shaded region showing where 95% of the data fall. (b) The experimental data are acquired using a high-speed videographic method, from which we reconstruct PDVA data via automatic image analysis via DataTank. Videographic data are available for only a single cycle for the pericardial BHV.

and the mean experimental data by

$$\Delta M_q = \frac{\left\| M^{\mathrm{simulation}} - M^{\mathrm{experiment}} \right\|_{L^q(0,T)}}{\left\| M^{\mathrm{experiment}} \right\|_{L^q(0,T)}}, \qquad q = 2, \infty, \tag{9}$$

in which $(0, T)$ indicates an integral over time and $M^{\mathrm{experiment}}$ is the experimental data averaged over 10 consecutive cycles. Comparisons are shown in Table 1.

The computational stroke volumes are 72.7 mL and 72.1 mL for the porcine and bovine pericardial BHVs, which are 4.68% and 0.71% larger than the mean experimental stroke volumes, respectively. The maximum experimental pressure differences during forward flow for the porcine aortic and bovine pericardial valves are 22.8 ± 0.2 mmHg and 19.7 ± 0.5 mmHg, respectively. The maximum computational pressure differences during forward flow are 22.4 mmHg and 16.4 mmHg, which correspond to differences of 2.0% and 16.5% compared to the experimental pressure difference in the mean pressure waveforms.

Figure 5 uses PDVA to compare the leaflet kinematics in the experimental and computational models. The experimental data are systematically shifted in time to align with the simulation data at the beginning of valve opening. The timing of opening and closing are in excellent agreement, and the open area is also in

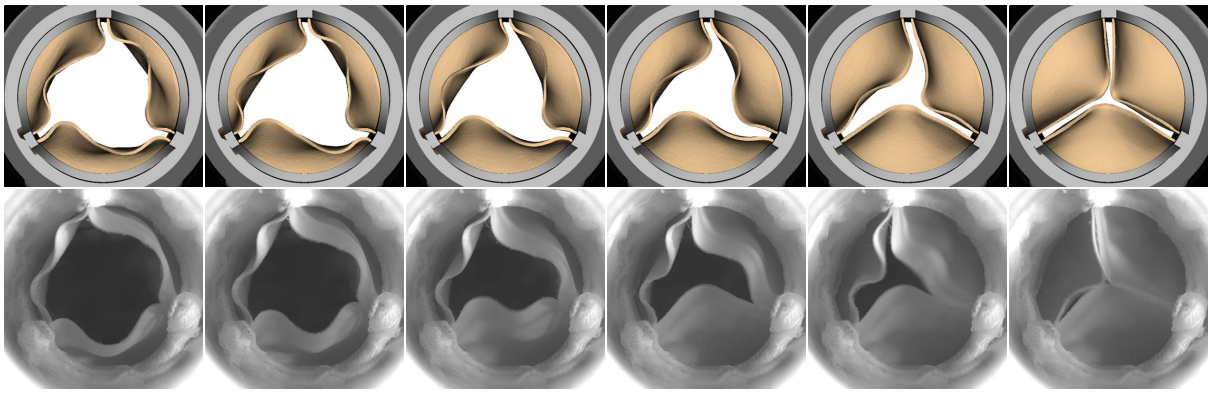

Figure 6: Detailed comparison of the bovine pericardial valve leaflet kinematics during closure from simulation (top) and experiment (bottom). The simulation captures the behavior of each of the leaflets closing one at a time (order: bottom → right → left leaflet) as observed in the experiment. The time increment between frames for simulation is 9.6 ms.

excellent agreement. There are some differences in the fluttering frequency, and we discuss potential sources of these discrepancies in the "Discussion" section.

Figure 6 compares the leaflet kinematics of the bovine pericardial valve during closure in our simulation to images acquired via high-speed videography. We observe that each of the leaflets close one at a time in the experiment as well as in the simulation.

Figure 7 provides detailed flow patterns generated in the FSI simulations of the porcine aortic (Fig. 7a) and bovine pericardial (Fig. 7b) BHVs. We observe that the large-scale flow features are similar in both cases. We classify the flow regime of our simulations by computing the peak Reynolds number Re_{peak},

$$Re_{\text{peak}} = \frac{\rho Q_{\text{peak}} D}{\mu A}, \tag{10}$$

in which ρ is the density, Q_{peak} is the peak flow rate, D is the diameter of the aortic test section, μ is the dynamic viscosity of the fluid, and A is the cross-sectional area of the aortic test section. Re_{peak} is 20,576 and 19,330 for the porcine tissue and bovine pericardial BHV, respectively.

We also compare the leaflet kinematics of the porcine tissue (Figs. 8a and 9a) and bovine pericardial (Figs. 8b and 9b) valves. One important difference between the two valves is the symmetry breaking in the pericardial leaflets, especially during closure. Because of the asymmetric fiber architecture in each of its leaflets, the bovine pericardial valve shows a swirling motion during closure, as also observed in real pericardial BHVs [55].

Differences between the porcine valve and bovine pericardial valve resulting from different fiber architectures are also clear in the stress distributions (Fig. 10). The von Mises stresses on the valves are distributed according to the anisotropic material responses. The porcine valve shows a stress distribution that is aligned from commissure to commissure when the valve is loaded in diastole (Fig. 10a). The stress is also distributed symmetrically on each porcine leaflet during valve opening (Fig. 10c), which is again concentrated around the commissures. In contrast, the bovine pericardial valve shows an asymmetric stress distribution, and the von Mises stresses are concentrated at one of each leaflet's commissures. The location where stress is the highest on the leaflet occurs where the fibers collect at the commissures (Fig. 10b). The opposite is true during valve opening, when the highest leaflet stresses occur near the free edges of the leaflets (Fig. 10d). These patterns appear because the parts of the leaflets with less commissural support experience larger deformations.

4 Discussion

This study has developed FSI models of BHVs in an experimental pulse-duplicator platform. Our leaflet models include anisotropic descriptions of the leaflet biomechanics that are based on experimental tensile test data. In addition, we use experimental pressure and flow data obtained from the pulse-duplicator systems

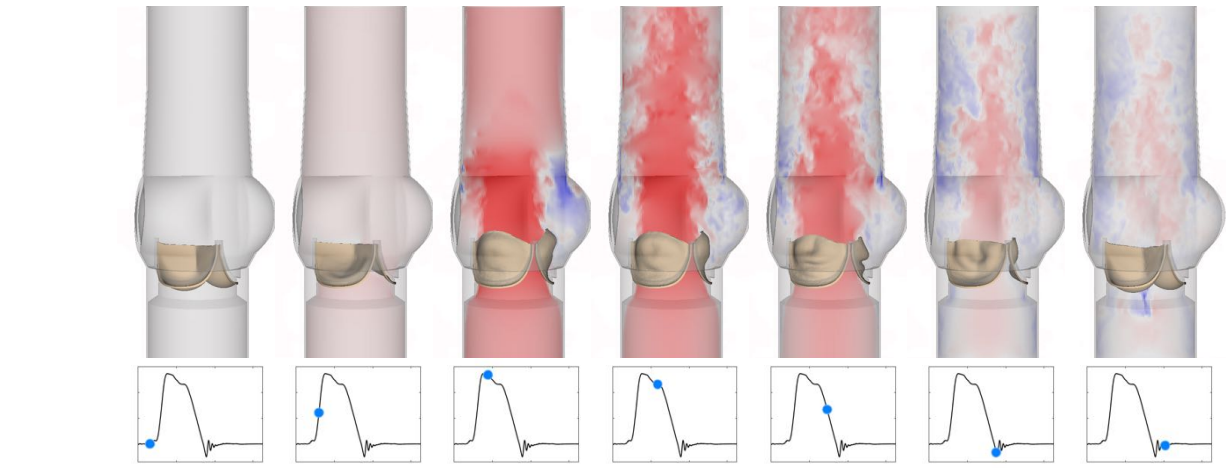

(a) Porcine aortic valve

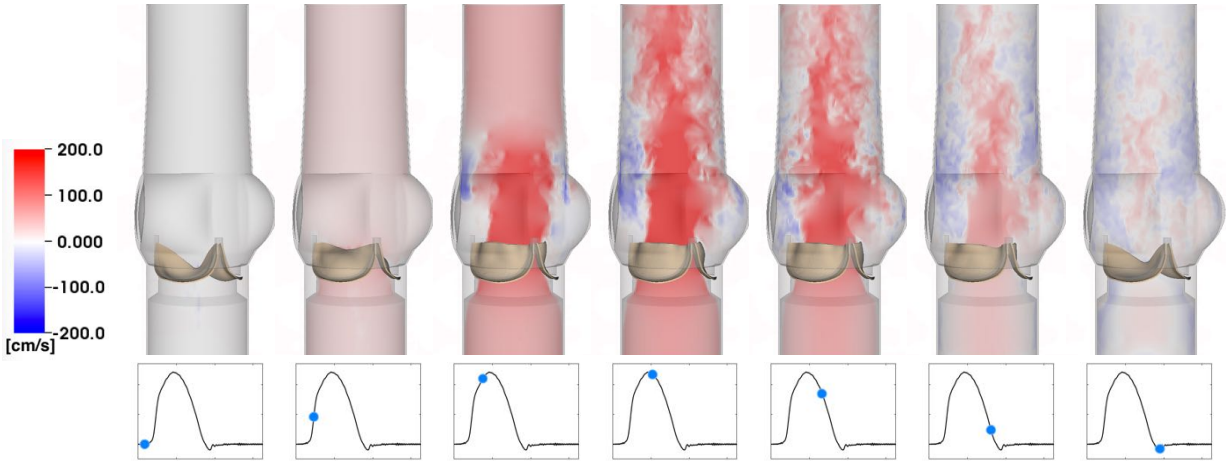

(b) Bovine pericardial valve

Figure 7: Cross-section view of simulated flow patterns using the porcine aortic (a) and bovine pericardial (b) valve models. The color shows the axial velocity through the aortic test section at the center plane, with red indicating forward flow and blue indicating reverse flow. (a) $Re_{\text{peak}} = 20{,}576$. (b) $Re_{\text{peak}} = 19{,}330$. The time increment between frames is 57.6 ms.

to establish realistic boundary models for the detailed FSI models. These boundary models are calibrated in isolation from the rest of the system, independent of the FSI model of the valves. The simulated pressures, flow rates, and leaflet kinematics all emerge from integrating these three model components, and the motion of the leaflets, including the timing of valve opening and closing, is not prescribed. Further, because the flow rate is not imposed in the model, and because the time-dependent configuration of the valve determines the resistance of the aortic test section, achieving both pressures and flow rates that are in good agreement with the experimental data represents a nontrivial test of the model.

The numerical results detailed in Figure 4 show excellent agreement in flow rates, pressures, valve open areas, and the timing of valve opening and closure between the simulations and experiments. For instance, the experimental flow rate oscillations that are present during valve closure in the porcine aortic valve (Fig. 4b) are physical because they come from the interaction between the momentum of the fluid and the compliance of the system, and these oscillations are captured by the computational model. We observe from the bovine pericardial BHV case that a more comprehensive reduced-order model of the upstream components of the pulse-duplicator system, including the pump, VIA, left ventricle, left atrium, and mitral valve, allows us to capture system dynamics, including closure (Fig. 4d), more completely. Table 1 shows the L^2- and L^∞-

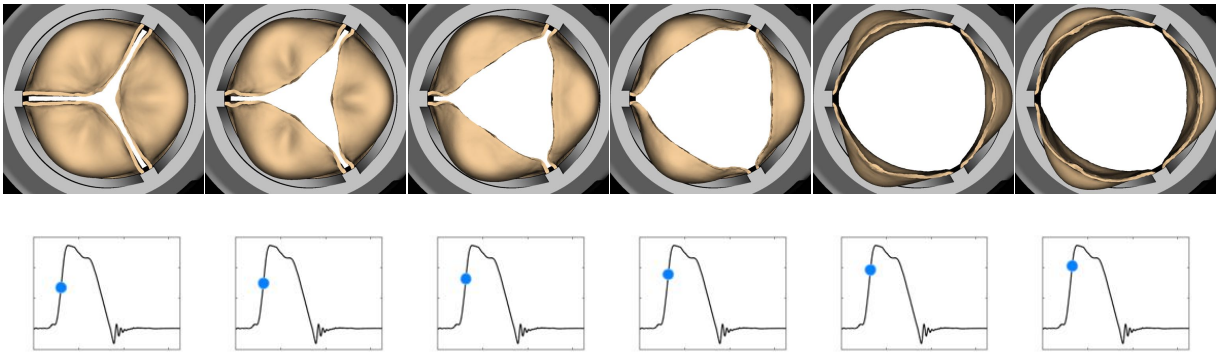

(a) Porcine aortic valve

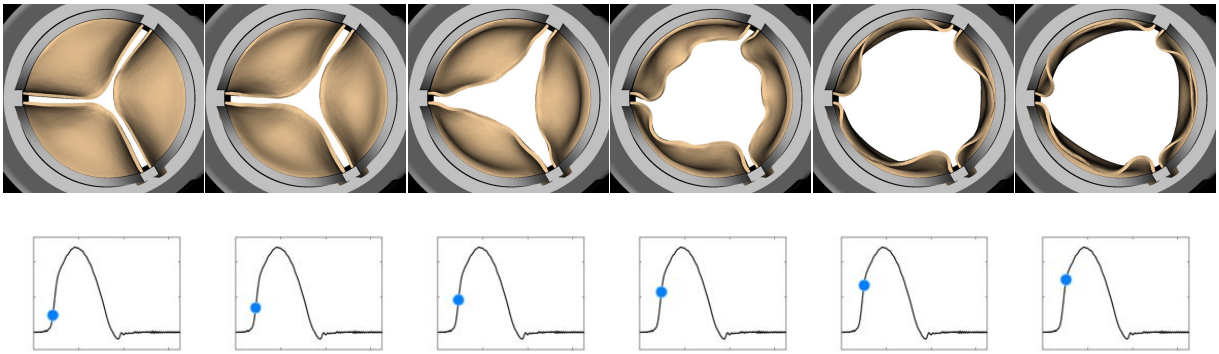

(b) Bovine pericardial valve

Figure 8: Leaflet kinematics of the porcine aortic (a) and bovine pericardial (b) valves during opening. (a) The time increment between frames is 1.92 ms. (b) The time increment between frames is 3.84 ms.

norms of the discrepancies in the simulation results relative to the experimental measurements. In particular, the L^2-differences demonstrate good quantitative agreement, in which the relative discrepancies are within 4.7% for the porcine aortic valve and 8.6% for the bovine pericardial valve. These results show that our valve models generate leaflet kinematics that yield realistic pressures and flow rates in the fully coupled FSI models.

The experimental and computational leaflet kinematics are assessed using PDVA (Figs. 5a and 5b). The PDVA measurements for the porcine aortic valve indicate reasonable agreement between simulations and experiments. There is a key difference in the techniques used to acquire these data. An electro-optical system (Fig. 1b) was used to measure PDVA directly for the porcine aortic valve. For the bovine pericardial valve, PDVA was calculated indirectly using automatic image analysis via DataTank from videographic images. An advantage of the electro-optical subsystem is that it is calibrated with a reference area at the same location as the valve in the test section, but high-speed video is not available for this system. In contrast, although high-speed video is available for the pericardial BHV as shown in Figure 6, the image analysis method uses an estimated area-to-pixel scaling. In addition, the frame rate (400 fps) of the high-speed video of bovine pericardial valve is not sufficient to capture the full dynamic response. Consequently, we are missing data needed to resolve the full dynamic waveform. We plan to use higher speed ($\geq$ 5000 fps) videography in future work to quantify leaflet motion more completely. An important limitation of the present model is that we do observe discrepancies between the computational and experimental leaflet fluttering frequencies and amplitudes. BHVs are known to be viscoelastic [56], and fully viscoelastic models may be needed to achieve better agreement between simulation and experiment. At present, however, experimentally constrained viscoelastic models of BHV biomaterials suitable for three-dimensional mechanical analyses appear to be lacking. The structural models could be improved by incorporating additional experimental data that characterize the flexural properties of the valve leaflets.

Detailed comparisons of the leaflet kinematics for the bovine pericardial BHV showed that the leaflets

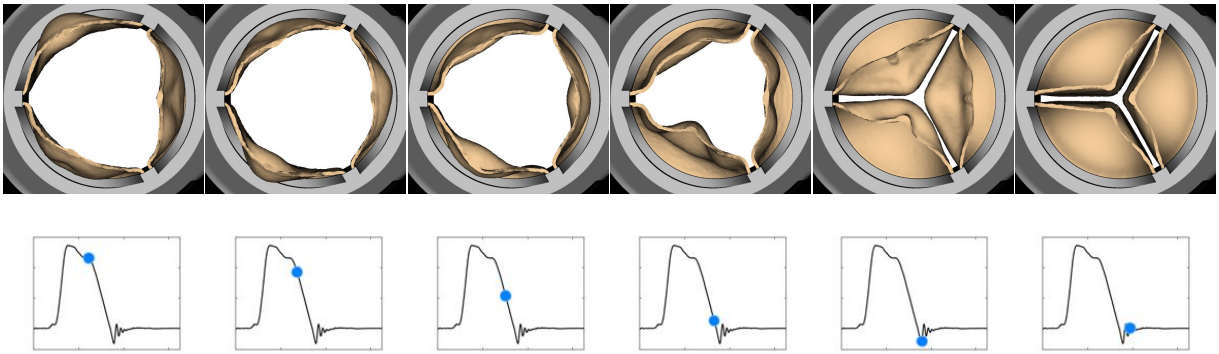

(a) Porcine aortic valve

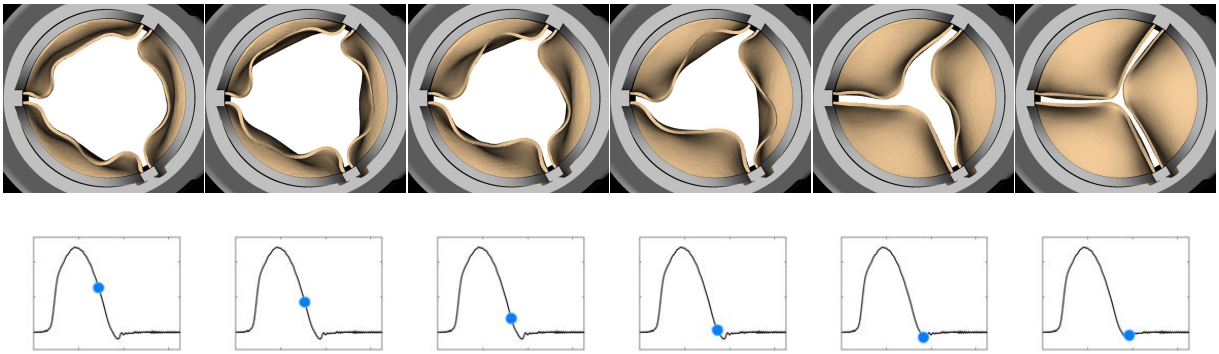

(b) Bovine pericardial valve

Figure 9: Leaflet kinematics of the porcine aortic (a) and bovine pericardial (b) valves during closure. (a) The time increment between frames is 9.6 ms. (b) The time increment between frames is 19.2 ms.

closed one at a time both in the experiment and simulation (Fig. 6). This result indicates that the overall kinematics are in reasonable agreement between the experiment and our model. We speculate that this may be because each of the leaflets has slightly different size and geometric features, along with the contribution from its fiber structure. Alternatively, flow instabilities may induce the sequential closure of the valve leaflets.

The large-scale flow features for the porcine aortic and bovine pericardial valves are similar (Fig. 7). We also observe additional small-scale turbulent flow features at current spatial resolutions, which are also present in physiological flow regimes [57]. Re_{peak} for both cases is approximately 20,000, which clearly motivates the need for further studies on the treatment of turbulence in these types of models. In the present study, we perform implicit large-eddy simulation (ILES) using high-resolution slope limiters, based on the piecewise parabolic method (PPM) [58–61], to model the flow field. Explicit LES methods have not yet been completely developed for the present IB approach to FSI. We plan to compare ILES [58–61] and explicit LES [62, 63] models for cardiovascular flows in future work. The similarity in the large-scale flow features for the two BHVs suggests that it is important to consider the leaflet kinematics in addition to the flow patterns in comparing different BHVs. Studying leaflet kinematics could also be important in identifying the factors that affect the durability of different BHVs.

Differences in the porcine and bovine pericardial leaflet kinematics are particularly prominent during leaflet closure (Figs. 8 and 9). Specifically, the twisting motion during closure that we see in the bovine pericardial valve results from the asymmetric alignment of its fibers. This is also evident in stress analyses of the leaflets. Differences in stress distributions (Fig. 10) are caused by the reduced strain at one of two commissure points of each of the bovine pericardial leaflets, whereas the stress distributions in the porcine BHV model reflects the symmetric fiber architecture of the porcine valve cusps. Also, unlike the porcine aortic valve, the pericardial valve lacks nodes of Arantius, which are intrinsic anatomic structures in native aortic valve leaflets. It has been hypothesized that the nodes may play a role in distributing and equalizing leaflet closing stresses [64]. We also observe that the porcine BHV leaflets experience higher stresses, which

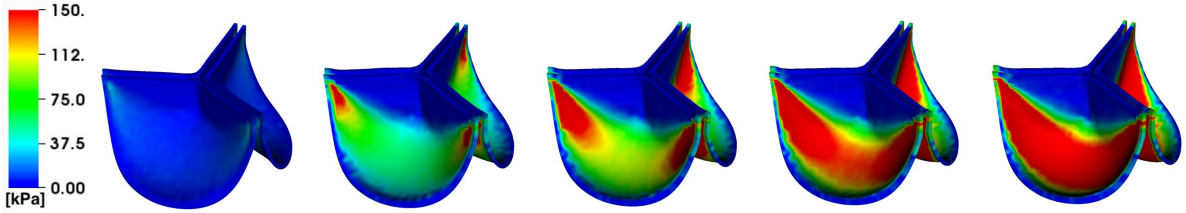

(a) Porcine aortic valve (diastole)

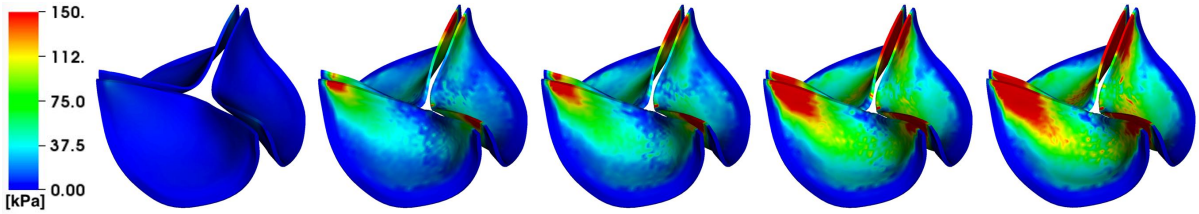

(b) Bovine pericardial valve (diastole)

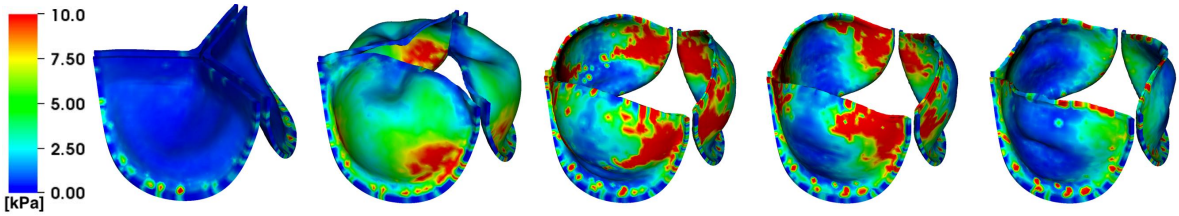

(c) Porcine aortic valve (systole)

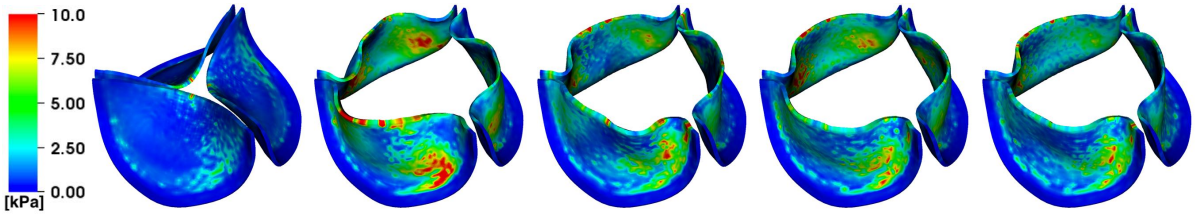

(d) Bovine pericardial valve (systole)

Figure 10: von Mises stress (kPa) on the porcine aortic (a), (c) and bovine pericardial (b), (d) valves during diastole (a)-(b) and systole (c)-(d). The time increment between frames in panels (a)-(b) is 30.72 ms, and the time increment between frames in panels (c)-(d) is 11.52 ms.

may also explain why porcine BHVs have a greater tendency to develop leaflet tears with regurgitation compared to bovine pericardial BHV [65, 66]. The stress concentrations at the commissures of the bovine pericardial BHV also agrees with the known failure regions for bovine pericardial BHVs [67, 68].

The present study has several limitations. Although we report 10 consecutive cycles of experimental data, one future aim is to better quantify the uncertainty associated with cycle-to-cycle variability in the experiments, and to integrate this uncertainty into our computational models. We shall also quantify variability in the leaflet kinematics along with variability in the pressure and flow rate measurements by collecting high-speed video and data over multiple cycles. We also have not yet systematically performed sensitivity analysis or uncertainty quantification of the model. Performing such analyses is crucial for establishing the credibility of the model but is challenging because of the substantial computational requirements of such analyses. We also plan to validate the flow fields by particle image velocimetry (PIV) under different conditions, as well as using a blood analogue (dynamic viscosity of 3–4 cP) as our test fluid. With PIV, we also plan to perform direct comparison between computational and experimental flows in steady state cases in which we expect to obtain converged mean flows. This will help us quantify the accuracy our model by comparing time-averaged flows as well as turbulence kinetic energies to compare both large- and small-scale flow features to those of the experiments. In this study, we also use homogeneous structural models that

omit descriptions of the discrete layers of the valve leaflets, which will affect how the leaflets deform [69,70]. Therefore we shall also further validate specifically the leaflet kinematics by focusing on quasi-static BHV deformations, as done by Sun et al. [28], or by comparing the leaflet kinematics with reconstructions of leaflet deformations from in vitro experiments, as done by Iyengar et al. [27] or Sugimoto et al. [71]. Other potential validation tests include assessing BHV performance using additional hydrodynamics performance measures (pressure drop, effective orifice area, etc.) [72–74].

In summary, this study describes work to model BHVs in an experimental pulse-duplicator platform that is used in various settings to assess their performance. Ultimately, fully validated FSI models of BHVs may be used to develop a high-fidelity model for predicting dynamic performance amongst different valve designs and addressing persistent challenges posed by current BHV designs. They could also facilitate matching patient requirements with valve performance specifics and the development of regulatory guidelines for evaluation of novel designs. This methodology may also be extended and further validated to be applicable to study the effectiveness of TAVR devices with varying degrees of intra- and paravalvular leak, reduced leaflet mobility, subclinical valve thrombosis, and potential pannus formation [75].

Acknowledgment

J.H.L. acknowledges funding from the NIH Integrative Vascular Biology Training Fellowship (5T32HL069768-17) at the University of North Carolina School of Medicine. B.E.G. acknowledges funding from NSF (Awards OAC 1450327, OAC 1652541, and CBET 1757193) and NIH (Awards R01HL117063 and U01HL143336). Thanks to B. Vadala-Roth for providing data for Supplemental Materials Section E, and to K. Aycock and T. Morrison for reviewing the manuscript. The findings and conclusions in this article have not been formally disseminated by the U.S. FDA and should not be construed to represent any agency determination or policy. The mention of commercial products, their sources, or their use in connection with material reported herein is not to be construed as either an actual or implied endorsement of such products by the Department of Health and Human Services.

Conflict of interest

No conflict of interest.

References

[1] L. P. Dasi, H. A. Simon, P. Sucosky, A. P. Yoganathan, Fluid mechanics of artificial heart valves, Clin Exp Pharmacol Physiol 36 (2) (2009) 225–237.

[2] T. Rodriguez-Gabella, P. Voisine, R. Puri, P. Pibarot, J. Rodés-Cabau, Aortic Bioprosthetic Valve Durability: Incidence, Mechanisms, Predictors, and Management of Surgical and Transcatheter Valve Degeneration, J Am Coll Cardiol 70 (8) (2017) 1013–1028.

[3] R. F. Siddiqui, J. R. Abraham, J. Butany, Bioprosthetic heart valves: modes of failure, Histopathology 55 (2) (2009) 135–144.

[4] T. M. Morrison, M. L. Dreher, S. Nagaraja, L. M. Angelone, W. Kainz, The role of computational modeling and simulation in the total product life cycle of peripheral vascular devices, J Med Device 11 (2) (2017) 024503.

[5] Regulatory Science Priorities (FY2017), Tech. rep., U.S. Food and Drug Administration Center for Devices and Radiological Health (2016).
URL https://www.fda.gov/downloads/MedicalDevices/ScienceandResearch/UCM521503.pdf

[6] N. Duraiswamy, J. D. Weaver, Y. Ekrami, S. M. Retta, C. Wu, A parametric computational study of the impact of non-circular configurations on bioprosthetic heart valve leaflet deformations and stresses: possible implications for transcatheter heart valves, Cardiovasc Eng Technol 7 (2) (2016) 126–138.

[7] ASME V&V 40-2018, Assessing Credibility of Computational Modeling Through Verification and Validation: Application to Medical Devices (2018).

[8] A. P. Yoganathan, K. B. Chandran, F. Sotiropoulos, Flow in prosthetic heart valves: state-of-the-art and future directions, Ann Biomed Eng 33 (12) (2005) 1689–1694.

[9] R. Zakerzadeh, M.-C. Hsu, M. S. Sacks, Computational methods for the aortic heart valve and its replacements, Expert Rev Med Devices 14 (11) (2017) 849–866.

[10] A. M. Bavo, G. Rocatello, F. Iannaccone, J. Degroote, J. Vierendeels, P. Segers, Fluid–structure interaction simulation of prosthetic aortic valves: comparison between immersed boundary and arbitrary Lagrangian–Eulerian techniques for the mesh, PLoS ONE 11 (4) (2016) e0154517.

[11] J. H. Spühler, J. Jansson, N. Jansson, J. Hoffman, 3D fluid-structure interaction simulation of aortic valves using a unified continuum ALE FEM model, Front Physiol 16 (9) (2018) 363.

[12] C. S. Peskin, The immersed boundary method, Acta Numer 11 (2002) 479–517.

[13] C. S. Peskin, Flow patterns around heart valves: a numerical method, J Comput Phys 10 (2) (1972) 252–271.

[14] C. S. Peskin, Numerical analysis of blood flow in the heart, J Comput Phys 25 (3) (1977) 220–252.

[15] B. E. Griffith, N. A. Patankar, Immersed method for fluid–structure interaction, Annu Rev Fluid Mech 52.

[16] B. E. Griffith, X. Y. Luo, D. M. McQueen, C. S. Peskin, Simulating the fluid dynamics of natural and prosthetic heart valves using the immersed boundary method, Int J Appl Mech 1 (1) (2009) 137–177.

[17] B. E. Griffith, Immersed boundary model of physiological driving and loading conditions, Int J Numer Methods Biomed Eng 28 (3) (2012) 317–345.

[18] I. Borazjani, Fluid–structure interaction, immersed boundary-finite element method simulations of bioprosthetic heart valves, Comput Methods Appl Mech Eng 257 (0) (2013) 103–116.

[19] A. Gilmanov, H. Stolarski, F. Sotiropoulos, Flow–structure interaction simulations of the aortic heart valve at physiologic conditions: The role of tissue constitutive model, J Biomech Eng 140 (4) (2018) 041003.

[20] V. Flamini, A. DeAnda, B. E. Griffith, Immersed boundary-finite element model of fluid–structure interaction in the aortic root, Theor Comput Fluid Dyn 30 (1) (2016) 139–164.

[21] A. Hasan, E. M. Kolahdouz, A. Enquobahrie, T. G. Caranasos, J. P. Vavalle, B. E. Griffith, Image-based immersed boundary model of the aortic root, Med Eng Phys 47 (2017) 72–84.

[22] J. de Hart, G. W. M. Peters, P. J. G. Schreurs, F. P. T. Baaijens, Collagen fibers reduce stresses and stabilize motion of aortic valve leaflets during systole, J Biomech 37 (3) (2004) 303–311.

[23] M.-C. Hsu, D. Kamensky, F. Xu, J. Kiendl, C. Wang, M. C. H. Wu, J. Mineroff, A. Reali, Y. Bazilevs, M. S. Sacks, Dynamic and fluid-structure interaction simulations of bioprosthetic heart valves using parametric design with T-splines and Fung-type material models, Comput Mech 55 (6) (2015) 1211–1225.

[24] D. Kamensky, M.-C. Hsu, D. Schillinger, J. A. Evans, A. Aggarwal, Y. Bazilevs, M. S. Sacks, T. J. Hughes, An immersogeometric variational framework for fluid–structure interaction: application to bioprosthetic heart valves, Comput Methods Appl Mech Eng 284 (2015) 1005–1053.

[25] F. Xu, S. Morganti, R. Zakerzadeh, D. Kamensky, F. Auricchio, A. Reali, T. J. R. Hughes, M. S. Sacks, M.-C. Hsu, A framework for designing patient-specific bioprosthetic heart valves using immersogeometric fluid–structure interaction analysis, Int J Numer Method Biomed Eng 34 (4) (2018) e2938.

[26] M. C. H. Wu, R. Zakerzadeh, D. Kamensky, J. Kiendl, M. S. Sacks, M.-C. Hsu, An anisotropic constitutive model for immersogeometric fluid–structure interaction analysis of bioprosthetic heart valves, J Biomech 74 (2018) 23–31.

[27] A. K. S. Iyengar, H. Sugimoto, D. B. Smith, M. S. Sacks, Dynamic in vitro quantification of bioprosthetic heart valve leaflet motion using structured light projection, Ann Biomed Eng 29 (11) (2001) 963–973.

[28] W. Sun, A. Abad, M. S. Sacks, Simulated bioprosthetic heart valve deformation under quasi-static loading simulated bioprosthetic heart valve deformation under quasi-static loading, J Biomech Eng 127 (2005) 905–914.

[29] W. Mao, K. Li, W. Sun, Fluid–structure interaction study of transcatheter aortic valve dynamics using smoothed particle hemodynamics, Cardiovasc Eng Technol 7 (4) (2016) 374–388.

[30] H. S. Kandail, S. D. Trivedi, A. C. Shaikh, T. K. Bajwa, D. P. O'Hair, A. Jahangir, J. F. LaDisa Jr., Impact of annular and supra-annular CoreValve deployment locations on aortic and coronary artery hemodynamics, J Mech Behav Biomed Mater 86 (2018) 131–142.

[31] Y. Chen, H. Luo, A computational study of the three-dimensional fluid–structure interaction of aortic valve, J Fluids Struct 80 (2018) 332–349.

[32] Y. Chen, H. Luo, Pressure distribution over the leaflets and effect of bending stiffness on fluid–structure interaction of the aortic valve, J Fluid Mech 883 (A52) (2020) 1–29.

[33] A. M. Tango, J. Salmonsmith, A. Ducci, G. Burriesci, Validation and extension of a fluid–Structure interaction model of the healthy aortic valve, Cardiovasc Eng Technol 9 (4) (2018) 739–751.

[34] J. Sigüenza, D. Pott, S. Mendez, S. J. Sonntag, T. A. S. Kaufmann, U. Steinseifer, F. Nicoud, Fluid–structure interaction of a pulsatile flow with an aortic valve model: a combined experimental and numerical study, Int J Numer Method Biomed Eng 34 (4) (2018) e2945.

[35] K. L. Billiar, M. S. Sacks, Biaxial mechanical properties of the natural and glutaraldehyde treated aortic valve cusp. Part I: experimental results, J Biomech Eng 122 (1) (2000) 23–30.

[36] K. L. Billiar, M. S. Sacks, Biaxial mechanical properties of the native and glutaraldehyde-treated aortic valve cusp. Part II: a structural constitutive model, J Biomech Eng 122 (4) (2000) 327–335.

[37] H. Kim, K. B. Chandran, M. S. Sacks, J. Lu, An experimentally derived stress resultant shell model for heart valve dynamic simulations, Ann Biomed Eng 35 (1) (2007) 30–44.

[38] L. N. Scotten, R. Siegel, Importance of shear in prosthetic valve closure dynamics, J Heart Valve Dis 20 (2011) 664–672.

[39] S. M. Retta, J. Kepner, S. Marquez, B. A. Herman, M. C. S. Shu, L. W. Grossman, In-vitro pulsatile flow measurement in prosthetic heart valves: an inter-laboratory comparison, J Heart Valve Dis 26 (1) (2017) 72–80.

[40] Cardiovascular Implants – Cardiac Valve Prostheses – Part 3: Heart Valve Substitutes Implanted by Transcatheter Techniques, ISO 5840-3 2013(E).

[41] C. Wu, N. Saikrishnan, A. J. Chalekian, R. Fraser, O. Ieropoli, S. M. Retta, R. Joseph, S. Lee, S. Marquez, D. Mester, N. Pan, S. Vatanpour, C. Weinberg, U. Steinseifer, In-vitro pulsatile flow testing of prosthetic heart valves: a round-robin study by the ISO Cardiac Valves Working Group, Cardiovasc Eng Technol 10 (3) (2019) 397–422.

[42] G. A. Holzapfel, Nonlinear Solid Mechanics: A Continuum Approach for Engineering, 1st Edition, Wiley, 2000.

[43] K. Murdock, C. Martin, W. Sun, Characterization of mechanical properties of pericardium tissue using planar biaxial tension and flexural deformation, J Mech Behav Biomed Mater 77 (2018) 148–156.

[44] T. C. Gasser, R. W. Ogden, G. A. Holzapfel, Hyperelastic modelling of arterial layers with distributed collagen fibre orientations, J R Soc Interface 3 (6) (2006) 15–35.

[45] B. Vadala-Roth, S. Acharya, N. A. Patankar, S. Rossi, B. E. Griffith, Stabilization approaches for the hyperelastic immersed boundary method for problems of large-deformation incompressible elasticity, arXiv preprint arXiv:1811.06620.

[46] N. J. B. Driessen, C. V. C. Bouten, F. P. T. Baaijens, A structural constitutive model for collagenous cardiovascular tissues incorporating the angular fiber distribution, J Biomech Eng 127 (3) (2005) 494–503.

[47] J. Wong, E. Kuhl, Generating fibre orientation maps in human heart models using Poisson interpolation, Comput Methods Biomech Biomed Eng 17 (11) (2014) 1217–1226.

[48] B. Kallemov, A. P. S. Bhalla, B. E. Griffith, A. Donev, An immersed boundary method for rigid bodies, Commun App Math Comput Sci 11 (1) (2016) 79–141.

[49] B. E. Griffith, X. Y. Luo, Hybrid finite difference/finite element immersed boundary method, Int J Numer Methods Biomed Eng 33 (11) (2017) e2888.

[50] B. E. Griffith, R. D. Hornung, D. M. McQueen, C. S. Peskin, An adaptive, formally second order accurate version of the immersed boundary method, J Comput Phys 223 (1) (2007) 10–49.

[51] IBAMR: Immersed Boundary Method Adaptive Mesh Refinement Software Infrastructure.
URL `https://ibamr.github.io/`

[52] R. D. Hornung, S. R. Kohn, Managing application complexity in the SAMRAI object-oriented framework, Concurr Comput Pract Exp 14 (2002) 347–368.

[53] B. S. Kirk, J. W. Peterson, R. H. Stogner, G. F. Carey, `libMesh`: a C++ library for parallel adaptive mesh refinement/coarsening simulations, Eng Comput 22 (3–4) (2006) 237–254.

[54] S. Balay, S. Abhyankar, M. F. Adams, J. Brown, P. Brune, K. Buschelman, L. Dalcin, A. Dener, V. Eijkhout, W. D. Gropp, D. Kaushik, M. G. Knepley, D. A. May, L. C. McInnes, R. T. Mills, T. Munson, K. Rupp, P. Sanan, B. F. Smith, S. Zampini, H. Zhang, H. Zhang, PETSc Users Manual, Tech. Rep. ANL-95/11 - Revision 3.10, Argonne National Laboratory (2018).
URL `http://www.mcs.anl.gov/petsc`

[55] C. Doose, M. Kütting, S. Egron, P. F. Ghalati, C. Schmitz, M. Utzenrath, A. Sedaghat, B. Fujita, T. Schimitz-Rode, S. Ensminger, U. Steinseifer, Valve-in-valve outcome: design impact of a pre-existing bioprosthesis on the hydrodynamics of an Edwards Sapien XT valve, Eur J Cardiothorac Surg 51 (2017) 562–570.

[56] A. Rassoli, N. Faltouraee, R. Guidoin, Structural model of viscoelastic properties of pericardial bioprosthetic valves, Artif Organs 42 (6) (2018) 630–639.

[57] J. A. Funder, M. W. Frost, P. Wierup, K. Klaaborg, V. Hjortdal, H. Nygaard, J. M. Hasenkam, Turbulence downstream of subcoronary stentless and stented aortic valves, J Biomech 44 (2011) 2273–2278.

[58] P. Colella, P. R. Woodward, The piecewise parabolic method (PPM) for gas-dynamical simulations, J Comput Phys 54 (1) (1984) 174–201.

[59] W. J. Rider, J. A. Greenough, J. R. Kamm, Accurate monotonicity- and extrema-preserving methods through adaptive nonlinear hybridizations, J Comput Phys 225 (2) (2007) 1827–1848.

[60] P. Colella, M. D. Sekora, A limiter for PPM that preserves accuracy at smooth extrema, J Comput Phys 227 (15) (2008) 7069–7076.

[61] P. McCorquodale, P. Colella, A high-order finite-volume method for conservation laws on locally refined grids, Commun App Math Comput Sci 6 (1) (2011) 1–25.

[62] P. Sagaut, Large Eddy Simulation for Incompressible Flows, an Introduction, Berlin: Springer, 2014.

[63] L. C. Berselli, T. Iliescu, W. J. Layton, Mathematics of Large Eddy Simulation of Turbulent Flows, Berlin: Springer, 2006.

[64] M. H. Aazami, M. Salehi, The Arantius nodule: a 'stress-decreasing effect', J Heart Valve Dis 14 (4) (2005) 565–566.

[65] M. Arsalan, T. Walther, Durability of prostheses for transcatheter aortic valve implantation, Nat Rev Cardiol 13 (6) (2016) 360–367.

[66] T. Rodriguez-Gabella, P. Voisine, R. Puri, P. Pibarot, J. Rodés-Cabau, Aortic bioprosthetic valve durability: incidence, mechanisms, predictors, and management of surgical and transcatheter valve degeneration, J Am Coll Cardiol 70 (8) (2017) 1013–1028.

[67] P. Singhal, A. Luk, J. Butany, Bioprosthetic heart valves: impact of implantation on biomaterials, ISRN Biomater (2013) 1–14.

[68] C. Martin, W. Sun, Comparison of transcatheter aortic valve and surgical bioprosthetic valve durability: a fatigue simulation study, J Biomech 48 (12) (2015) 3026–3034.

[69] R. M. Buchanan, M. S. Sacks, Interlayer micromechanics of the aortic heart valve leaflet, Biomech Model Mechanobiol 13 (2014) 813–826.

[70] B. V. Rego, M. S. Sacks, A functionally graded material model for the transmural stress distribution of the aortic valve leaflet, J Biomech 54 (2017) 88–95.

[71] H. Sugimoto, M. S. Sacks, Effects of leaflet stiffness on dynamic bioprosthetic heart valve leaflet shape, Cardiovasc Eng Technol 4 (1) (2013) 2–15.

[72] M. Rashtian, D. M. Stevenson, D. T. Allen, A. P. Yoganathan, E. C. Harrison, W. A. Edmiston, S. H. Rahimtoola, Flow characteristics of bioprosthetic heart valves, Chest 98 (2) (1990) 365–375.

[73] S. C. Reimold, A. P. Yoganathan, H. W. Sung, L. H. Cohn, M. G. Sutton, R. T. Lee, Doppler echocardiographic study of porcine bioprosthetic heart valves in the aortic valve position in patients without evidence of cardiac dysfunction, Am J Cardiol 67 (7) (1991) 611–615.

[74] S. Marquez, R. T. Hon, A. P. Yoganathan, Comparative hydrodynamic evaluation of bioprosthetic heart valves, J Heart Valve Dis 10 (6) (2001) 802–811.

[75] E. De Marchena, J. Mesa, S. Pomenti, C. Marin Y Kall, X. Marincic, K. Yahagi, E. Ladich, R. Kutz, Y. Aga, M. Ragosta, A. Chawla, M. E. Ring, R. Virmani, Thrombus formation following transcatheter aortic valve replacement, JACC Cardiovasc Interv 8 (5) (2015) 728–739.

[76] L. Zhang, A. Gerstenberger, X. Wang, W. K. Liu, Immersed finite element method, Comput Methods Appl Mech Engrg 193 (21–22) (2004) 2051–2067.

[77] W. K. Liu, Y. Liu, D. Farrell, L. Zhang, X. S. Wang, Y. Fukui, N. Patankar, Y. Zhang, C. Bajaj, J. Lee, et al., Immersed finite element method and its applications to biological systems, Comput Methods Appl Mech Engrg 195 (13–16) (2006) 1722–1749.

[78] L. T. Zhang, M. Gay, Immersed finite element method for fluid-structure interactions, J Fluids Struct 23 (6) (2007) 839–857.

[79] X. Wang, L. T. Zhang, Interpolation functions in the immersed boundary and finite element methods, Comput Methods Appl Mech Engrg 45 (4) (2010) 321–334.

[80] X. Wang, C. Wang, L. T. Zhang, Semi-implicit formulation of the immersed finite element method, Comput Methods Appl Mech Engrg 49 (4) (2012) 421–430.

[81] B. E. Griffith, An accurate and efficient method for the incompressible Navier–Stokes equations using the projection method as a preconditioner, J Comput Phys 228 (20) (2009) 7565–7595.

[82] B. E. Griffith, On the volume conservation of the immersed boundary method, Commun Comput Phys 12 (2) (2012) 401–432.

[83] S. Reese, M. K. Ussner, B. D. Reddy, A new stabilization technique for finite elements in non-linear elasticity, Int J Numer Meth Biomed Engng 44 (1999) 1617–1652.

[84] J. Bonet, A. J. Gil, R. Ortigosa, A computational framework for polyconvex large strain elasticity, Comput Methods Appl Mech Engrg 283 (2015) 1061–1094.

Supplemental Materials

A Reconstruction of the Bovine Pericardial BHV Geometry

The pericardial valve geometry was reconstructed from micro-CT images of a Carpentier-Edwards PERIMOUNT RSR Model 2800 surgical aortic heart valve. The DICOM files, consisting of approximately 500 slices of the 25 mm valve after micro-CT scanning (Scanco Medical; scan parameters: 90 kV; 88 μA; voxel size 24.6 μm), were imported into Mimics (Materialise Inc., Leuven, Belgium) for further segmentation and reconstruction. Segmentation and reconstruction operations in Mimics involved first thresholding to remove the dense metal and its artifacts from all the slices, and then cavity filling and region growing to reconstruct the continuity in the leaflet material. These operations helped reconstruct the three-dimensional shape of the leaflets. Other segmentation morphology operations were used to ensure that the leaflet thickness was consistent with the measured thickness of the leaflet. After these operations, the leaflet masks were smoothed, wrapped, and smoothed again prior to importing into Materialise 3-matic (Materialise Inc., Leuven, Belgium). Further processing using design tools in Materialise 3-matic was necessary to sketch and sweep edges of the leaflet to create a smooth outline of the entire leaflet.

B Parameter Fitting for the Valve Material Models

We perform model fits for the constitutive model of the valves detailed in the "Leaflet Mechanics" section in the main text using experimental data from Billiar and Sacks [35, 36] for the porcine tissue BHV and from Kim et al. [37] for the bovine pericardial BHV. In the biaxial tests of Billiar and Sacks, the specimens were mounted onto the testing device so that the radial and circumferential directions were aligned with the direction of the applied forces, as shown in Figure S1a. Kim et al. used a stress-control biaxial testing method on a gluteraldehyde-treated bovine pericardial tissue sample. As shown in Figure S1c, the specimen was aligned at 45° to the direction of the applied forces, mimicking the fiber alignment of the pericardial valve leaflets. To determine constitutive model parameters, we assume that the solid is incompressible, compute the second Piola-Kirchhoff stress ($\mathbb{S}$), and compare it to the experimental values for given values of the Green-Lagrange strain $\mathbb{E} = \frac{1}{2}(\mathbb{C} - \mathbb{I})$. The stress is computed by

$$\mathbb{S} = \mathbb{S}^{\text{dev}} - p\mathbb{C}^{-1}, \tag{S1}$$

$$\mathbb{S}^{\text{dev}} = 2\frac{\partial W}{\partial \mathbb{C}}, \tag{S2}$$

$$p = \frac{\mathbb{S}^{\text{dev}}_{33}}{(\mathbb{C}^{-1})_{33}}, \tag{S3}$$

in which $W = W_{\text{iso}} + W_{\text{aniso}}$ is the Holzapfel-Gasser-Ogden model described by (4) and (5) in the "Leaflet Mechanics" section of the main text, $\mathbb{S}^{\text{dev}}$ is the deviatoric part of the second Piola-Kirchhoff stress, $\mathbb{C} = \mathbb{F}^T\mathbb{F}$ is the Cauchy-Green strain, $\mathbb{F}$ is the deformation gradient tensor, and p is the pressure assuming that the specimen is acted on only by in-plane loads. We use lsqcurvefit in MATLAB (The MathWorks, Inc., Natick, MA, USA), a nonlinear least-squares solver, to determine the model parameters. Figures S1b and S1d show constitutive model fits obtained using this approach.

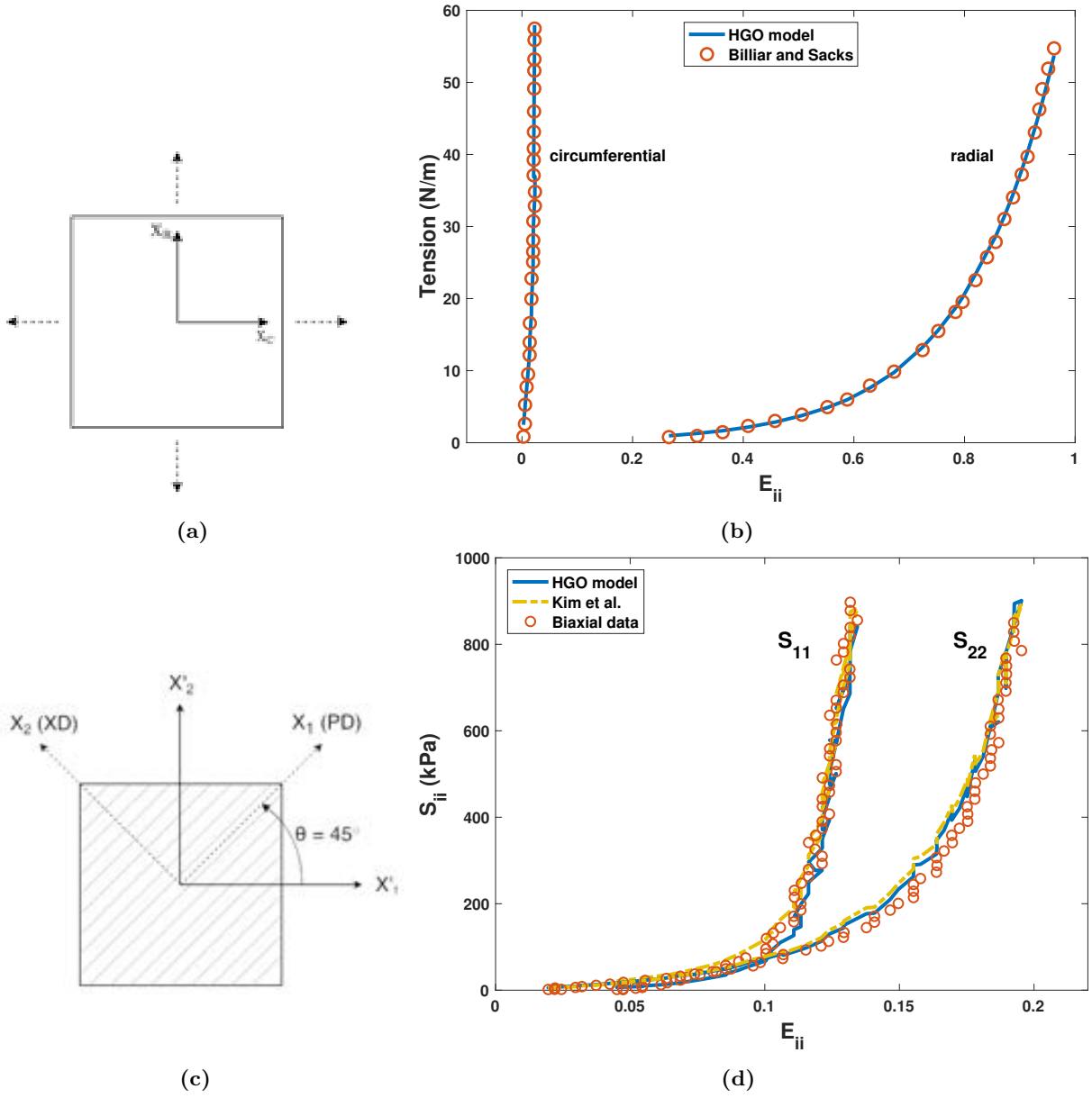

Figure S1: (a) Schematic of the biaxial tensile test of Billiar and Sacks [35, 36] for porcine aortic valve tissue specimens to study their material response. X_C is the circumferential axis, and X_R is the radial axis. The dashed lines are the directions in which forces were applied. (b) Parameter fitting for the porcine aortic valve using the experimental tensile test data from Billiar and Sacks [35, 36] for glutaraldehyde-fixed porcine aortic valves. (c) Schematic of the biaxial tensile tests of Kim et al. [37] for bovine pericardium tissue specimens to study their material response. X_1 is the preferred mean fiber direction (PD) also shown by gray lines, X_2 is the cross-preferred fiber direction (XD), and X_1' and X_2' are the directions in which forces were applied. (d) Parameter fitting for the bovine pericardial valve using the equibiaxial data from Kim et al. [37] compared to the plot using parameters determined by Kim et al. using a finite element model of the biaxial test.

C Parameter Fitting for the Windkessel Model

Pulse-duplicator system components upstream of the aortic test section, including the resistance and compliance of the pump, the viscoelastic impedance adapter (VIA) subsystem, and the left ventricular chamber of the pulse duplicator, are described by a three-element Windkessel (R-C-R) model for the porcine aortic valve, whereas a more detailed model is used for the bovine pericardial valve because additional experimental data are available for the bovine pericardial BHV cases. See Figure 3 of the main text. We remark that the VIA subsystem includes tunable compliance chambers (see Figure 1b of the main text) that help to ameliorate unphysiological pressure oscillations in the left ventricular pressure [38]. The upstream model used in the porcine aortic valve simulations is

$$C_{\mathrm{VIA}}\frac{\mathrm{d}P_{\mathrm{VIA}}}{\mathrm{d}t} = \frac{P_{\mathrm{pump}} - P_{\mathrm{VIA}}}{R_1} + Q_{\mathrm{LV}}, \tag{S4}$$

$$\frac{P_{\mathrm{LV}}}{R_2} = \frac{P_{\mathrm{VIA}}}{R_2} + Q_{\mathrm{LV}}, \tag{S5}$$

in which C_{VIA}, R_1, and R_2 characterize the VIA system, and Q_{LV} and P_{LV} are the volumetric flow rate and pressure, respectively, at the inlet of the aortic test section model. P_{pump} is derived from (S4) and (S5) using experimental measurements of Q_{LV} and P_{LV}. The upstream model used in the bovine pericardial valve simulations is

$$C_{\mathrm{VIA}_1}\frac{\mathrm{d}P_{\mathrm{VIA}_1}}{\mathrm{d}t} = Q_{\mathrm{pump}} - \frac{P_{\mathrm{VIA}_1} - P_{\mathrm{VIA}_2}}{R_{\mathrm{VIA}}}, \tag{S6}$$

$$C_{\mathrm{VIA}_2}\frac{\mathrm{d}P_{\mathrm{VIA}_2}}{\mathrm{d}t} = \frac{P_{\mathrm{VIA}_1} - P_{\mathrm{VIA}_2}}{R_{\mathrm{VIA}}} - \frac{P_{\mathrm{VIA}_2} - P_{\mathrm{LA}} + Q_{\mathrm{LV}}R_{\mathrm{MV}}}{R_{\mathrm{out}} + R_{\mathrm{MV}}}, \tag{S7}$$

$$P_{\mathrm{LV}} = \frac{P_{\mathrm{VIA}_2}R_{\mathrm{MV}} + P_{\mathrm{LA}}R_{\mathrm{out}} - Q_{\mathrm{LV}}R_{\mathrm{out}}R_{\mathrm{MV}}}{R_{\mathrm{out}} + R_{\mathrm{MV}}}, \tag{S8}$$

in which C_{VIA_1}, C_{VIA_2}, R_{VIA}, and R_{out} characterize the VIA system, R_{MV} characterizes the resistance at the mitral position, P_{LA} is the left atrial pressure, Q_{pump} is the prescribed volumetric flow rate of the pump, and Q_{LV} and P_{LV} are the volumetric flow rate and pressure, respectively, at the inlet of the aortic test section model.

The downstream loading conditions of the pulse duplicator are also described by a three-element Windkessel model,

$$C\frac{\mathrm{d}P_{\mathrm{Wk}}}{\mathrm{d}t} = Q_{\mathrm{Ao}} - \frac{P_{\mathrm{Wk}}}{R_{\mathrm{p}}}, \tag{S9}$$

$$P_{\mathrm{Ao}} = P_{\mathrm{Wk}} + Q_{\mathrm{Ao}}R_{\mathrm{c}}, \tag{S10}$$

in which C is the compliance, R_{c} is the characteristic resistance, R_{p} is the peripheral resistance, P_{Wk} is the Windkessel pressure, and Q_{Ao} and P_{Ao} are the volumetric flow rate and pressure, respectively, at the outlet of the test section. The Windkessel parameters R_{c}, R_{p}, and C are calibrated using experimental measurements of Q_{Ao} and P_{Ao}. We use the nonlinear optimization tool fmincon in MATLAB to determine the model parameters by comparing P_{Ao} from (S9) and (S10) with that of experimental system (Figure S2). When calibrating the reduced-order models, the experimental measurements of Q_{Ao} are used as inputs to the Windkessel models.

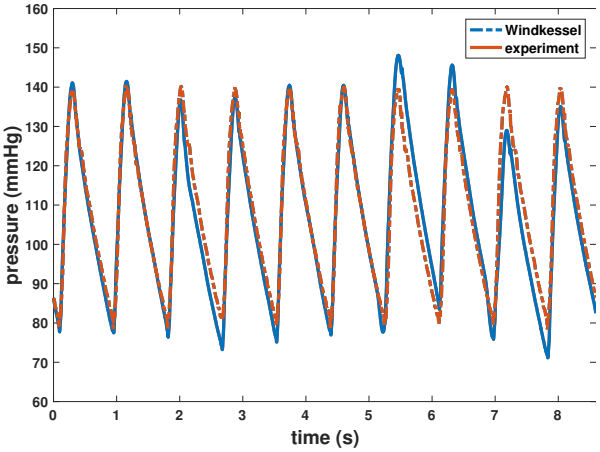

(a) Porcine aortic valve (downstream)

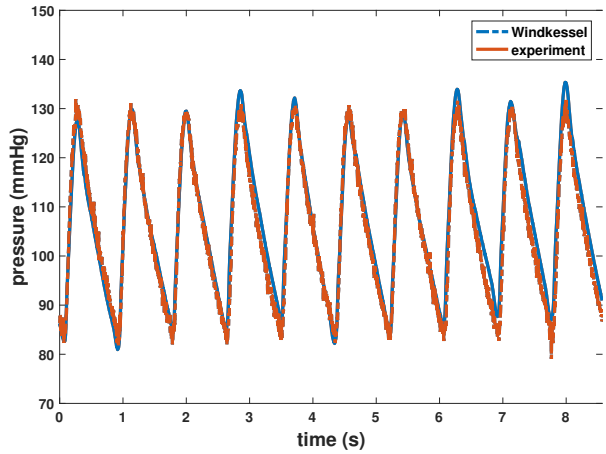

(b) Bovine pericardial valve (downstream)

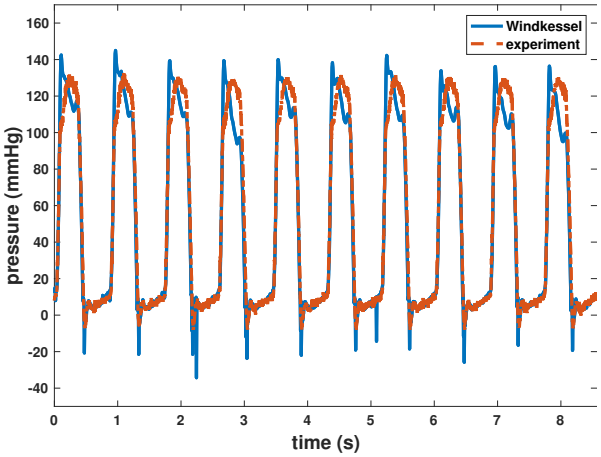

(c) Bovine pericardial valve (upstream)

Figure S2: (a)-(b) The three-element Windkessel model fits of the experimental downstream pressure (pressure at the outlet) data for both porcine aortic valve and bovine pericardial valve models (Figures 3a and 3b). These fits are obtained using a nonlinear optimization tool fmincon in MATLAB by comparing experimental values of P_{Ao} to model results obtained by solving (S9) and (S10) with measured values of Q_{Ao} as inputs to the Windkessel models. (c) Model fit of the experimental upstream pressure (pressure at the inlet) data for the bovine pericardial valve model using a detailed upstream model shown in Figure 3b. These fits are obtained by comparing experimental values of P_{LV} to model results obtained by solving (S6), (S7), and (S8) with measured values of Q_{pump}, Q_{LV}, and P_{LA}.

A first-order (Godunov) time step splitting is used to couple the three-dimensional FSI model to the reduced-order models, as described by Griffith et al. [16]. At the outlet of the aortic test section, for example, the mean flow rate through the outlet surface computed by the three-dimensional FSI model is provided as an input to the Windkessel model. The pressure generated in the Windkessel model is used, along with the flow rate, to determine the pressure along the outlet surface, which is used as a boundary condition for the three-dimensional model.

D Immersed Boundary Formulation

D.1 Continuum Equations

The IB formulation uses an Eulerian description of the momentum, viscosity, and incompressibility of the coupled fluid-structure system, and it uses a Lagrangian description of the deformations, stresses, and resul-

tant forces of the immersed structure. In particular, we model the immersed structure as a viscoelastic solid, in which the viscous stresses in the solid are small compared to elastic stresses, as in previous work by us and others [49,76–80]. The coupling between Eulerian and Lagrangian variables is mediated by integral transforms with delta function kernels. In the continuous IB formulation, we consider a fixed three-dimensional Eulerian computational domain Ω that is divided into the time-dependent solid (Ω_t^{s}) and fluid (Ω_t^{f}) subdomains, so that $\Omega = \Omega_t^{\mathrm{s}} \cup \Omega_t^{\mathrm{f}}$. Here, $\boldsymbol{x} = (x_1, x_2, x_3) \in \Omega$ are physical coordinates, $\boldsymbol{X} = (X_1, X_2, X_3) \in \Omega_0^{\mathrm{s}}$ are reference coordinates attached to the structure, $\boldsymbol{N}(\boldsymbol{X}) \in \partial\Omega_0^{\mathrm{s}}$ is the outward unit normal to the reference configuration of the solid region at material point $\boldsymbol{X}$, and $\boldsymbol{\chi}(\boldsymbol{X}, t) \in \Omega_t^{\mathrm{s}}$ is the physical position of material point $\boldsymbol{X}$ at time t. ρ and μ are the mass density and viscosity, $\boldsymbol{u}(\boldsymbol{x}, t)$ and $p(\boldsymbol{x}, t)$ are the Eulerian velocity and pressure fields, $\boldsymbol{f}(\boldsymbol{x}, t)$ is the Eulerian elastic force density, $\mathbb{P}(\boldsymbol{X}, t)$ is the first Piola-Kirchhoff elastic stress of the immersed structure, and $\delta(\boldsymbol{x}) = \prod_{i=1}^{3} \delta(x_i)$ is the three-dimensional Dirac delta function. The IB form of the equations of motion for the fluid-structure system is:

$$\rho \frac{\mathrm{D}\boldsymbol{u}}{\mathrm{D}t}(\boldsymbol{x}, t) = -\nabla p(\boldsymbol{x}, t) + \mu \nabla^2 \boldsymbol{u}(\boldsymbol{x}, t) + \boldsymbol{f}(\boldsymbol{x}, t), \tag{S11}$$

$$\nabla \cdot \boldsymbol{u}(\boldsymbol{x}, t) = 0, \tag{S12}$$

$$\begin{aligned} \boldsymbol{f}(\boldsymbol{x}, t) = &\int_{\Omega_0^s} \nabla_{\boldsymbol{X}} \cdot \mathbb{P}(\boldsymbol{X}, t)\, \delta(\boldsymbol{x} - \boldsymbol{\chi}(\boldsymbol{X}, t))\, \mathrm{d}\boldsymbol{X} \\ &- \int_{\partial\Omega_0^s} \mathbb{P}(\boldsymbol{X}, t)\, \boldsymbol{N}(\boldsymbol{X})\, \delta(\boldsymbol{x} - \boldsymbol{\chi}(\boldsymbol{X}, t))\, \mathrm{d}A, \end{aligned} \tag{S13}$$

$$\frac{\partial \boldsymbol{\chi}}{\partial t}(\boldsymbol{X}, t) = \int_{\Omega} \boldsymbol{u}(\boldsymbol{x}, t)\, \delta(\boldsymbol{x} - \boldsymbol{\chi}(\boldsymbol{X}, t))\, \mathrm{d}\boldsymbol{x} = \boldsymbol{u}(\boldsymbol{\chi}(\boldsymbol{X}, t), t), \tag{S14}$$

in which $\frac{\mathrm{D}}{\mathrm{D}t} = \frac{\partial}{\partial t} + \boldsymbol{u} \cdot \nabla$ is the material derivative. Notice that because $\partial\boldsymbol{\chi}/\partial t(\boldsymbol{X}, t) = \boldsymbol{u}(\boldsymbol{\chi}(\boldsymbol{X}, t), t)$ and $\nabla \cdot \boldsymbol{u}(\boldsymbol{x}, t) = 0$, the immersed structure is described in the continuous IB framework as an exactly incompressible material.

D.2 Numerical Approximations

The computational domain Ω, which includes both the solid and fluid subregions, is described using a block-structured locally refined Cartesian grid consisting of multiple nested levels of Cartesian grid patches. High spatial resolution is used dynamically near fluid-structure interfaces (Figure S3) and near flow features, such as vortices shed from the valve leaflets, that are identified by feature detection criteria that select regions of high vorticity for enhanced spatial resolution. A staggered-grid discretization is used for the incompressible Navier-Stokes that includes a version [81,82] of the xsPPM7 variant [59] of the piecewise parabolic method (PPM) [58] to approximate the convective term.

In our simulations, we use a regularized delta function $\delta_h(\boldsymbol{x})$ to approximate the singular Dirac delta function $\delta(\boldsymbol{x})$. The three-dimensional regularized delta function is the tensor product of one-dimensional delta functions, $\delta_h(\boldsymbol{x}) = \prod_{i=1}^{3} \delta_h(x_i)$, and the one-dimensional delta function is defined in terms of a basic kernel function via $\delta_h(x) = \frac{1}{h}\varphi\left(\frac{x}{h}\right)$. In our computations, different regularized delta functions are used for the rigid aortic test section and flexible valve leaflets. These choices are based on preliminary benchmarking studies extending the tests reported by Griffith and Luo [49]. For the aortic test section, we use a simple piecewise-linear (PWL) kernel that takes the form,

$$\varphi^{\mathrm{PWL}}(r) = \begin{cases} 1 - r, & 0 \le r < 1, \\ 0, & 1 \le r, \end{cases} \tag{S15}$$

and we use a three-point B-spline (BS3) kernel for the valve leaflets,

$$\varphi^{\mathrm{BS3}}(r) = \begin{cases} \frac{3}{4} - r^2, & 0 \le r < 0.5, \\ \frac{9}{8} - \frac{3}{2}r + \frac{1}{2}r^2, & 0.5 \le r \le 1.5, \\ 0, & 1.5 \le r. \end{cases} \tag{S16}$$

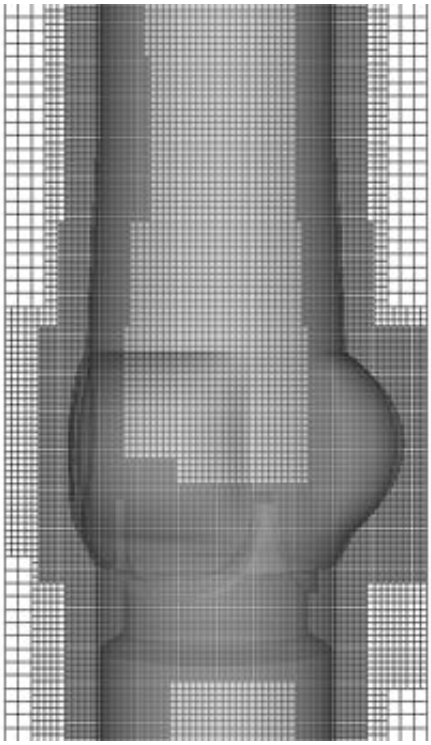

Figure S3: The aortic test section in the computational domain. The computational domain is a block-structured adaptively refined Cartesian grid. A snapshot of the locally refined grid is shown on a plane that bisects the aortic test section.

Notice that the gap between the valve leaflets during closure reflects the size of regularized delta function, and in our simulations, the valve is effectively closed during the diastolic phase of the simulated cardiac cycle. This is also shown by Figures 4b and 4d in the main text, in which there is no leakage once the valve is closed. An advantage of the IB formulation of such problems is that it does not require an explicit contact model to simulate contact between the valve leaflets.

E Stabilization Method for the Hyperelastic Immersed Boundary Method

In the continuum equations of the IB framework (Supplemental Materials Section D.1), the Cauchy stress on the full domain can be seen to take the form

$$\sigma(\boldsymbol{x},t) = \sigma^{\mathrm{f}} + \begin{cases} \mathbb{0}, & \boldsymbol{x} \in \Omega_t^{\mathrm{f}}, \\ \sigma^{\mathrm{e}}, & \boldsymbol{x} \in \Omega_t^{\mathrm{s}}, \end{cases} \tag{S17}$$

which can also be written as

$$\sigma(\boldsymbol{x},t) = \mathrm{dev}[\sigma^{\mathrm{v}}] - p\mathbb{I} + \begin{cases} \mathbb{0}, & \boldsymbol{x} \in \Omega_t^{\mathrm{f}}, \\ \sigma^{\mathrm{e}}, & \boldsymbol{x} \in \Omega_t^{\mathrm{s}}, \end{cases} \tag{S18}$$

in which $\sigma^{\mathrm{e}} = \frac{1}{J}\mathbb{P}\mathbb{F}^T$, $\sigma^{\mathrm{v}} = \mu(\nabla \boldsymbol{u} + \nabla \boldsymbol{u}^T)$ is the viscous stress, the pressure p is a Lagrange multiplier that imposes the incompressibility constraint for both the fluid and structure, and $\mathrm{dev}[\sigma^{\mathrm{v}}]$ is the deviatoric part of σ^{v} that is defined as

$$\mathrm{dev}[\sigma^{\mathrm{v}}] = \sigma^{\mathrm{v}} - \frac{\mathrm{tr}(\sigma^{\mathrm{v}})}{3}\mathbb{I}. \tag{S19}$$

Although the continuous IB equations model the structure as exactly incompressible, the present numerical method is not guaranteed to preserve the divergence of the Eulerian velocity field when that field is evaluated

on the Lagrangian finite element mesh. Consequently, the method only approximately accounts for the incompressibility of the immersed structure, although the accuracy of this approximation improves under grid refinement. Vadala-Roth et al. [45] introduced a volumetric energy in the solid region to stabilize and improve the accuracy of the numerical scheme substantially,

$$\sigma(\boldsymbol{x},t) = \operatorname{dev}[\sigma^{\mathrm{v}}] - p\mathbb{I} + \begin{cases} \mathbb{0}, & \boldsymbol{x} \in \Omega_t^{\mathrm{f}}, \\ \operatorname{dev}[\sigma^{\mathrm{e}}] - p_{\mathrm{stab}}\mathbb{I}, & \boldsymbol{x} \in \Omega_t^{\mathrm{s}}, \end{cases} \tag{S20}$$

in which the stabilization term $p_{\mathrm{stab}} = -\partial U(J)/\partial J$ acts as a pressure that reinforces incompressibility in the solid region in the numerical method. We refer to this as a stabilization method because its effect vanishes under grid refinement. Specifically, in the continuum limit, the structure is automatically incompressible in the IB framework, and so $J \equiv 1$ and $p_{\mathrm{stab}} \equiv 0$. This stabilization method has been tested using standard quasi-static solid mechanics benchmark problems. Sections E.1 and E.2 show two benchmark examples from Vadala-Roth et al. [45] that demonstrate the effect of this stabilization method. These results are compared to and show excellent agreement with the results from a stabilized incompressible finite element solid mechanics formulation. Additional details are provided by Vadala-Roth et al. [45].

E.1 Compression Benchmark

This benchmark involves a rectangular block with a downward traction of 200 dyn cm^{-2} applied at the center of the top side along with zero horizontal displacement. Zero vertical displacement is imposed at the bottom side of the block, and zero traction is applied at all sides other than the top side [83], as shown in Figure S4a. The block is a neo-Hookean material,

$$\Psi = \frac{c_1}{2}(\bar{I}_1 - 3) + \frac{\kappa_{\mathrm{stab}}}{2}(\ln J)^2, \tag{S21}$$

in which $\bar{I}_1 = \operatorname{tr}(\overline{\mathbb{C}})$ is the first invariant of the modified right Cauchy-Green strain tensor $\overline{\mathbb{C}} = \overline{\mathbb{F}}^T\overline{\mathbb{F}} = J^{-2/3}\mathbb{F}^T\mathbb{F}$. Here, c_1 is the shear modulus, and κ_{stab} is the numerical bulk modulus controlled by the shear modulus and the numerical Poisson ratio, ν_{stab}, via

$$\kappa_{\mathrm{stab}} = \frac{2\mu_{\mathrm{s}}(1+\nu_{\mathrm{stab}})}{3(1-2\nu_{\mathrm{stab}})}, \tag{S22}$$

in which μ_{s} is the linearized ($\mathbb{F} = \mathbb{I}$) shear modulus. For the neo-Hookean model, $\mu_{\mathrm{s}} = c_1$. This test uses $c_1 = 80.194$ dyn cm^{-2} and $\nu_{\mathrm{stab}} = 0.4$. The density and viscosity are $\rho = 1.0$ g cm^{-3} and $\mu = 0.01$ dyn s cm^{-2}, respectively. We again emphasize that the numerical bulk modulus, κ_{stab}, and the numerical Poisson ratio, ν_{stab}, act as stabilization parameters, and not as physical parameters of the model, and that their effects vanish under grid refinement. This test shows that using the stabilization method yields superior volume conservation and smooth deformations for the mesh elements (Figures S4b and S4d).

E.2 Torsion Benchmark

This benchmark involves applying torsion to an elastic beam [84] as shown in Figure S5a. Torsion is applied to the top face of the beam while zero displacement is imposed at the opposite face. Zero traction boundary conditions were used on all the other faces. The elastic beam is a Mooney-Rivlin material,

$$\Psi = c_1(\bar{I}_1 - 3) + c_2(\bar{I}_2 - 3) + \frac{\kappa_{\mathrm{stab}}}{2}(\ln J)^2, \tag{S23}$$

in which $\bar{I}_2 = (\bar{I}_1^2 - \operatorname{tr}(\overline{\mathbb{C}}^2))/2$ is the second invariant of $\overline{\mathbb{C}}$. For the Mooney-Rivlin model, $\mu_{\mathrm{s}} = 2(c_1 + c_2)$. This test uses material parameters $c_1 = 9000$ dyn cm^{-2}, $c_2 = 9000$ dyn cm^{-2}, and $\nu_{\mathrm{stab}} = 0.4$. The density and viscosity are $\rho = 1.0$ g cm^{-3} and $\mu = 0.04$ dyn s cm^{-2}, respectively. This test also shows that the stabilization method gives reasonable deformation (Figure S5c) as well as yielding superior volume conservation (Figures S5b and S5d).

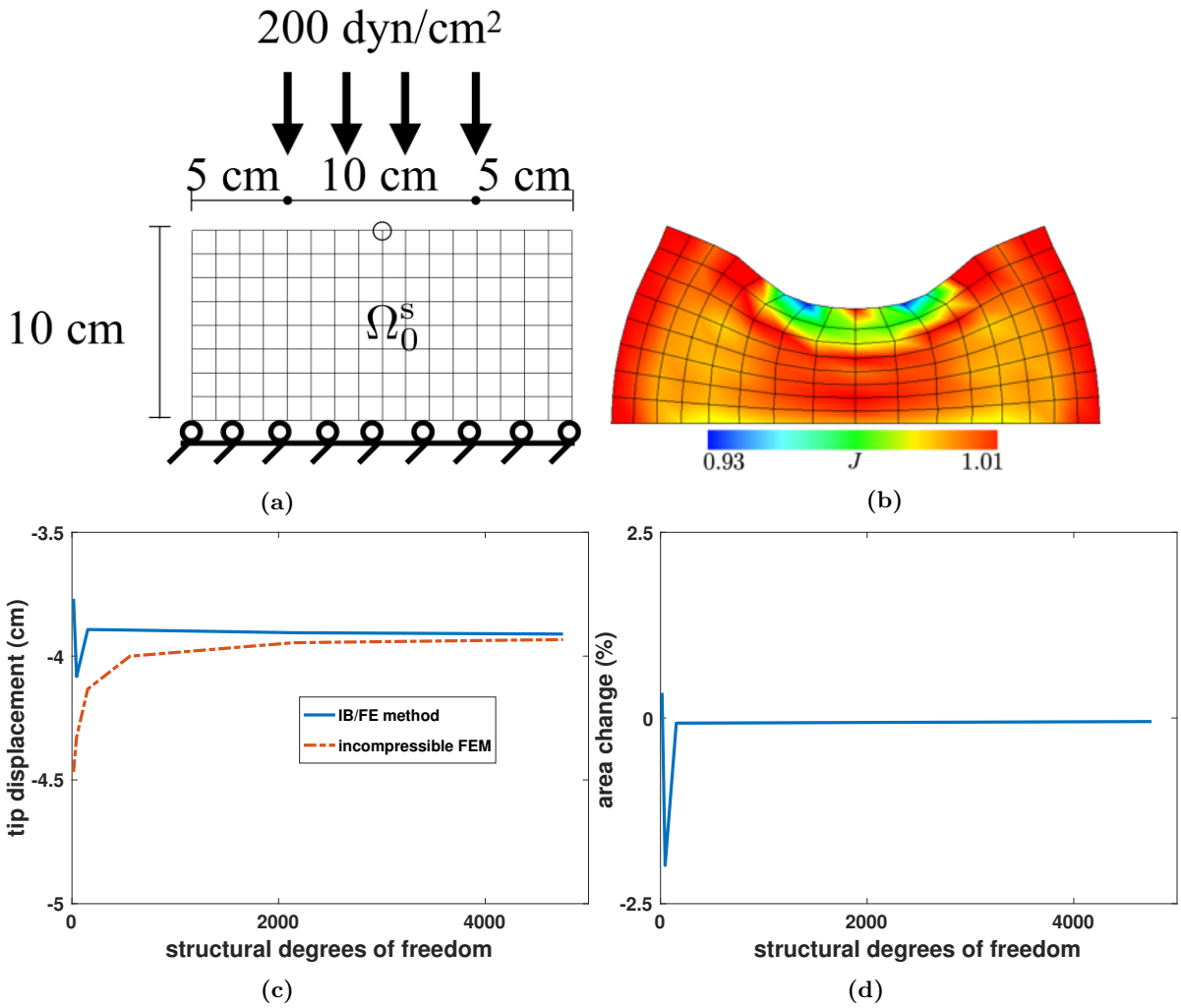

Figure S4: (a) Schematic of the compressed block benchmark from Vadala-Roth et al. [45]. A downward traction applied at the center of the top side along with zero horizontal displacement. Zero vertical displacement is imposed at the bottom side of the block, and zero traction is applied at all sides other than the top side, as used by Reese et al. [83]. (b) Deformation of the compressed block for a neo-Hookean material model. The stabilization method results in smooth element deformation as well as excellent volume (area) conservation. The color shows the magnitude of $J = \det(\mathbb{F})$. (c) Displacement of the circled location in panel a compared to result from using standard incompressible structural mechanics formulation. (d) Percent change in total area; see also panel (b).

F Solution Verification

We perform grid convergence studies to verify the level of consistency in our numerical results. We consider both dynamic and steady flow conditions at three different spatial resolutions. For the dynamic cases, we consider the consistency under grid refinement of all of the measurements reported in the manuscript. For the steady flow conditions, we observe the time-averaged flow rates and the turbulence kinetic energy (TKE) between different resolutions, in addition to bulk measurements.

We use locally refined Cartesian grids with an effective fine-grid resolution that corresponds to a uniform $N \times N \times N$ grid, and we compare results obtained for $N = 192$, 256, and 320. The effective fine-grid Cartesian resolutions are approximately 0.53 mm ($N = 192$), 0.39 mm ($N = 256$), and 0.32 mm ($N = 320$). The average grid-spacings of meshes are 0.5 mm ($N = 192$), 0.4 mm ($N = 256$), and 0.3 mm ($N = 320$) for

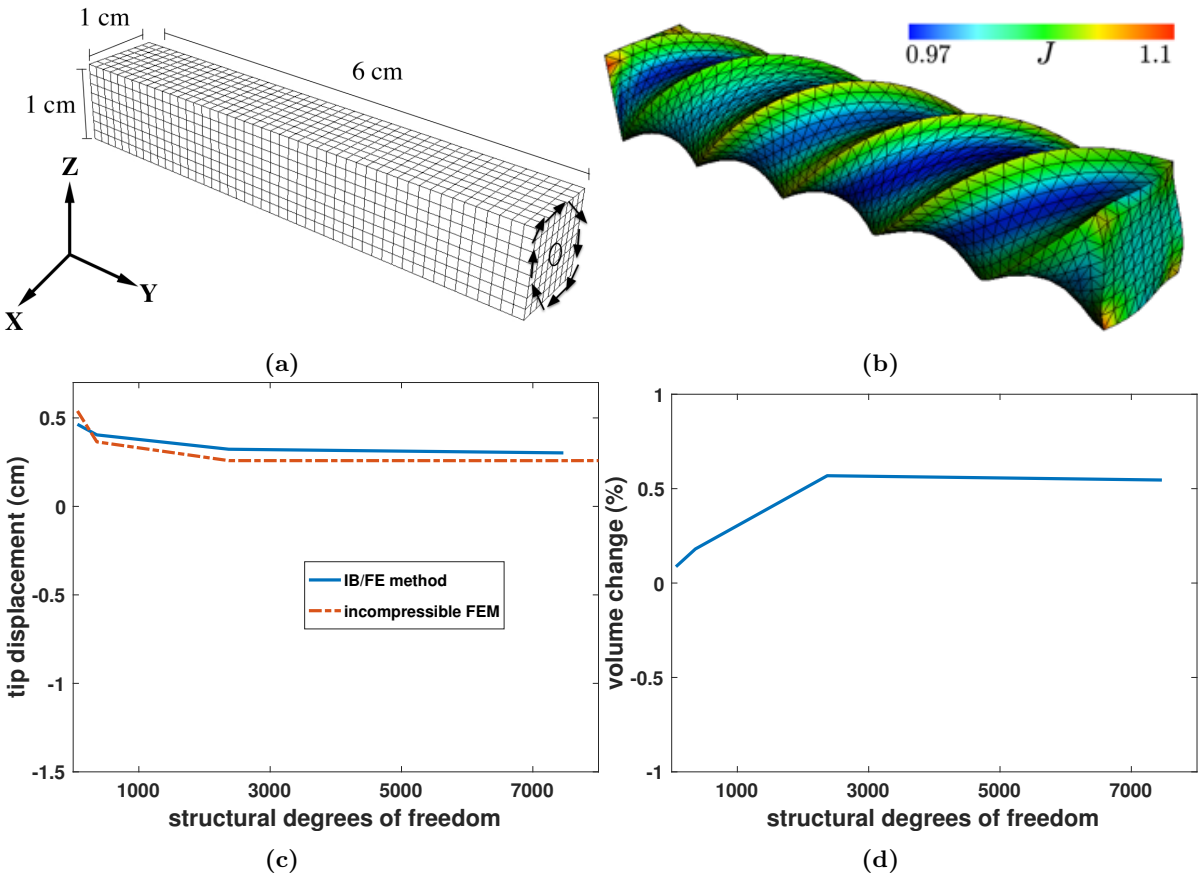

Figure S5: (a) Schematic of the torsion benchmark from Vadala-Roth et al. [45]. A Mooney-Rivlin material model is used, and torsion is applied to the top face of the beam while zero displacement is imposed at the opposite face. Zero traction boundary conditions were used on all the other faces, as in Bonet et al. [84]. (b) Deformation of the torsion test for a Mooney-Rivlin material model. The stabilization method results in smooth element deformation as well as excellent volume conservation. The color shows the magnitude of $J = \det(\mathbb{F})$. (c) Displacement of the tip position (the circled location in panel a) on the beam in the axial (Y) direction compared to result from using standard incompressible structural mechanics formulation. (d) Percent change in total volume; see also panel (b).

the aortic test section, 0.75 mm ($N = 192$), 0.59 mm ($N = 256$), and 0.45 mm ($N = 320$) for the porcine aortic valve, and 0.75 mm ($N = 192$, 256, and 320) with a wider range of grid-spacings for the bovine pericardial valve.

Figure S6 compares the bulk flow properties under grid refinement, indicating that our simulations are consistent under grid refinement. This suggests that the results reported in the main text are sufficiently resolved for these measurements by the resolutions considered therein. Tables S1, S2, S3, and S4 quantify the discrepancies relative to the experimental data under grid refinement, as well as the relative difference between resolutions ($N = 192$, $N = 256$, and $N = 320$). The relative differences are calculated by

$$\text{Normalized difference of } M^{N=192} \text{ and } M^{N=256} = \frac{\left\| M^{N=192} - M^{N=256} \right\|_{L^q(0,T)}}{\| M^{N=256} \|_{L^q(0,T)}}, \tag{S24}$$

$$\text{Normalized difference of } M^{N=256} \text{ and } M^{N=320} = \frac{\left\| M^{N=256} - M^{N=320} \right\|_{L^q(0,T)}}{\| M^{N=320} \|_{L^q(0,T)}}, \tag{S25}$$

in which $(0, T)$ indicates an integral over time, and $q = 2$ or ∞ for the L^2- and L^∞-norms, respectively. This shows that the discrepancies in bulk flow measurements compared to the experimental data are within

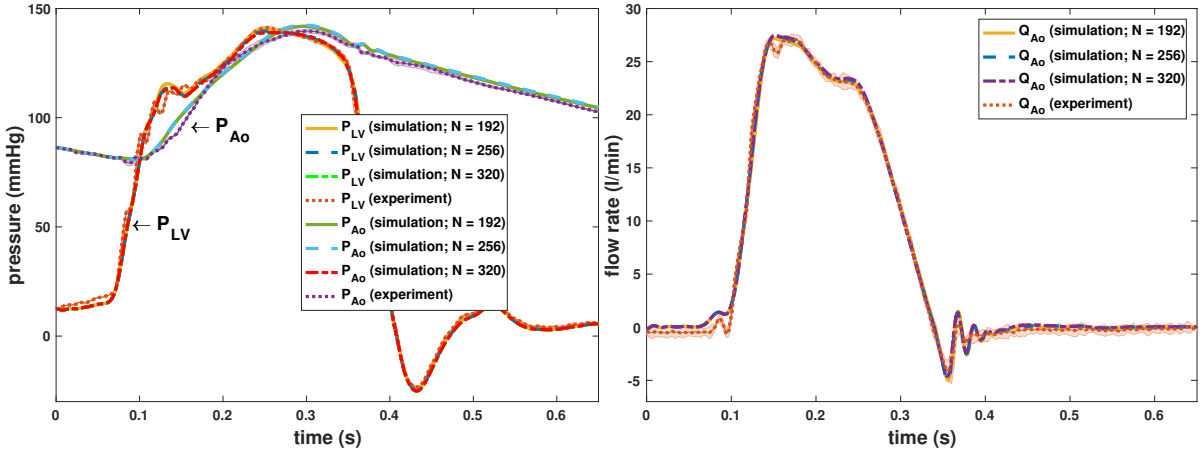

(a) Porcine aortic valve **(b)** Porcine aortic valve

(c) Bovine pericardial valve **(d)** Bovine pericardial valve

Figure S6: Grid refinement test corresponding to Figure 4 of the main text. The bulk flow waveforms are consistent under grid refinement.

8.7% at all resolutions. The relative differences between successive resolutions are within 1.6%, indicating consistency under grid refinement. This suggests that the bulk properties are reasonably resolved by our FSI model of the BHVs at the higher spatial resolutions ($N = 256$ and $N = 320$).

Table S1: Comparisons of normalized L^2-norms of discrepancies in the bulk measurements between simulation and experiment*

	Porcine aortic			Bovine pericardial		
	$N = 192$	$N = 256$	Relative	$N = 192$	$N = 256$	Relative
P_{LV}	3.6%	3.4%	0.73%	5.2%	4.6%	1.1%
P_{Ao}	1.7%	1.9%	0.33%	1.4%	1.4%	0.09%
Q_{Ao}	5.0%	4.7%	1.6%	8.4%	8.6%	0.71%

* Comparisons of L^2-norms of the discrepancies in the bulk measurements from the simulation and experiment shown in Figure S6 under the coarser ($N = 192$) and finer ($N = 256$) resolutions, normalized by the L^2-norms of the measurements from the experiment. Relative indicates the L^2-norms of the differences between the measurements from the two resolutions, normalized by the L^2-norms of the measurements from the finer ($N = 256$) case.

The comparison of PDVA results is similar to that of other bulk measurements under grid refinement, as

Table S2: Comparisons of normalized L^2-norms of discrepancies in the bulk measurements between simulation and experiment*

	Porcine aortic			Bovine pericardial		
	$N = 256$	$N = 320$	Relative	$N = 256$	$N = 320$	Relative
P_{LV}	3.4%	3.4%	0.45%	4.6%	4.5%	0.67%
P_{Ao}	1.9%	1.9%	0.21%	1.4%	1.4%	0.004%
Q_{Ao}	4.7%	4.8%	0.74%	8.6%	8.7%	0.43%

* Comparisons of L^2-norms of the discrepancies in the bulk measurements from the simulation and experiment shown in Figure S6 under the finer ($N = 256$) and finest ($N = 320$) resolutions, normalized by the L^2-norms of the measurements from the experiment. Relative indicates the L^2-norms of the differences between the measurements from the two resolutions, normalized by the L^2-norms of the measurements from the finer ($N = 320$) case.

Table S3: Comparisons of normalized L^∞-norms of discrepancies in the bulk measurements between simulation and experiment*

	Porcine aortic			Bovine pericardial		
	$N = 192$	$N = 256$	Relative	$N = 192$	$N = 256$	Relative
P_{LV}	8.5%	8.6%	1.6%	15.6%	14.4%	1.7%
P_{Ao}	4.3%	4.5%	0.42%	3.5%	3.6%	0.17%
Q_{Ao}	11.6%	9.5%	2.4%	19.2%	20.2%	1.4%

* Comparisons of L^∞-norms of the discrepancies in the bulk measurements from the simulation and experiment shown in Figure S6 between the coarser ($N = 192$) and finer ($N = 256$) resolutions, normalized by the L^∞-norms of the measurements from the experiment. Relative indicates the L^∞-norms of the differences between the measurements from the two resolutions, normalized by the L^∞-norms of the measurements from the finer ($N = 256$) case.

Table S4: Comparisons of normalized L^∞-norms of discrepancies in the bulk measurements between simulation and experiment*

	Porcine aortic			Bovine pericardial		
	$N = 256$	$N = 320$	Relative	$N = 256$	$N = 320$	Relative
P_{LV}	8.6%	8.6%	1.5%	14.4%	14.1%	1.1%
P_{Ao}	4.5%	4.5%	0.31%	3.6%	3.6%	0.001%
Q_{Ao}	9.5%	9.2%	2.2%	20.2%	20.8%	0.6%

* Comparisons of L^∞-norms of the discrepancies in the bulk measurements from the simulation and experiment shown in Figure S6 between the finer ($N = 256$) and finest ($N = 320$) resolutions, normalized by the L^∞-norms of the measurements from the experiment. Relative indicates the L^∞-norms of the differences between the measurements from the two resolutions, normalized by the L^∞-norms of the measurements from the finer ($N = 320$) case.

observed in Figure S6.

Figures S8 and S9 also give a qualitative sense of model consistency under grid refinement. Although Figures S8 and S9 indicate that additional small-scale flow features are generated by the model at higher spatial resolutions, the large scale flow features are consistent between grid resolutions.

We also observe that the time-averaged flow fields (Eq. S26) as well as the flow profiles (Figures S10 and S11) are in reasonable agreement between different spatial resolutions. The mean flow is determined via

$$\overline{u}_i = \frac{1}{T_2 - T_1} \int_{T_1}^{T_2} u_i(\boldsymbol{x}, t)\, \mathrm{d}t, \quad i = 1, 2, 3, \tag{S26}$$

We consider steady inflow conditions at two different flow rates: 100% and 50% of the maximum flow rate from the fully dynamic simulations. In particular, we find that the difference between $N = 256$ and $N = 320$

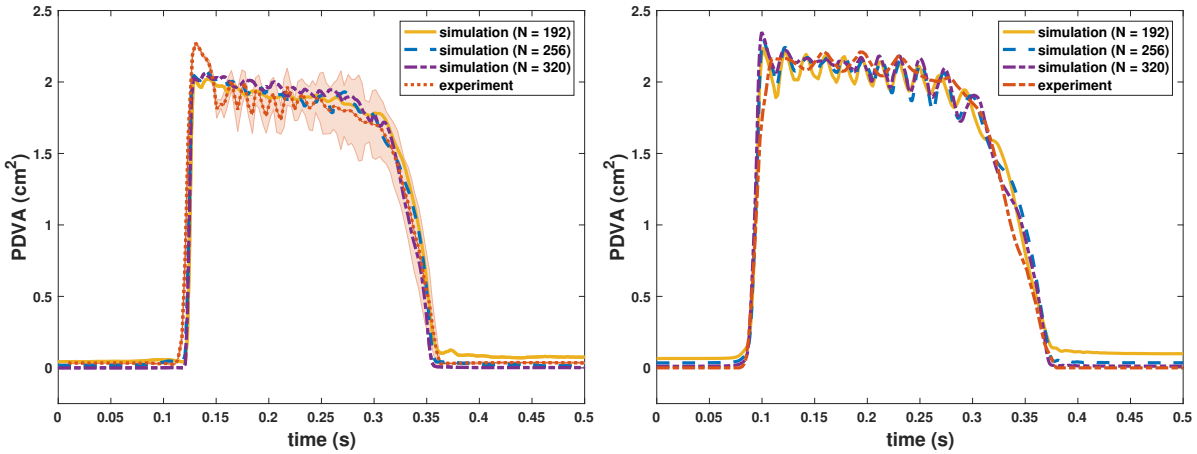

(a) Porcine aortic valve **(b)** Bovine pericardial valve

Figure S7: Grid refinement test corresponding to Figure 5 of the main text. The PDVA results are consistent under grid refinement. This result is in agreement with the consistency under grid refinement demonstrated in Figure S6d.

cases are small, and we conclude that $N = 256$ results are reasonably well resolved for large-scale flow measures.

We observe that the turbulence kinetic energy (Eq. S27) as well as its profiles for each bovine pericardial valve case (Figures S12 and S13) still show some differences between different spatial resolutions. Turbulence kinetic energy is defined by

$$TKE \equiv \frac{1}{2}\overline{u_i' u_i'}, \tag{S27}$$

in which $u_i' = u_i - \overline{u}_i$ is the fluctuating velocity. We again consider steady inflow conditions at two different flow rates: 100% and 50% of the maximum flow rate. At the maximum flow rate, the axial flow fields agree to approximately 1.6% in the L^2 norm for $N = 256$ and $N = 320$, with peak velocities differing by approximately 7%. At 50% of maximum flow, the flow fields agree to within approximately 1.1% in the L^2 norm, with peak velocities agreeing to within approximately 4%. The differences are larger for the TKE, with L^2 differences on the order of 10% and maximum TKE values differing by 17.5% at the maximum flow rate but to within approximately 1.5% at 50% of the maximum flow rate. The mean flow and TKE profiles are in reasonable agreement and appear to be converging under grid refinement. Although we find that the differences between $N = 256$ and $N = 320$ are not large, these results suggest that we are able to resolve the large-scale flow features, but higher spatial resolution is clearly needed to fully resolve the flow fields.

With steady inflow conditions, as in the pulsatile cases, the computed values of PDVA yielded by the model are in good agreement at the different grid spacings (data not shown). It is apparent, however, that the peak flow velocities for the coarser cases are larger than those of the finer cases. The observed differences in the peak flow velocities are a consequence of the numerical scheme that is used to couple the Lagrangian and Eulerian variables in the present IB method. Specifically, the use of regularized delta functions in the Lagrangian-Eulerian coupling operators causes the "effective" sizes of the Lagrangian structures to be larger than their "actual" sizes, with a length scale that is related to the regularization width of the delta function. In practice, the width of the regularized delta function is tied to the Cartesian grid spacing. This results in an effective narrowing of the flow path that is on the order of a few Cartesian grid cell widths, which is more pronounced on coarser grids. The effect of this narrowing is apparent in Figures S10 and S11 and results in higher flow velocities at the same volumetric flow rates. This effect also diminishes under grid refinement, as observed in the grid convergence study.

Figures S14 and S15 qualitatively compare the leaflet kinematics for $N = 192$, $N = 256$, and $N = 320$ during valve opening and closure for the porcine aortic valve and bovine pericardial valve, respectively. These results indicate that the computed structural deformations are consistent under grid refinement.

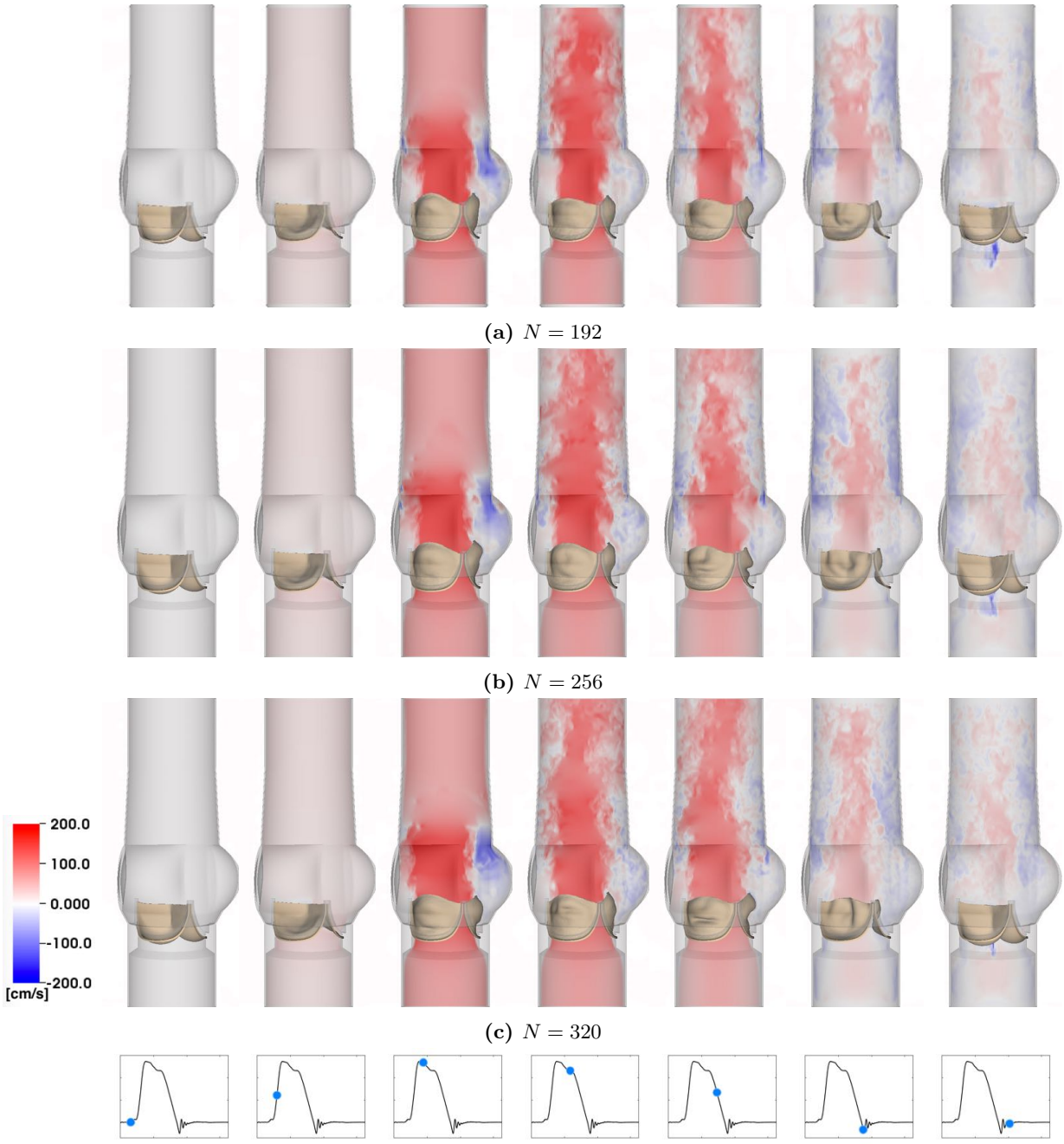

(a) $N = 192$

(b) $N = 256$

(c) $N = 320$

Figure S8: Grid refinement test corresponding to Figure 7a of the main text. Although additional small-scale flow features are generated by the model at higher spatial resolutions, the large scale flow features are consistent between grid resolutions.

Comparing the stress distributions of the leaflets in two grid resolutions (Figures S16 and S17) also confirms that the stress distributions are consistent under grid refinement.

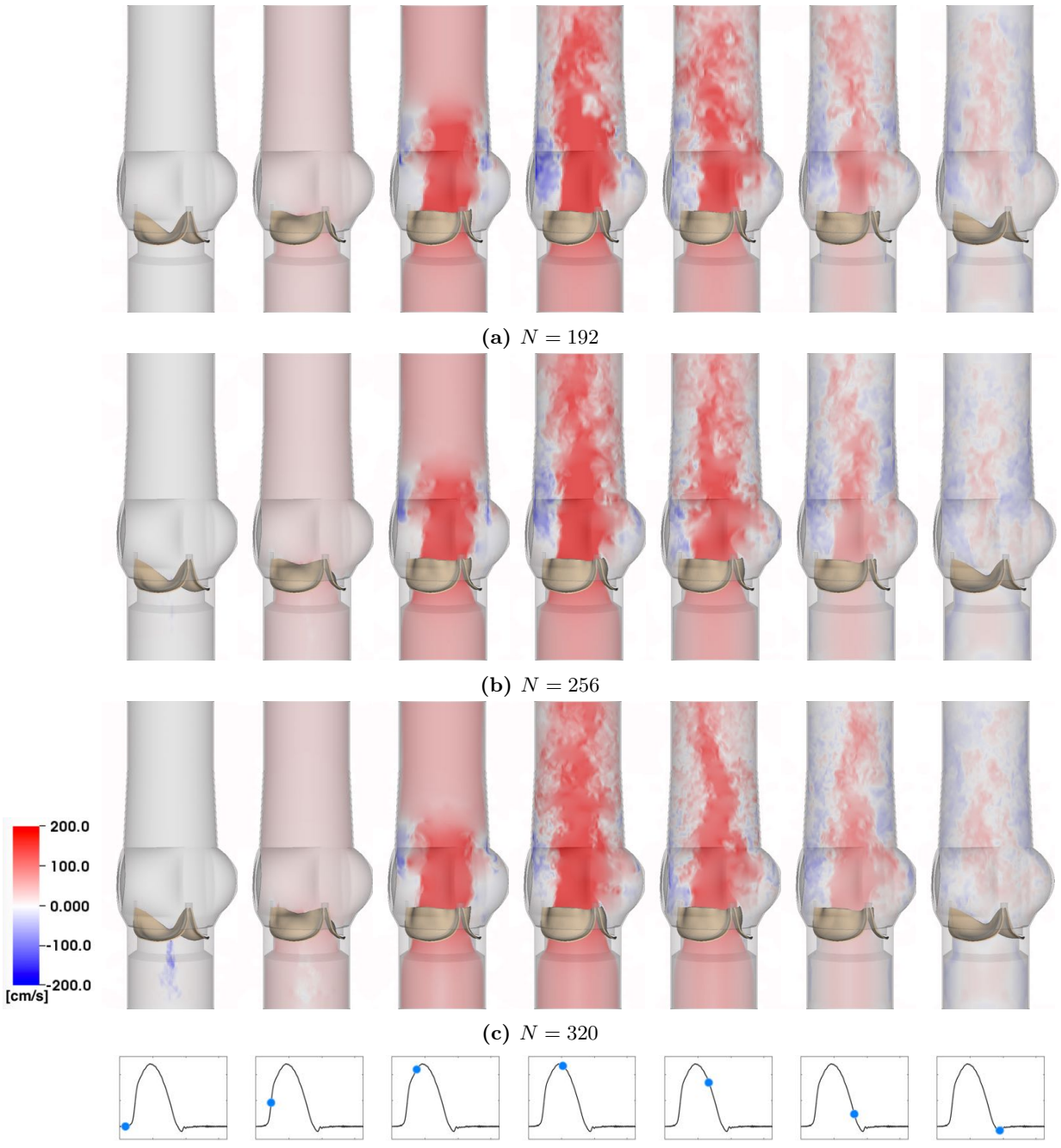

(a) $N = 192$

(b) $N = 256$

(c) $N = 320$

Figure S9: Grid refinement test corresponding to Figure 7b of the main text. Although additional small-scale flow features are generated by the model at higher spatial resolutions, the large scale flow features are consistent between grid resolutions.

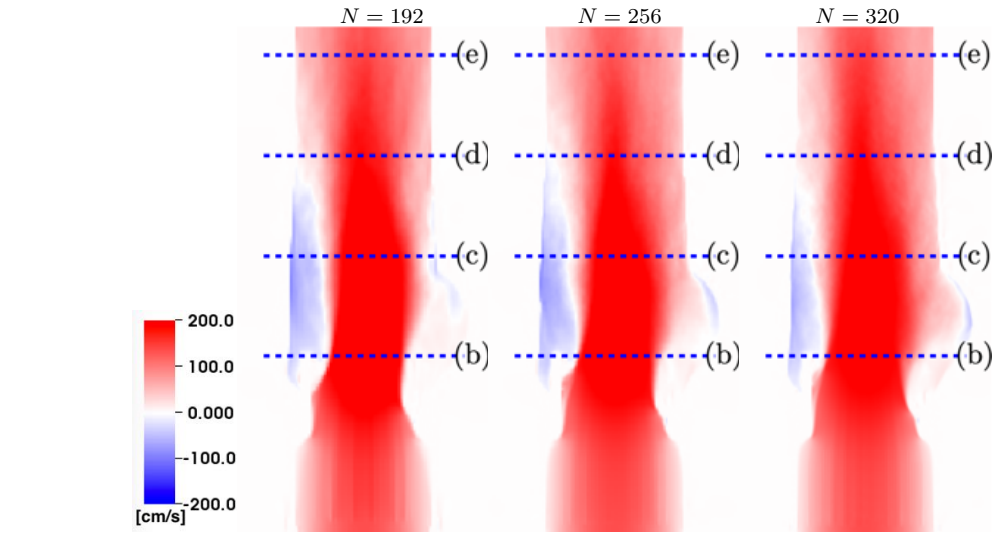

(a) Axial velocity (u_y) fields

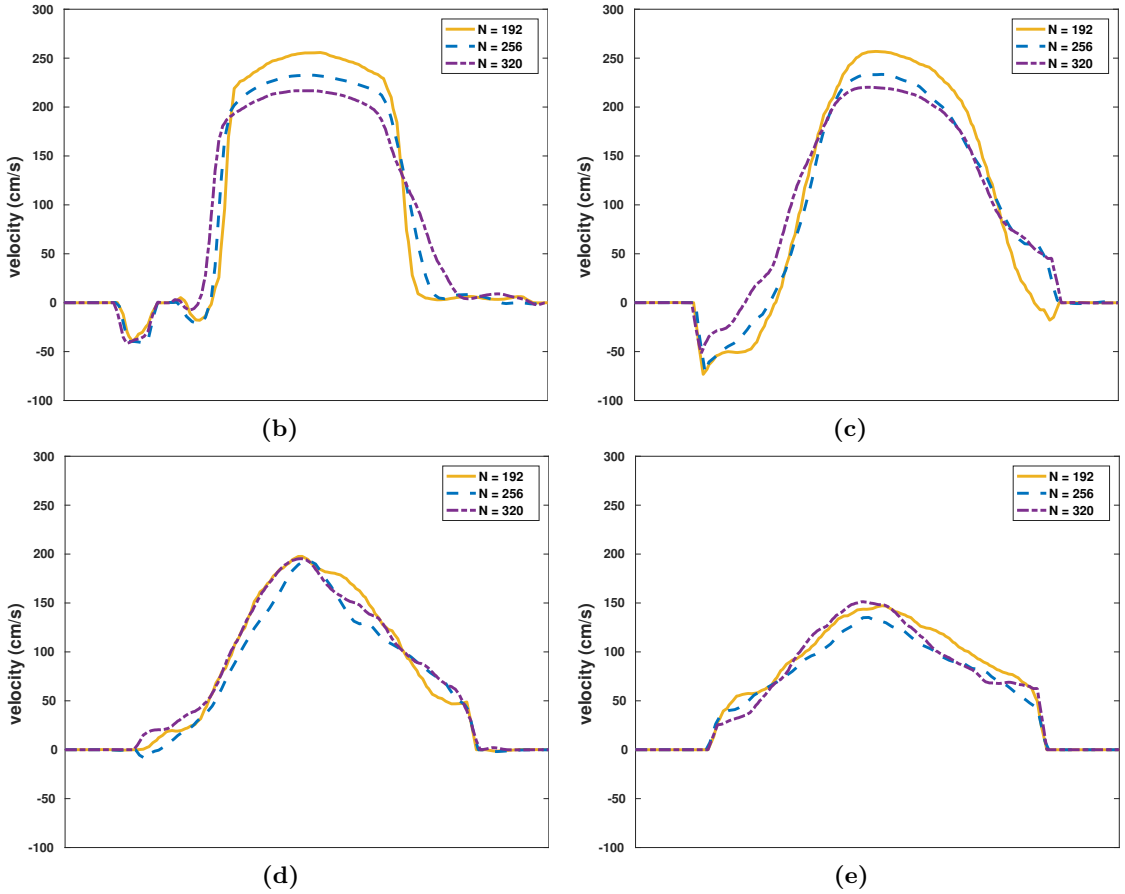

(b) **(c)**

(d) **(e)**

Figure S10: (a) Cross-section view of time-averaged flow fields and (b)-(e) flow profiles at different locations downstream of the valve for the bovine pericardial valve model. We use steady flow at the maximum flow rate. In panel (a), the color shows the time-averaged axial velocity through the aortic test section at the center plane, with red indicating forward flow and blue indicating reverse flow. Blue dashed lines show where the profiles shown in panels (b)-(e) are obtained. The axial flow fields agree to approximately 1.6% in the L^2 norm for $N = 256$ and $N = 320$, with peak velocities differing by approximately 7%.

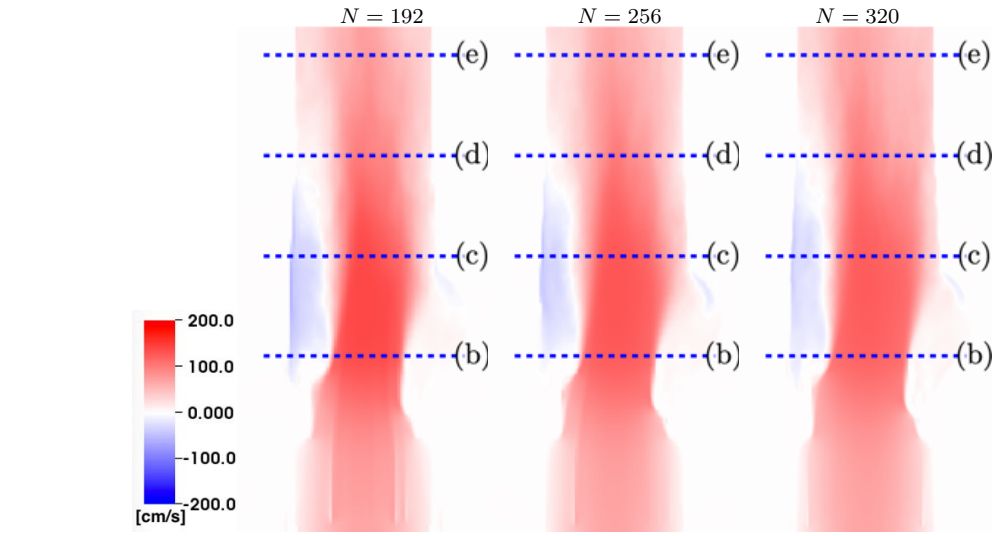

(a) Axial velocity (u_y) fields

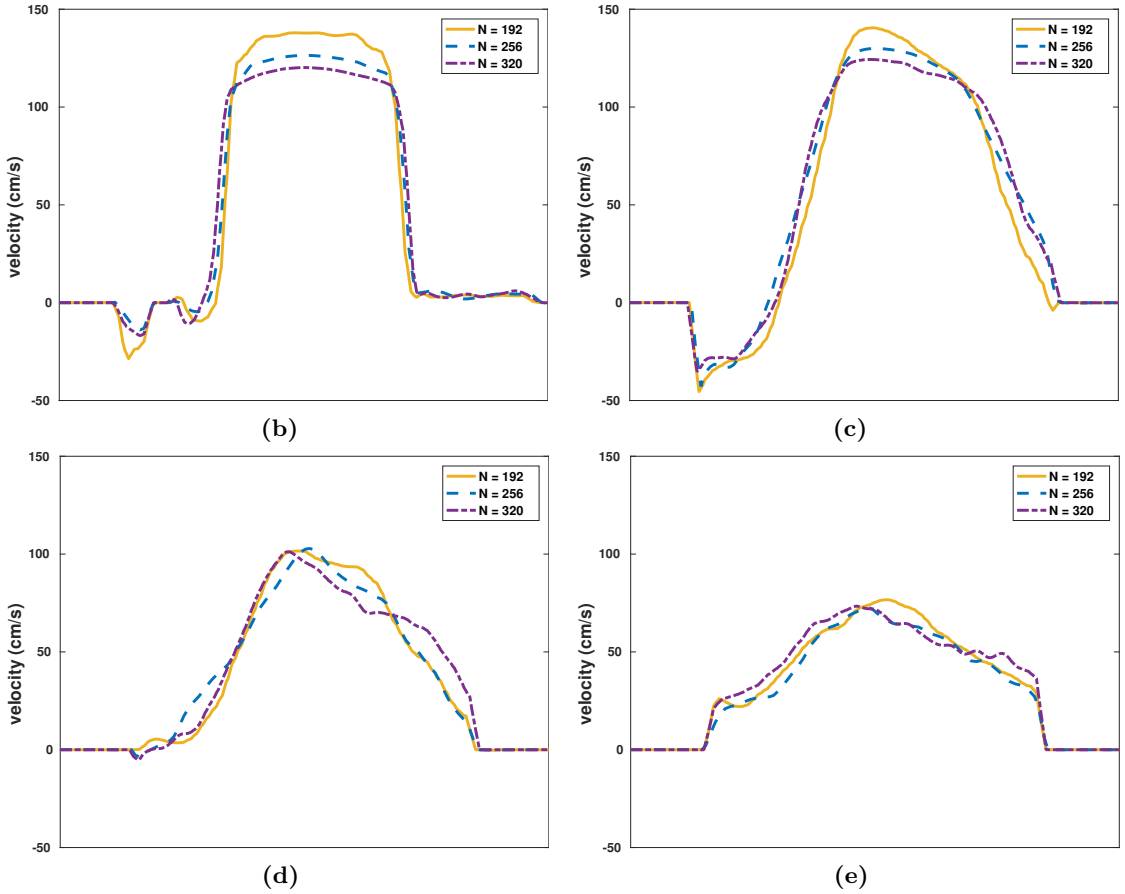

(b) **(c)** **(d)** **(e)**

Figure S11: (a) Cross-section view of time-averaged flow fields and (b)-(e) flow profiles at different locations downstream of the valve for the bovine pericardial valve model. We use steady flow at 50% of the maximum flow rate. In panel (a), the color shows the time-averaged axial velocity through the aortic test section at the center plane, with red indicating forward flow and blue indicating reverse flow. Blue dashed lines show where the profiles shown in panels (b)-(e) are obtained. The flow fields agree to within approximately 1.1% in the L^2 norm, with peak velocities agreeing to within approximately 4%.

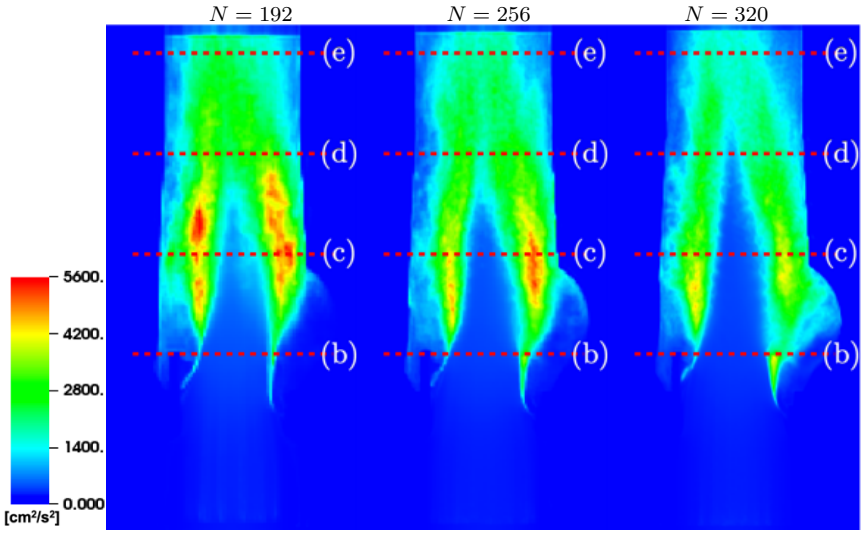

(a) TKE fields

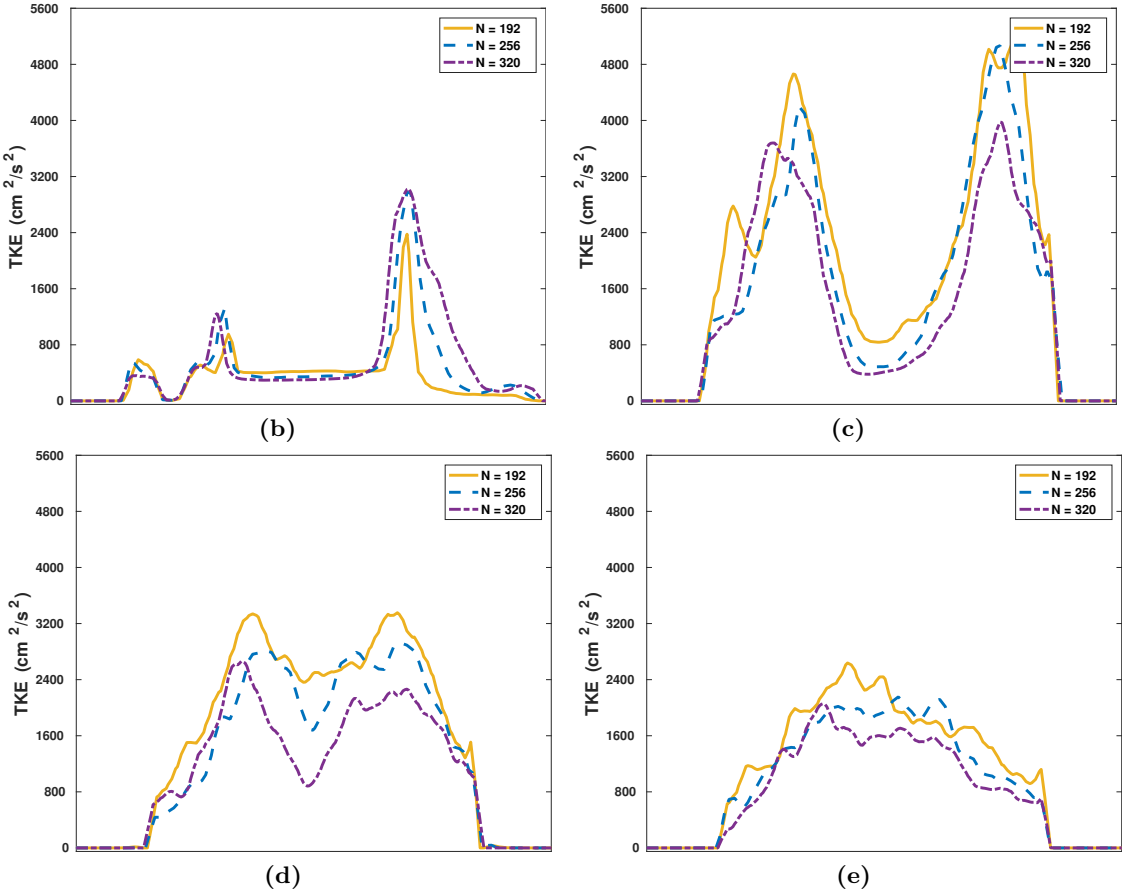

(b) **(c)** **(d)** **(e)**

Figure S12: (a) Cross-section view of turbulence kinetic energy (TKE) fields and (b)-(e) TKE profiles at different locations downstream of the valve for the bovine pericardial valve model. We use steady flow at the maximum flow rate. In panel (a), the color shows the magnitude of TKE through the aortic test section at the center plane. Red dashed lines show where the profiles shown in panels (b)-(e) are obtained. The L^2 differences are on the order of 10% between $N = 256$ and $N = 320$, with peak values of TKE differing by approximately 17.5%.

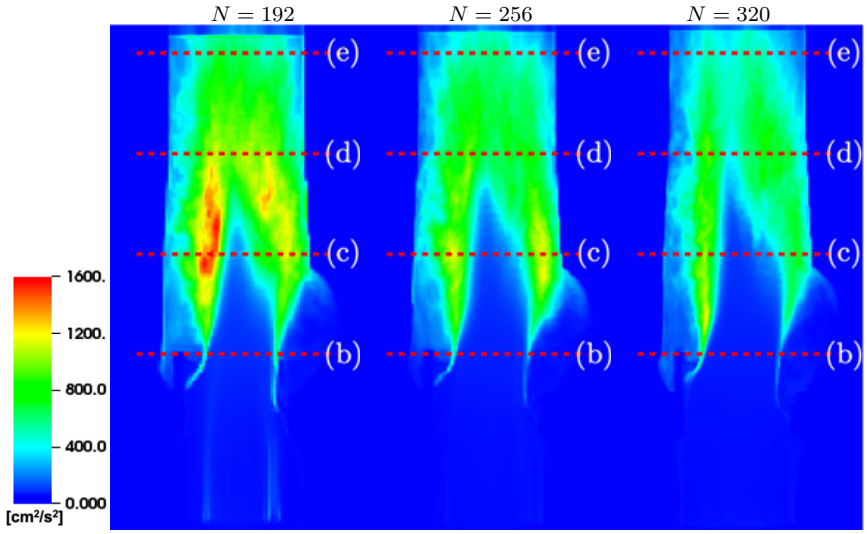

(a) TKE fields

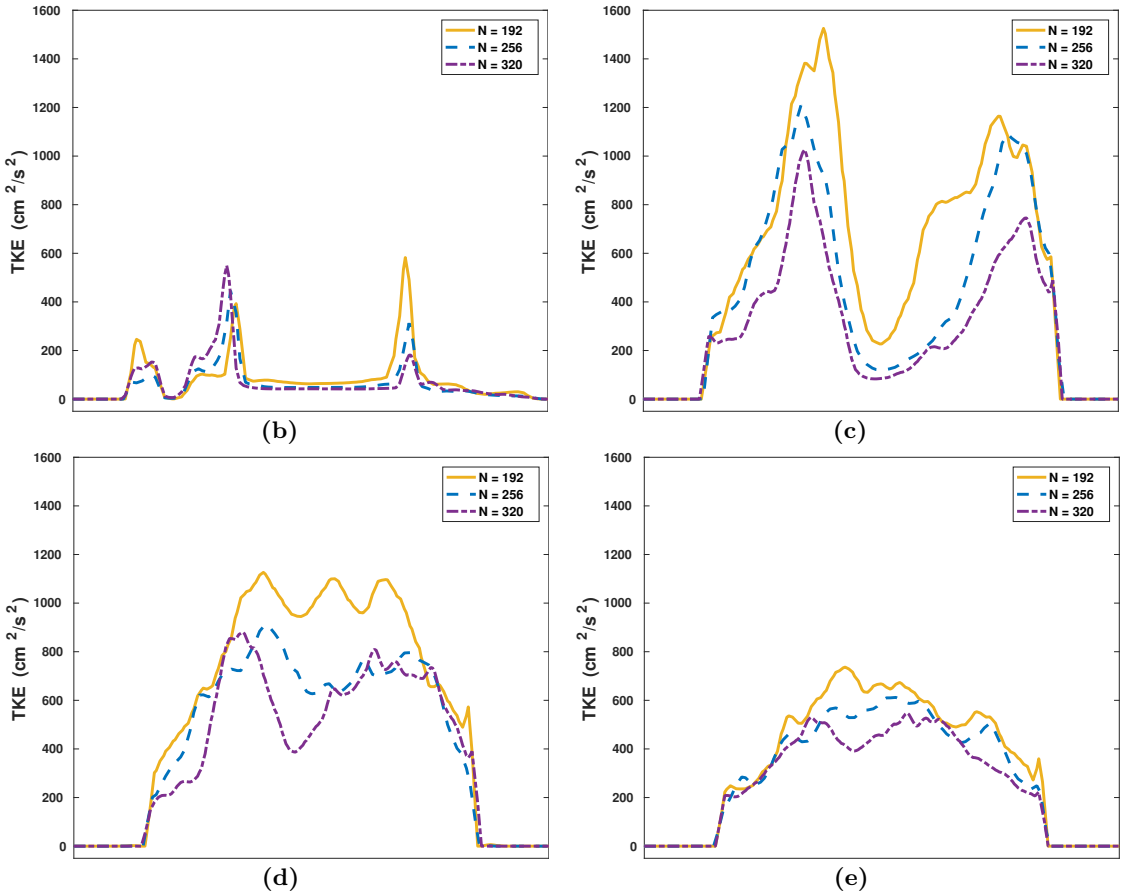

Figure S13: (a) Cross-section view of turbulence kinetic energy (TKE) fields and (b)-(e) TKE profiles at different locations downstream of the valve for the bovine pericardial valve model. We use steady flow at 50% of the maximum flow rate. In panel (a), the color shows the magnitude of TKE through the aortic test section at the center plane. Red dashed lines show where the profiles shown in panels (b)-(e) are obtained. The L^2 differences are on the order of 10% between $N = 256$ and $N = 320$, with peak values of TKE differing by approximately 1.5%.

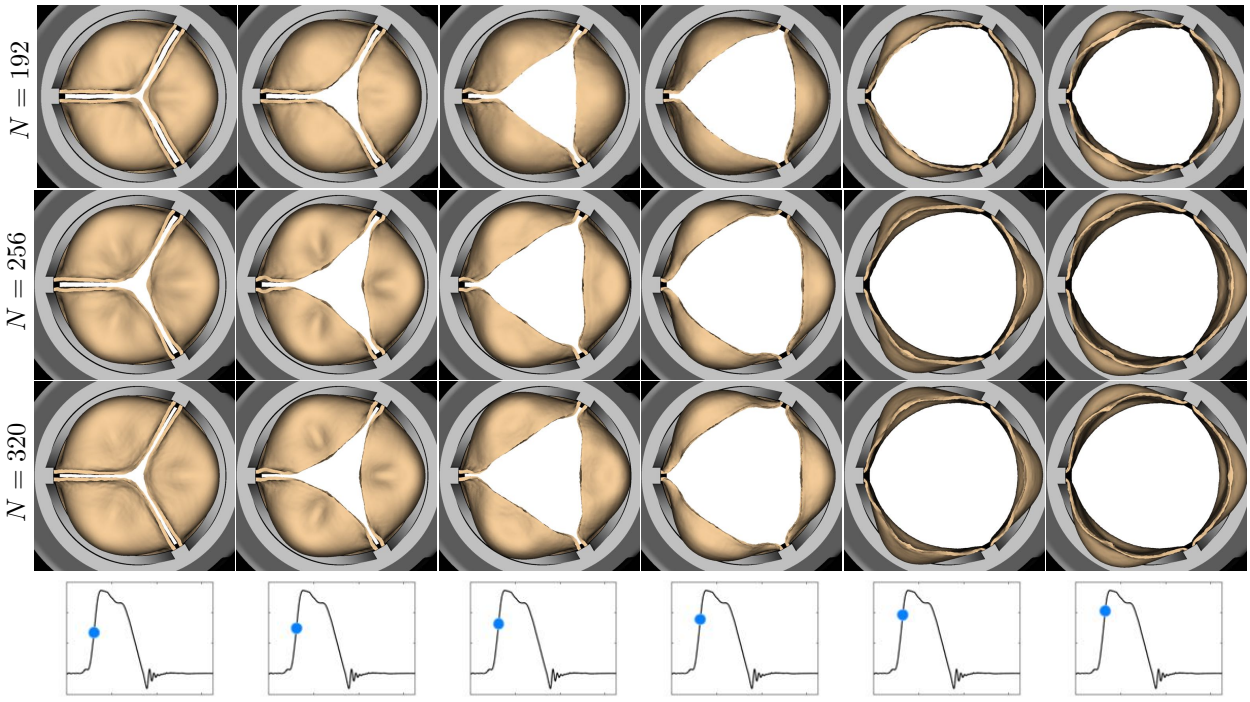

(a)

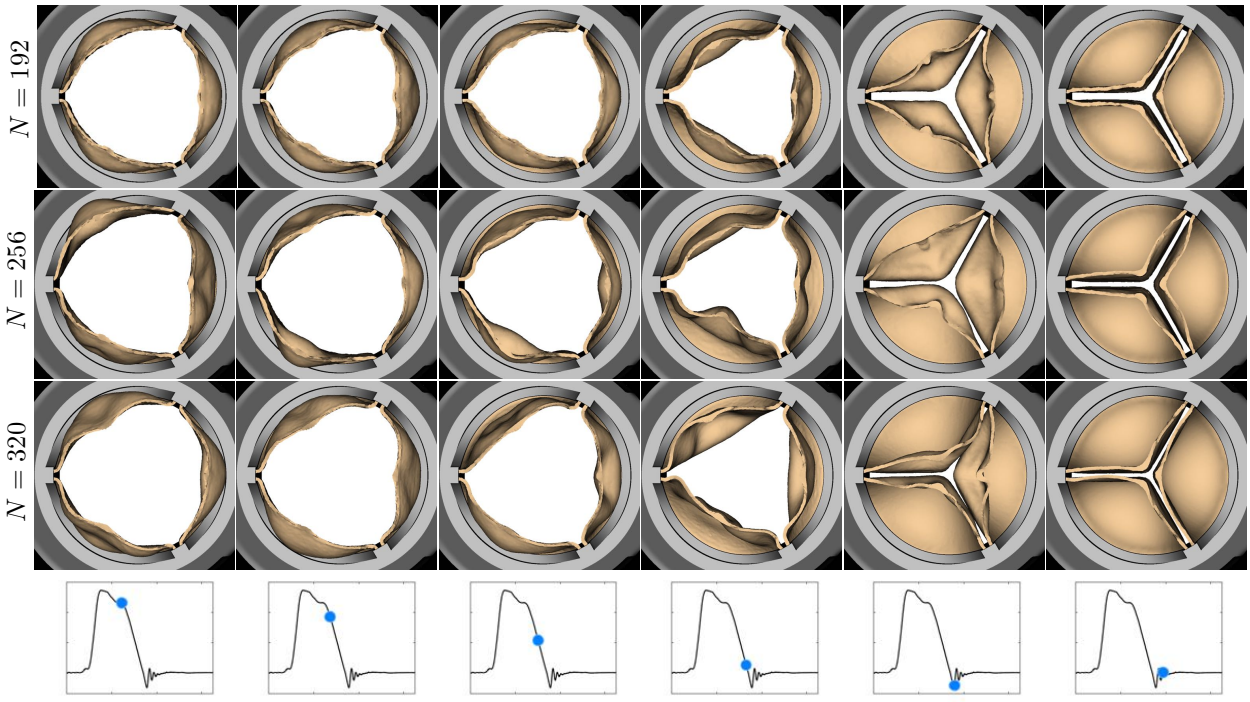

(b)

Figure S14: Leaflet kinematics of the porcine aortic valve during (a) valve opening and (b) valve closure under grid refinement. *Top panels*: $N = 192$, *middle panels*: $N = 256$, and *bottom panels*: $N = 320$. The time increment between frames in panel (a) is 1.92 ms, and the time increment between frames in panel (b) is 9.6 ms.

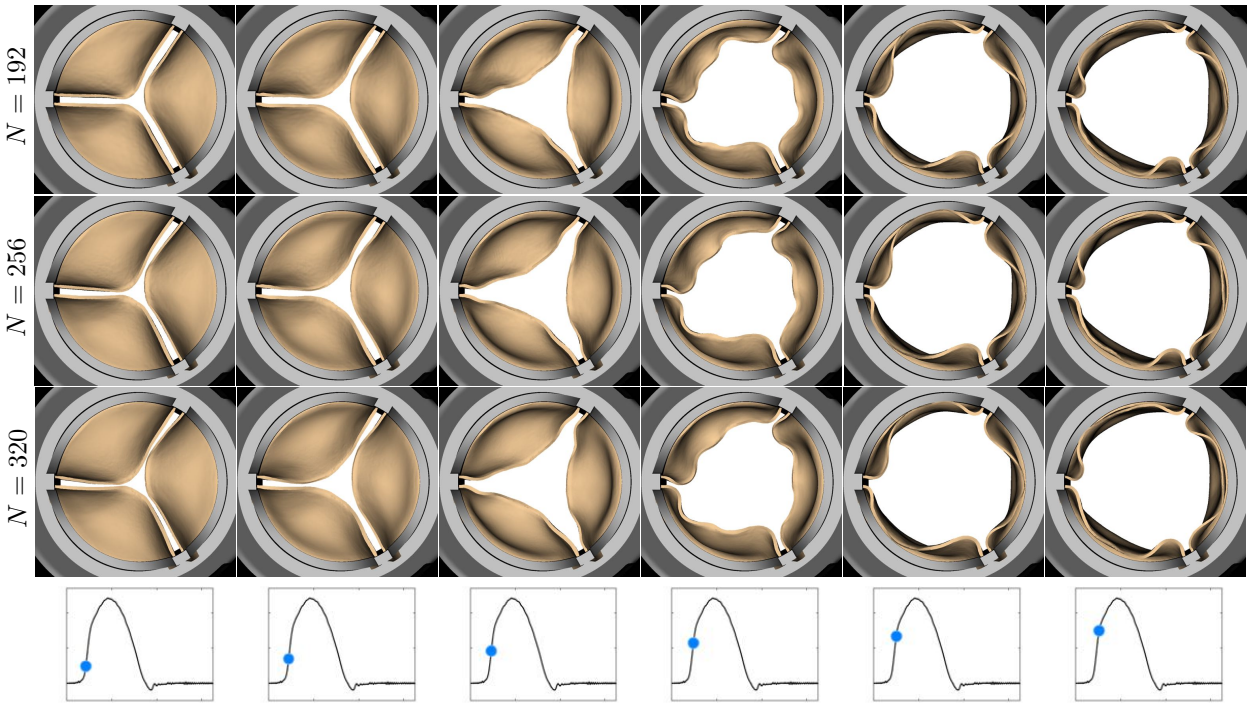

(a)

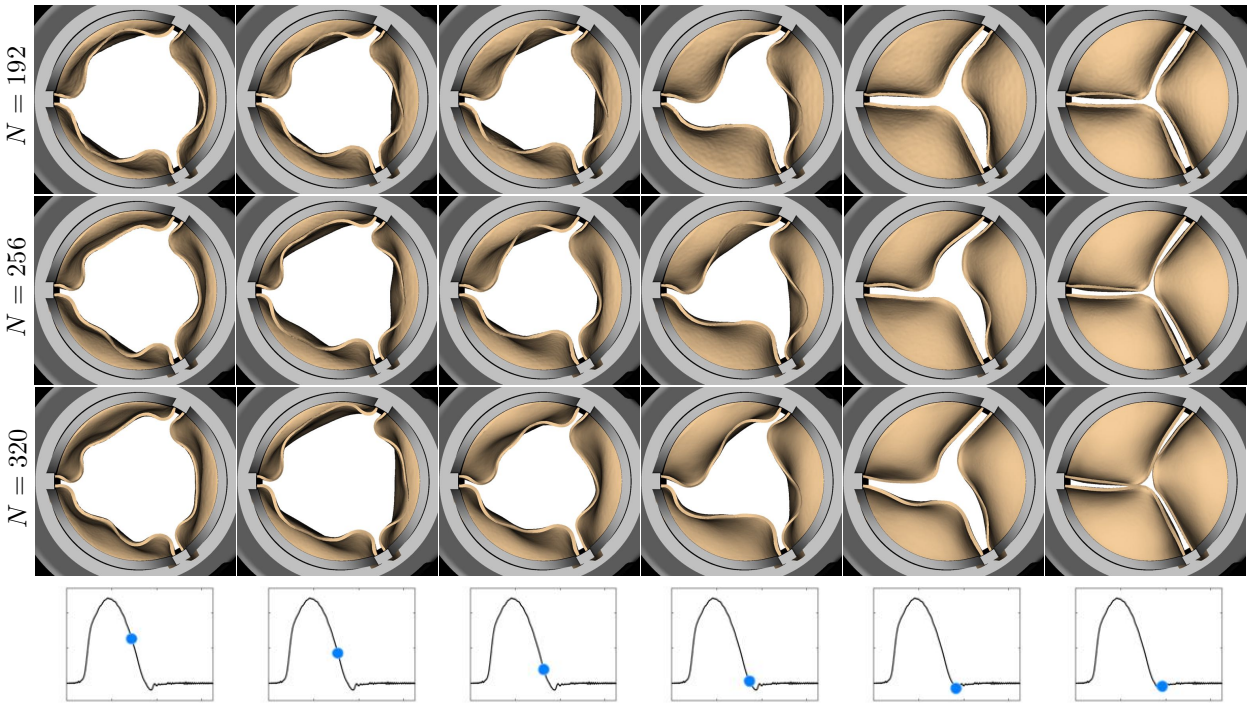

(b)

Figure S15: Leaflet kinematics of the bovine pericardial valve during (a) valve opening and (b) valve closure under grid refinement. *Top panels*: $N = 192$, *middle panels*: $N = 256$, and *bottom panels*: $N = 320$. The time increment between frames in panel (a) is 3.84 ms, and the time increment between frames in panel (b) is 19.2 ms.

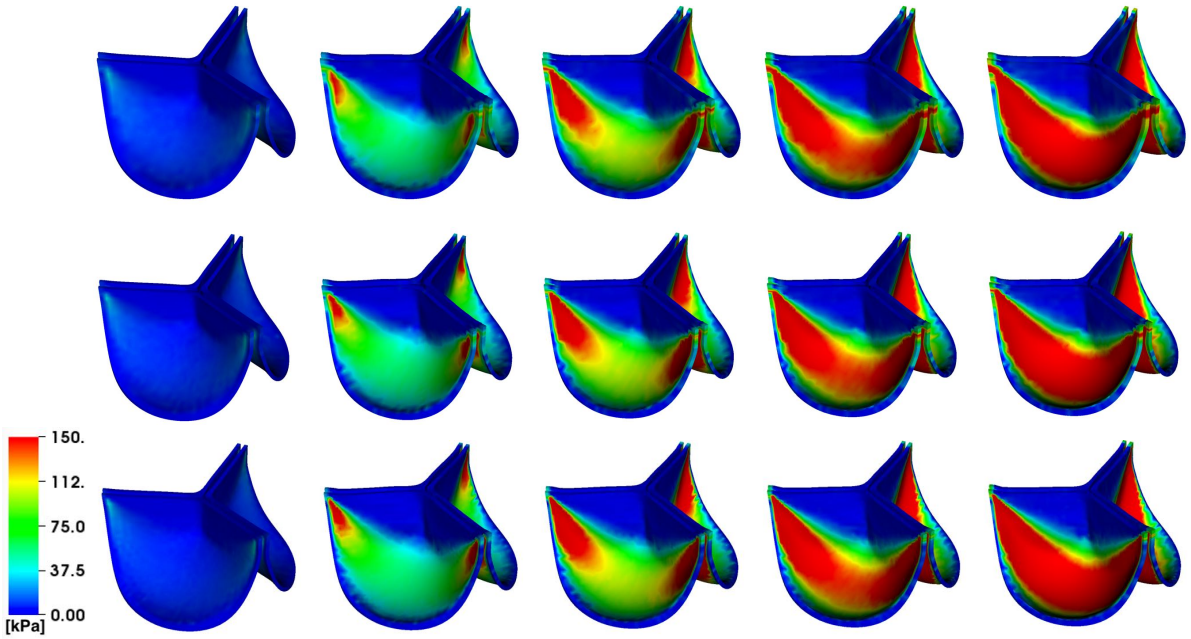

(a)

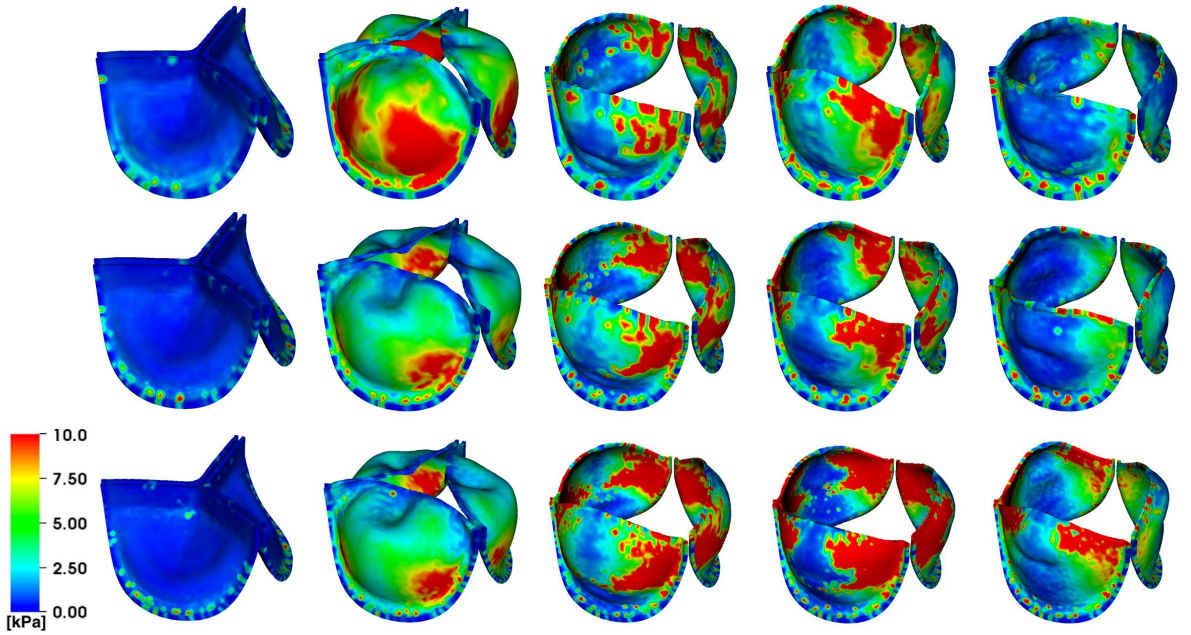

(b)

Figure S16: von Mises stress (kPa) on the porcine aortic valve during (a) valve closure and (b) valve opening under grid refinement. *Top panels*: $N = 192$, *middle panels*: $N = 256$, and *bottom panels*: $N = 320$ for both cases. The time increment between frames in panel (a) is 30.72 ms, and the time increment between frames in panel (b) is 11.52 ms.

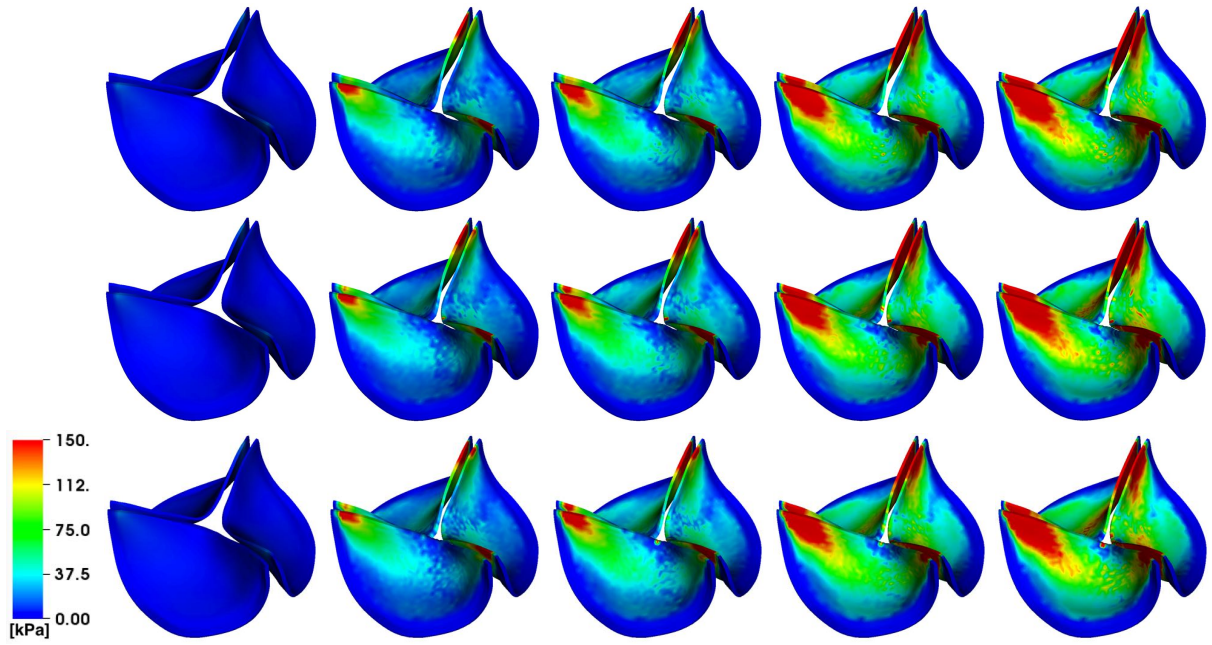

(a)

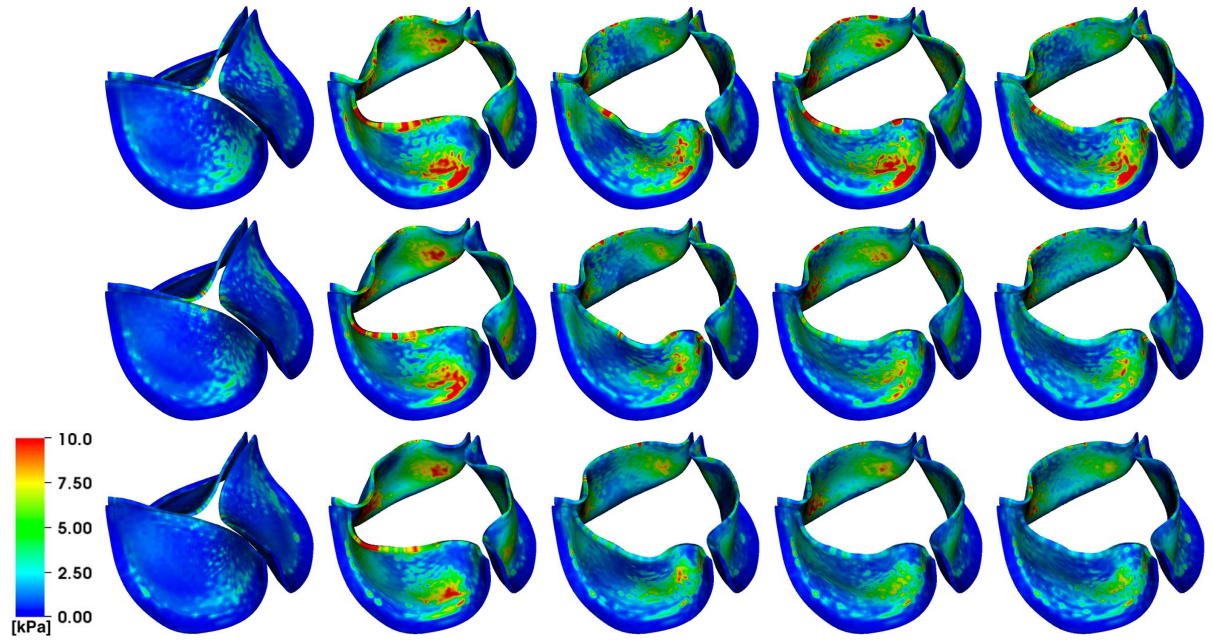

(b)

Figure S17: von Mises stress (kPa) on the porcine aortic valve during (a) valve closure and (b) valve opening under grid refinement. *Top panels*: $N = 192$, *middle panels*: $N = 256$, and *bottom panels*: $N = 320$ for both cases. The time increment between frames in panel (a) is 30.72 ms, and the time increment between frames in panel (b) is 11.52 ms.

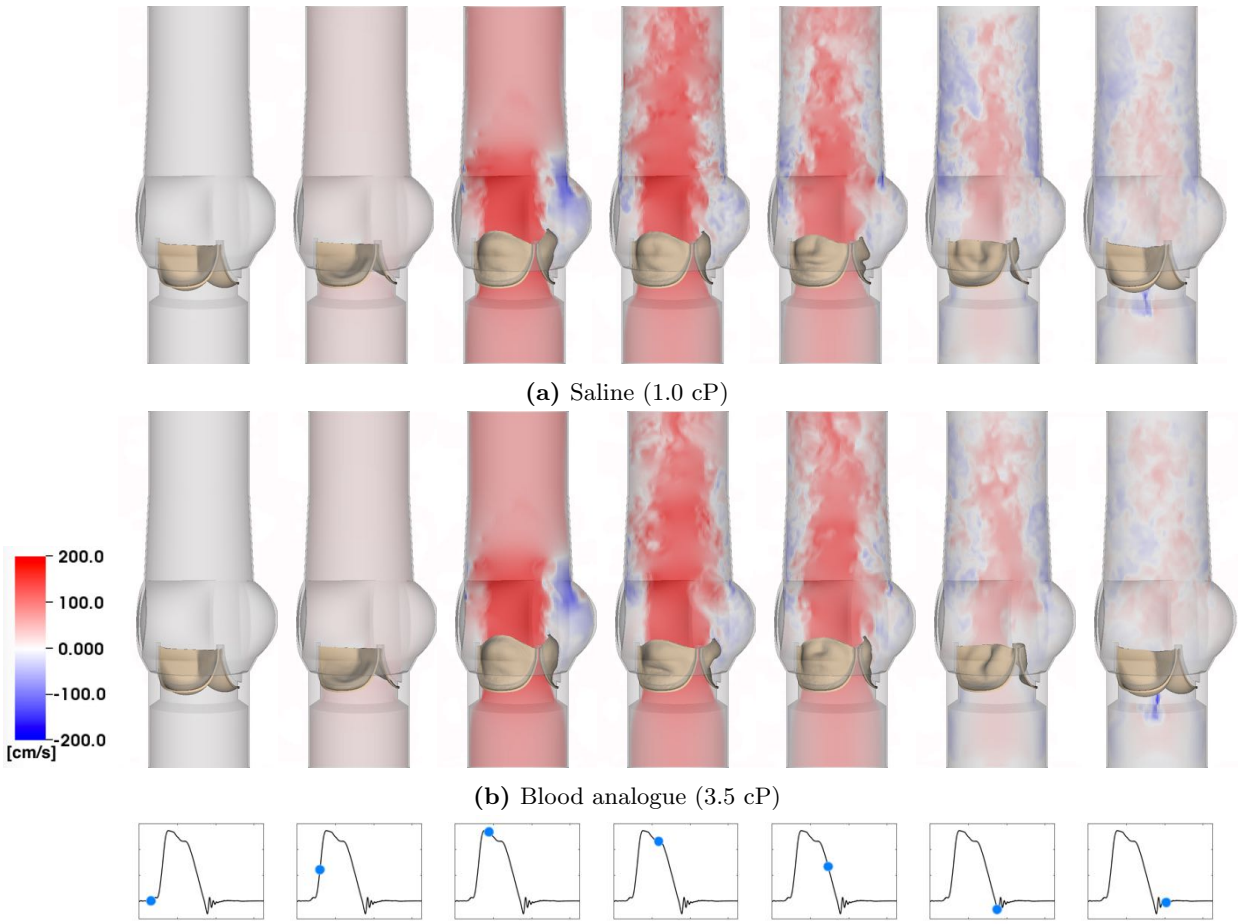

(a) Saline (1.0 cP)

(b) Blood analogue (3.5 cP)

Figure S18: Cross-section view of simulated flow patterns for the porcine aortic valve model using (a) saline with density 1.0 g cm^{-3} and viscosity 1.0 cP versus (b) Newtonian blood analogue with density 1.0 g cm^{-3} and viscosity 3.5 cP. The color shows the axial velocity through the aortic test section at the center plane, with red indicating forward flow and blue indicating reverse flow. (a) $Re_{\text{peak}} = 20{,}576$. (b) $Re_{\text{peak}} = 5{,}879$. The time increment between frames is 57.6 ms.

G Comparison Between Saline and Newtonian Blood Analogue Test Fluids

The goal of this study is to present our FSI models of bioprosthetic heart valves in the in vitro pulse duplicator system in the same setting as the completed experiments, which use saline as the test fluid. Even so, we performed additional simulations with a Newtonian blood analogue fluid with density 1.0 g cm^{-3} and viscosity 3.5 cP to show that our FSI models can be used in such flow regime without numerical instabilities (Figures S18 and S19). We are also interested in understanding the influence of using saline as compared to a more realistic blood analogue fluid in in vitro testing. To compare the predictions of the model for different test fluids, we perform simulations at the finer resolution ($N = 256$) for both pulsatile and steady mean simulations. For the comparison of the steady mean simulation, we only show the results for the bovine pericardial valve case. The porcine aortic valve model yields similar results and is not shown.

Our simulations indicate that the large scale flow structures are very similar between saline and the blood analogue fluid (Figures S18, S19, and S20). However, we observed differences in the small-scale turbulent flow structures present between saline and blood analogue fluid case (Figure S21), especially in the maximum steady flow case (Figure S21a). This is expected because of the larger Reynolds number associated with saline compared to the blood analogue.

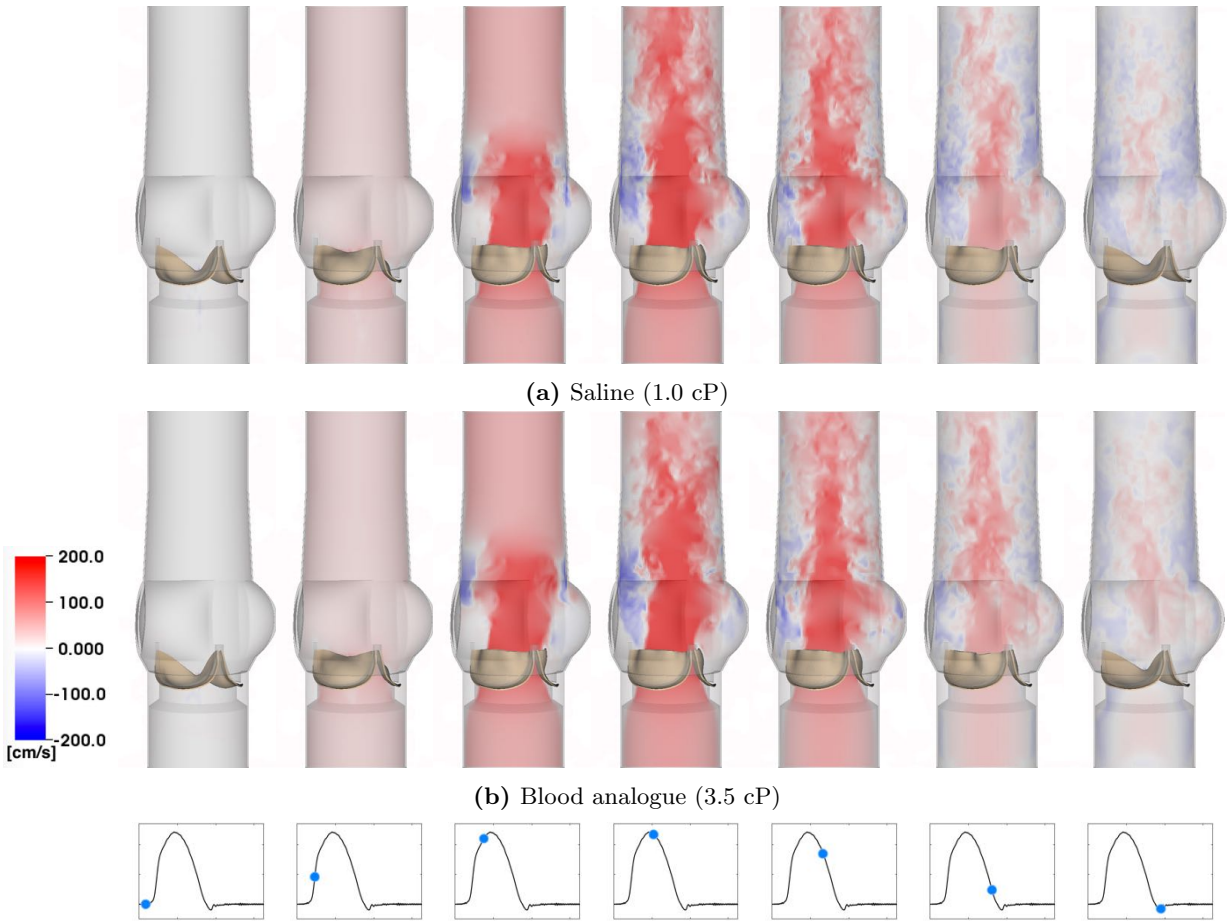

(a) Saline (1.0 cP)

(b) Blood analogue (3.5 cP)

Figure S19: Cross-section view of simulated flow patterns for the bovine pericardial valve model using (a) saline with density 1.0 g cm^{-3} and viscosity 1.0 cP versus (b) Newtonian blood analogue with density 1.0 g cm^{-3} and viscosity 3.5 cP. The color shows the axial velocity through the aortic test section at the center plane, with red indicating forward flow and blue indicating reverse flow. (a) $Re_{\text{peak}} = 19{,}330$. (b) $Re_{\text{peak}} = 5{,}523$. The time increment between frames is 57.6 ms.

Figures S22 and S23 show that the leaflet kinematics for saline versus the blood analogue fluid are similar because the leaflet kinematics are driven mostly by large-scale flow features.

H Simulation Environment

For $N = 256$, FSI simulations take about six days to compute a full cardiac cycle using 64 processor cores on *Dogwood* cluster managed by University of North Carolina Information Technology Services Research Computing. In this study, we focus on modeling aspects rather than parallel performance analysis. There is currently an ongoing effort to improve the parallel performance of the IBAMR software library, and we aim to report on these efforts, and their impacts on models like those described herein, in the future.

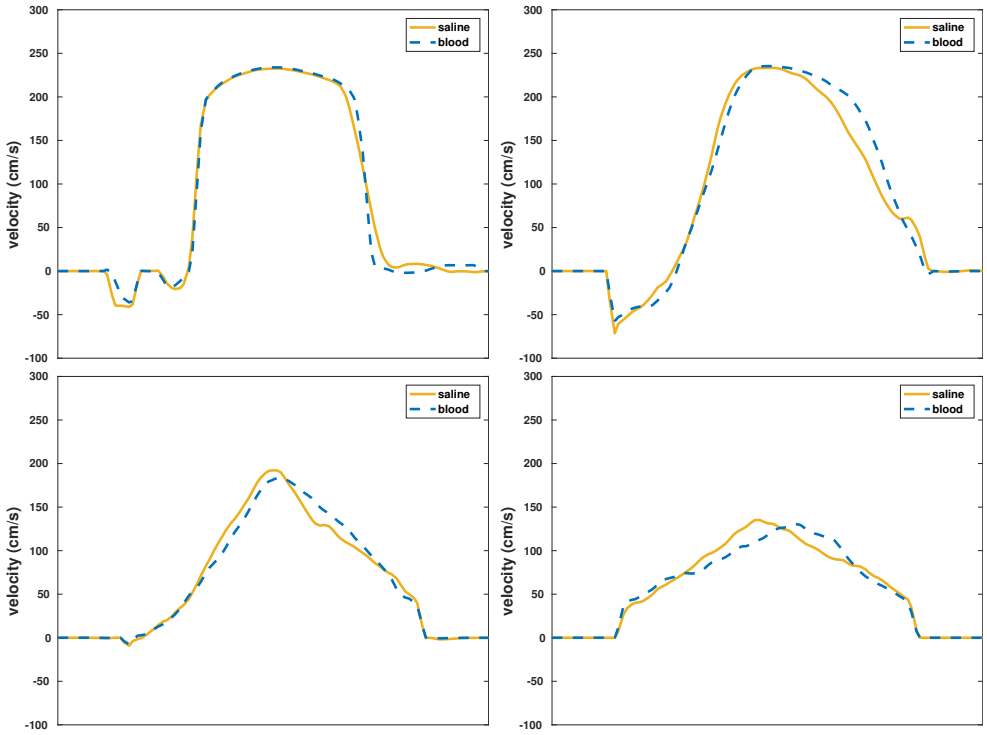

(a) Maximum steady flow rate

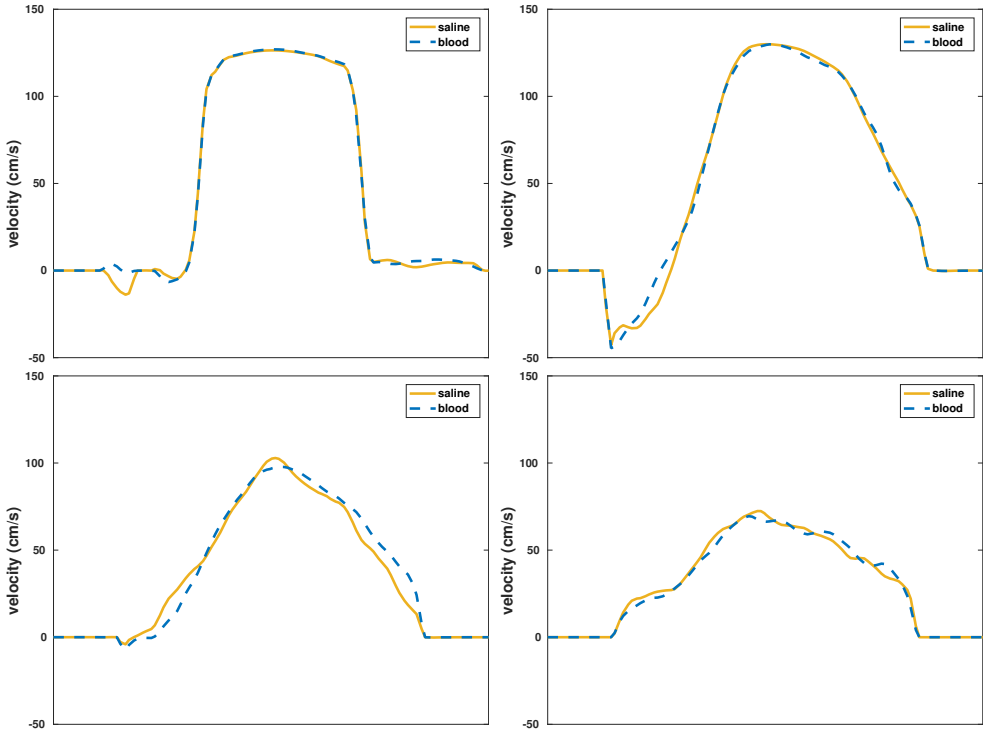

(b) 50% maximum steady flow rate

Figure S20: (a) Cross-section view of time-averaged axial velocity profiles at different locations downstream of the valve for the bovine pericardial valve model. We use steady flow at (a) the maximum and (b) 50% of the maximum flow rate. Flow profiles are show at the same locations as indicated in Figures S10 and S11.

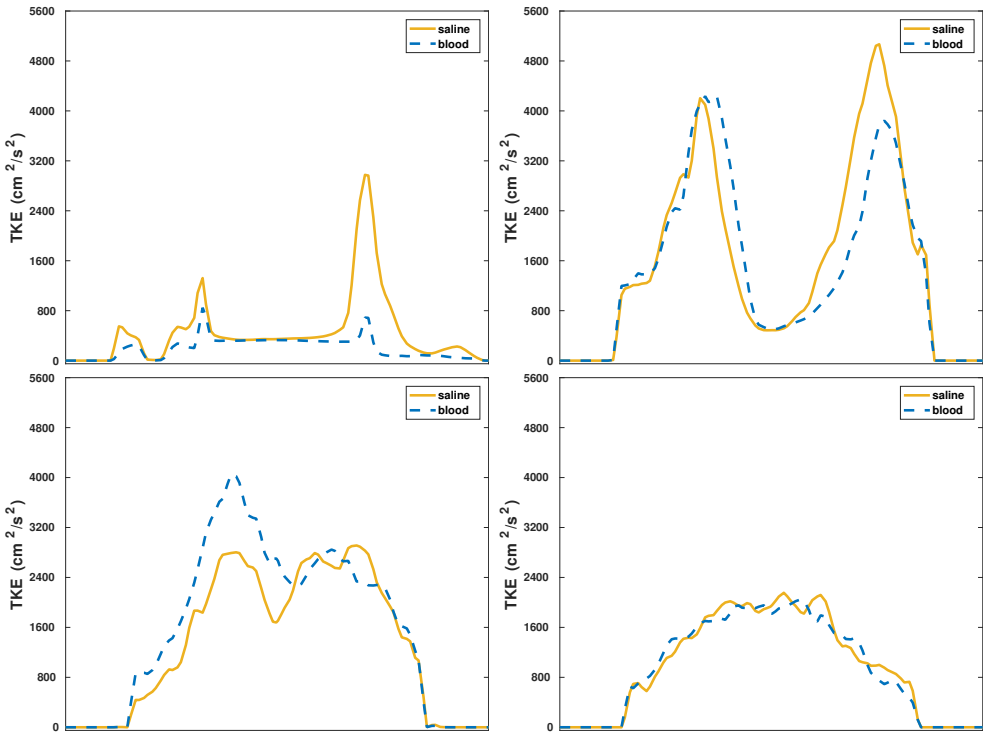

(a) Maximum steady flow rate

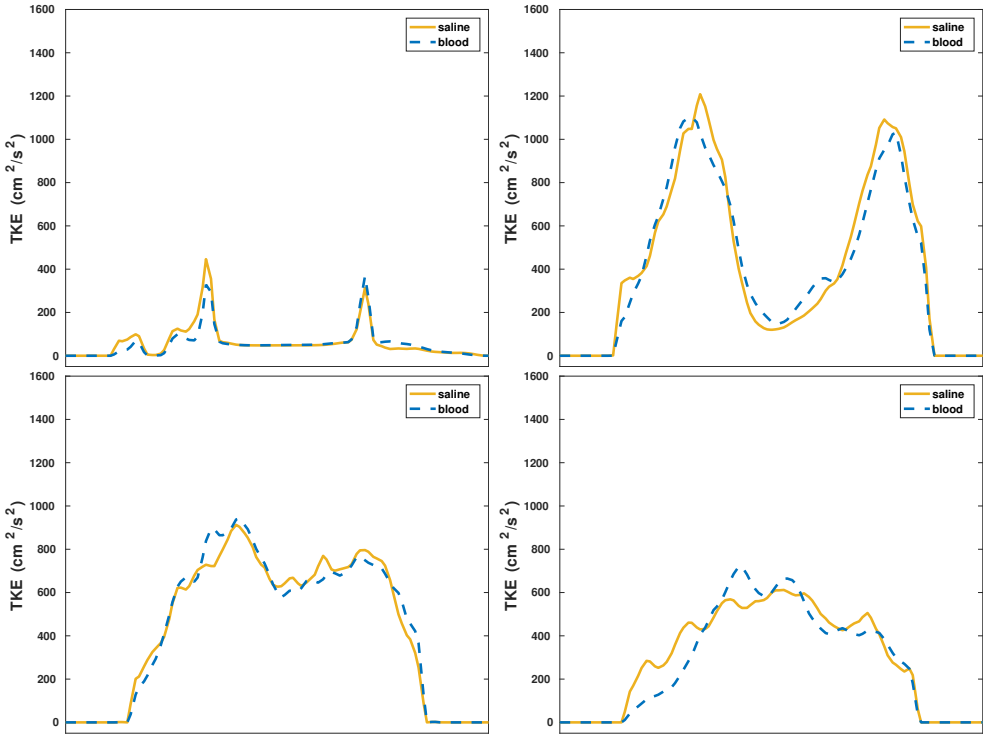

(b) 50% maximum steady flow rate

Figure S21: (a) Cross-section view of time-averaged turbulence kinetic energy (TKE) profiles at different locations downstream of the valve for the bovine pericardial valve model. We use steady flow at (a) the maximum and (b) 50% of the maximum flow rate. TKE profiles are show at the same locations as indicated in Figures S12 and S13.

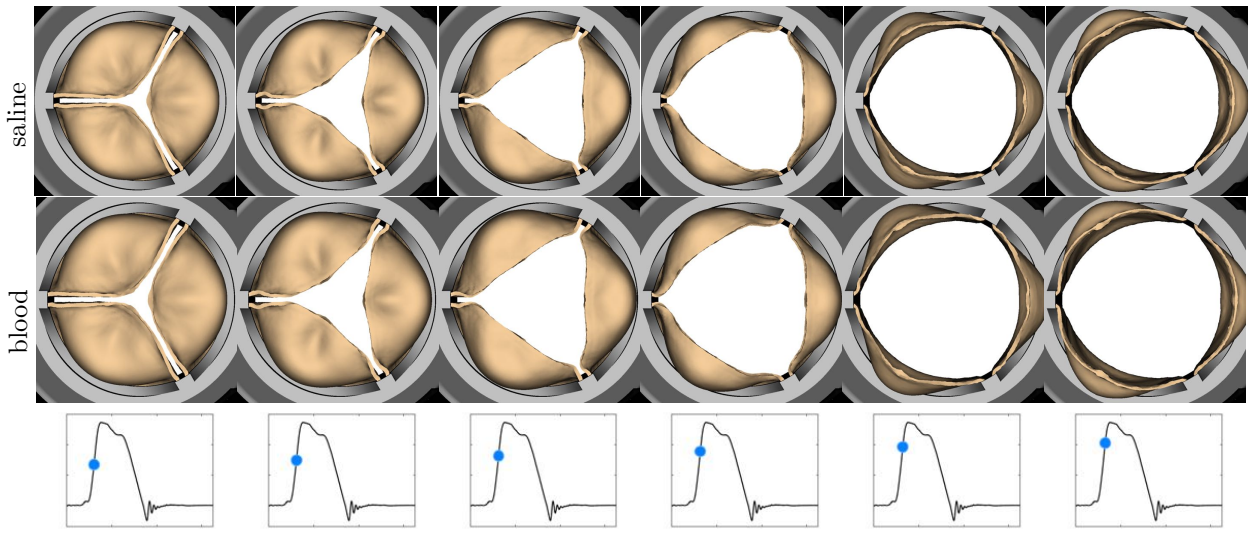

(a)

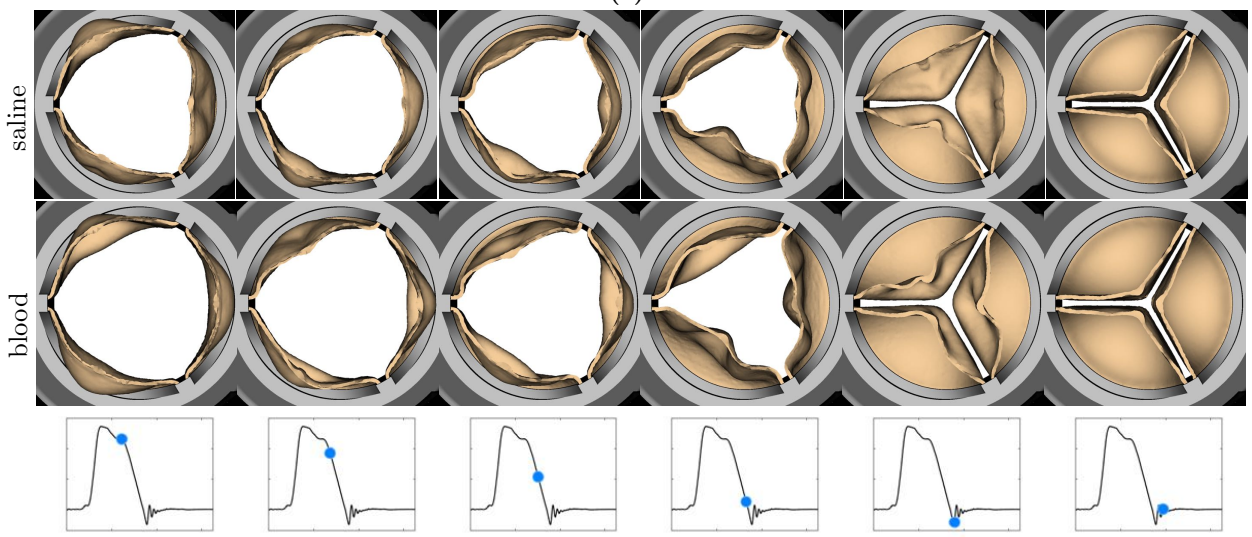

(b)

Figure S22: Comparison of leaflet kinematics of the porcine aortic valve during (a) valve opening and (b) valve closure between saline and blood analogue. The time increment between frames in panel (a) is 1.92 ms, and the time increment between frames in panel (b) is 9.6 ms.

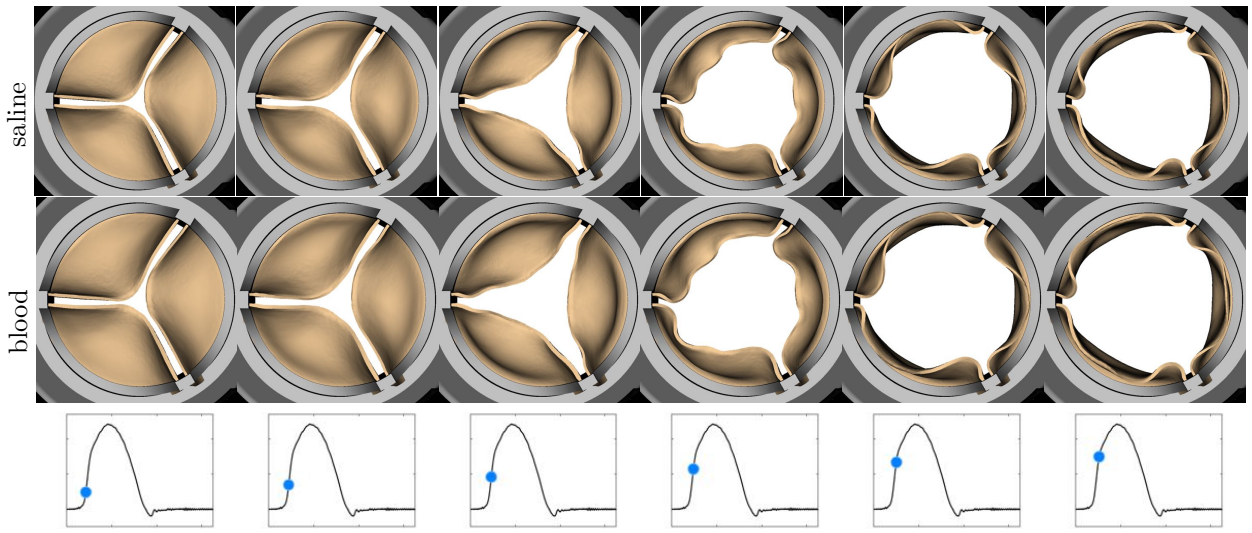

(a)

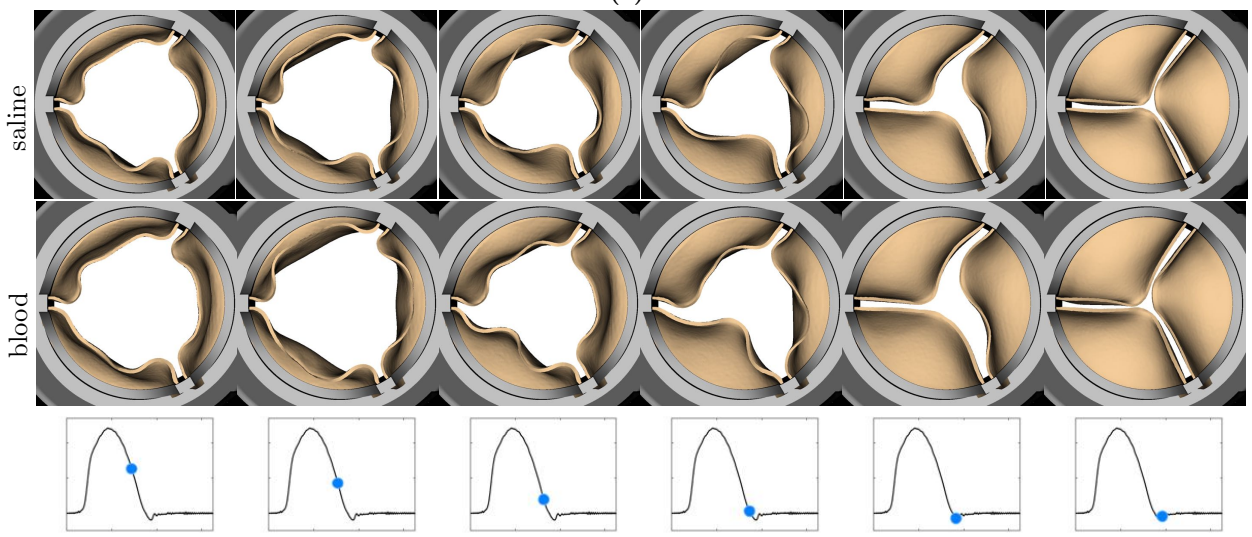

(b)

Figure S23: Comparison of leaflet kinematics of the bovine pericardial valve during (a) valve opening and (b) valve closure between saline and blood analogue. The time increment between frames in panel (a) is 3.84 ms, and the time increment between frames in panel (b) is 19.2 ms.